ZIRCONIA-BASED ELECTROCERAMIC MATERIALS FOR SOFC APPLICATIONS

Alan John Feighery

A Thesis Submitted for the Degree of PhD
at the
University of St Andrews

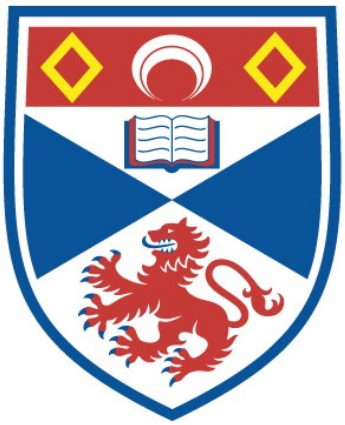

1999

'Studies of possible solid oxide fuel cell anode materials in the $MgO:TiO_2:ZrO_2$ ternary system'

A thesis submitted for the degree of M.Phil.

John D.W. Sutherland

School of Chemistry, University of St. Andrews, The Purdie Building, St. Andrews, Fife, KY16 9ST.

January 1997

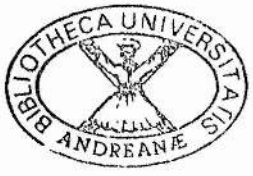

Contents

Declaration

I, John David Wightman Sutherland, hereby certify that this thesis has been composed by myself, that it is a record of my own work and that it has not been accepted in partial or complete fulfilment of any other professional qualification.

Signed ..... Date 24/1/97.....

I was admitted to the Faculty of Science of the University of st. Andrews under Ordinance General 12 on 1st October 1995, and as a candidate for the degree of M.Phil. on 1st October 1995.

Signed ..... Date 24/1/97.....

I hereby certify that this candidate has fulfilled the conditions of the Resolution and Regulations appropriate to the degree of M.Phil.

Signature of Supervisor ..... Date 24/1/97.....

In submitting this thesis to the University of St. Andrews, I understand that I am giving permission for it to be made available for use in accordance with the Regulations of the University Library for the time being in force, subject to any copyright vested in the work not being affected thereby. I also understand that the title and abstract will be published, and that a copy of the work may be made and supplied to any *bona fide* library or research worker.

Acknowledgements

I would like to thank my supervisor, Dr. John T.S. Irvine for his supervision and guidance. The support of everyone in the Irvine group must be thanked for their help and tenacity when needed (Richard Gover, Brian Mitchell, Alan Feighery, Peter Slater and Nianhua Peng). Lastly, a special mention must be made of Professor Chaogui Zheng (Beijing University, China) for his encouragement during his period of research in St. Andrews

Key to abbreviations used in the thesis

Certain words have been abbreviated for convenience. The following list shown below shows the abbreviation symbol used and its expanded form.

Abbreviation	Expanded form
M_2T	Spinel
S	Spinel phase
MT	Ilmenite
I	Ilmenite phase
MT_2	Distorted pseudobrookite
P	Distorted pseudobrookite phase
ZT	Orthorhombic
O	Orthorhombic phase
Z(c)	Cubic-fluorite
C	Cubic-fluorite phase
T	Tetragonal ZrO_2 phase
M	Monoclinic ZrO_2 phase

Abstract

The $MgO:TiO_2:ZrO_2$ ternary system was investigated as a possible novel anode material in a solid oxide fuel cell. Titanium-substituted yttria-stabilised zirconias have the necessary electrical conductivity properties for a ZrO_2-based fluorite electrode but problems have been encountered such as a decrease in unit-cell size upon reduction leading to mechanical failure. By incoporating magnesium into the titanium-stabilised zirconia structure, it was thought that the cubic-fluorite structure might be stabilised.

A phase diagram study was made of the $MgO:TiO_2:ZrO_2$ ternary system at 1500°C. Upon researching the literature phase diagram of the $MgO:TiO_2:ZrO_2$ system, it was found that the authors had not studied the single-phase region in the ZrO_2-rich area extensively and did not use a consistent temperature for their analysis of samples. This has meant that the phase diagram has had to be reinvestigated. The results obtained at 1500°C are in disagreement with the previously published phase diagram. A large area bounded by single-phase cubic-fluorite was detected; however the central region of this domain contained both tetragonal and cubic-fluorite domains. This implies that for the central region of this phase area that the cubic-fluorite phase is not stable at 1500°C.

Selected stabilised cubic-fluorite samples with ~ 10 atom% Mg were annealed at 1000°C after preparation at 1500°C and it was found that due to the presence of other phases present at 1000°C, that the cubic-fluorite phase is thermodynamically unstable at lower temperatures. DTA analysis revealed that as the titanium content in the cubic-fluorite solid-solution increased, the phase transition from tetragonal phase (+ MgO) to cubic-fluorite phase decreased. These results were used to provide a basis for a temperature phase diagram showing the likely phase transitions that occur at a particular temperature range.

The activation energy for conduction increased and ionic conductivity decreased with increasing titanium content in the solid solution, due to the effects of local distortions created by the smaller ionic radius of titanium when compared to zirconium.

Chapter 1

Introduction

1.1 Project Overview

In the search for new improved energy systems for the 21st century, the emphasis is on environmentally friendly, efficient means of energy conversion and storage. At the forefront of those technologies is the Solid Oxide Fuel Cell (SOFC) which it is hoped will find widespread application in the conversion of chemical to electrical energy.

In Solid Oxide Fuel Cells, the most important challenge facing today's materials scientists is the selection of materials for the fuel electrode. In this thesis, a study was made of the $MgO:TiO_2:ZrO_2$ phase diagram with a view to obtaining single phase pure cubic-fluorite samples. These samples would then be tested with respect to their suitability as an anode material for a Solid Oxide Fuel Cell by means of experiments such as Ac-impedance spectroscopy and thermal analysis (TGA-DTA).

1.2 The Chemistry of Zirconia

Zirconia (ZrO_2) exists in three polymorphs at normal ambient pressure; additionally an orthorhombic phase observed at high pressure has been reported[1]. The structures of the three polymorphs are shown in Figure 1.1. Major differences between the three structures are illustrated by changes in cell angle and lattice parameters as shown in Table 1 [2,3,4].

Monoclinic

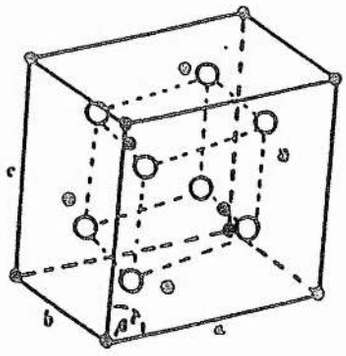

Tetragonal

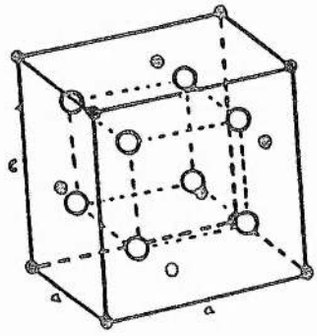

Cubic

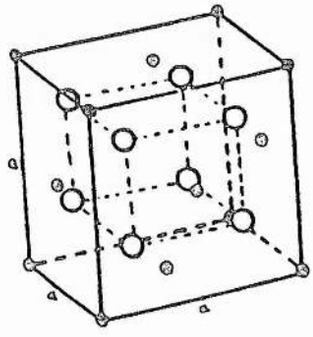

Figure 1.1: Structures of the monoclinic, tetragonal and cubic polymorphs of zirconia

Monoclinic	Tetragonal	Cubic
Space Group $P2_1/c$	Space Group $P4_2/nmc$	Space Group Fm3m
a = 5.156 Å	a = 5.094 Å.	a = 5.124 Å
b = 5.191 Å	c = 5.177 Å	
c = 5.304 Å		
β = 98.9°		

Table 1.1: Crystallographic data for the three polymorphs of zirconia

At room temperature, zirconia exists in the monoclinic form and undergoes a martensitic transformation at 1170°C to form the tetragonal structure. Further heating to above 2370°C causes the tetragonal structure to undergo a tranformation to the cubic-fluorite structure[5].

The martensitic transformation of monoclinic to tetragonal ZrO_2 is one of the most studied transformations in a non-metallic system[6]. Martensitic transformations occur by a shearing mechanism to give plates of product within the parent crystal (Figure 1.2). At the parent-product interfaces $A_1B_1C_1D_1$ and $A_2B_2C_2D_2$, the structures match well and there is a orientation relationship between the crystal structures of the two phases. As the parent and product phases have the same composition and closely related crystal structures there is no need for activation energy to support diffusion as only very small atomic displacements of about less than one bond-length are required to support the transformation. Transformation rates are often independent of temperature but may be subject to applied stresses and strains.

Figure1.2 (b)shows a partially formed martensitic crystal. Unlike other phase transitions, martensitic transformations do not proceed to completion at a constant temperature but take place over a wide range of temperatures. In the case of ZrO_2, the transformation occurs at around 1000°C as shown in Figure 1.3. On heating, the monoclinic phase which is stable at low temperatures, transformation to the tetragonal phase begins above ~ 1000°C but is not complete until ~ 1120°C. The transformation exhibits a hysteresis of

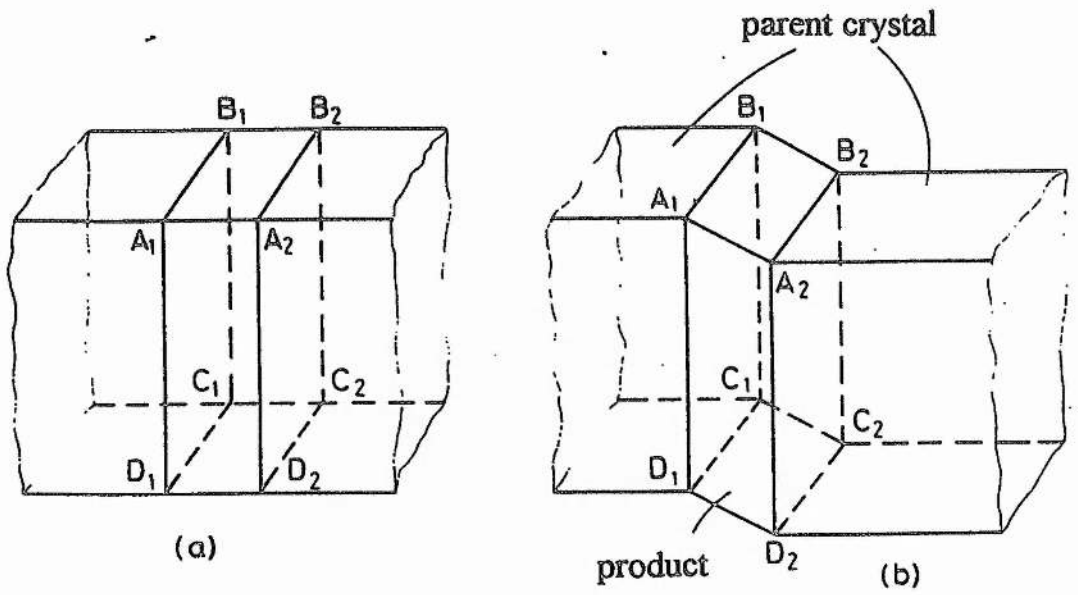

Figure 1.2 Formation of a martensite plate within a parent crystal

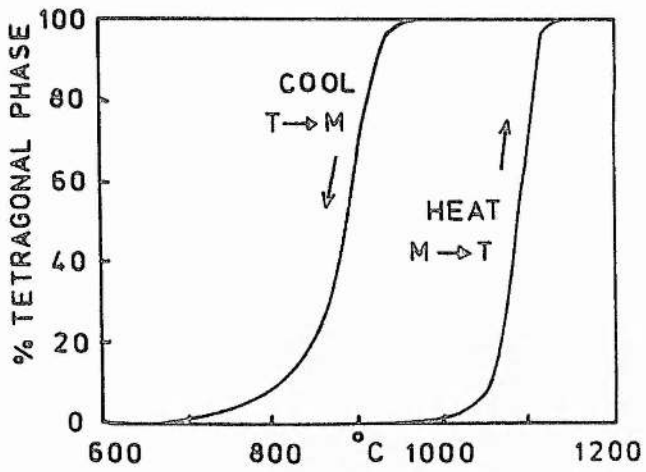

Figure 1.3 Monoclinic (M)-tetragonal (T) martensitic transformation in zirconia determined by high temperature powder X-ray diffraction (Adapted from West[6])

about 200°C, and the reverse tranformation begins at only ~ 930°C. The transition is classified as athermal as it takes place over a range of temperatures and the percentage transformation within that range does not change with time as long as the temperature remains constant. If the temperature is changed, the new 'equilibrium' state is reached extremely rapidly.

The tetragonal phase of zirconia was first determined by Teufer[3]. It consists of a distorted fluorite structure which is characterized by an 8-fold co-ordination of zirconium atoms and two completely different sets of Zr-O distances which are 2.445Å and 2.065Å, respectively[7]. For tetragonal zirconia, with $P4_2/nmc$ symmetry, the zirconium and oxygen ions are at the following sites:

Atom	**Position**	**Fractional Co-ordinates**	
Zr	2 (a)	(0,0,0)	(½, ½, ½)
O	4 (d)	(0, ½, z)	(½, 0, z)
		(0, ½, ½+z)	(½, 0, ½)

Tetragonal zirconia has been obtained at room temperature but its formation is dependent upon crystallite size and cooling regime; crystallite sizes of less than 30nm or rapid cooling are required[8]. Tetragonal stabilised zirconia is commonly obtained from the preparation of zirconia by 'wet' chemical processing routes such as *sol-gel*[9], where crystallites of diameter between 10-20nm have been obtained.

The instability of the cubic stabilised zirconia structure at room temperature is rather unusual when compared to other $M^{2+}F_2$ and $M^{4+}O_2$ compounds with the cubic fluorite structure as other compounds with the fluorite structure (e.g. ThO_2 and CaF_2) are stable at room temperature.

This unusual behaviour can be explained by the radius ratio (r_{cation}/r_{anion}) as described by Pauling. Ionic compounds with the general formula MX_2 are expected to have one of three structure types, depending upon their co-ordination number; silica (CN=4), rutile (CN=6) and fluorite (CN=8). A minimum radius ratio of 0.732 is required for the structure to have the fluorite structure with CN=8, whereas a minimum of 0.414 is expected for the rutile structure[9] with CN=6. Some examples of $M^{2+}F_2$ and $M^{4+}O_2$ compounds, along with their radius ratio, co-ordination number, cation ratio and structure type commonly observed are shown in Table 1.2 , based upon the ionic radii data provided by Shannon and Prewitt[10], $R(O^{2-})$=1.24Å, $R(F^-)$=1.17Å.

For compounds with a radius ratio close to unity, the fluorite structure is observed with CN=8. Examples of compounds which have the fluorite structure include CeO_2, ThO_2, CdF_2 and CaF_2. The radius ratio for zirconia with a co-ordination number of 8 is just larger than the minimum value of 0.732; whereas with a co-ordination number of 6, it is significantly larger than a MX_2 compound which has the rutile structure (e.g. TiO_2). Such a borderline situation suggests that the zirconium ions are slightly too small to sit in an eight-fold site which would provide the cubic-fluorite structure but too large for an octahedral six-fold site. So, a compromise is made with zirconium having a co-ordination number of 7; producing monoclinic symmetry. In addition to a co-ordination number of 7, the Zr-O bond lengths are quite different, with 3 average values of 2.07Å and 4 average Zr-O distances of 2.17Å.

The transformation of the monoclinic polymorph to the tetragonal polymorph on heating is accompanied by an increase in co-ordination number from 7 to 8, although the distorted cubic fluorite structure remains. The cubic fluorite eight-fold co-ordination exists only at very high temperatures where the distortion disappears.

Formula	Radius Ratio (CN)	Cation Radius	Structure Type
SiO_2	0.32 (4)	0.40	**silica**
GeO_2	0.43 (4)	0.54	silica
	0.55 (6)	0.68	**rutile**
TiO_2	0.60 (6)	0.745	**rutile**
	0.69 (8)	0.88	fluorite
SnO_2	0.67 (6)	0.83	**rutile**
	0.75 (8)	0.95	fluorite
ZrO_2	0.69 (6)	0.86	rutile
	0.78 (8)	0.98	**fluorite**
CeO_2	0.76 (6)	0.94	rutile
	0.89 (8)	1.11	**fluorite**
ThO_2	0.97 (8)	1.20	**fluorite**
CdF_2	0.98 (8)	1.21	**fluorite**
CaF_2	1.08 (8)	1.26	**fluorite**

Table 1.2:The radius ratio and structure type of a number of MX_2 ionic compounds.

The cubic fluorite structure is shown in Figure1.4It consists of a close packed array of zirconium ions with oxygen occupying all the tetrahedral sites. In the fluorite structure, with F_m3_m symmetry, the zirconium and oxygen ions are located at the following sites:

Atom	Position	Fractional co-ordinates
Zr	4 (a)	0 0 0
O	8 (c)	¼ ¼ ¼ } +(000, ½½0, ½0½, 0½½)
		¾ ¾ ¾ }

1.2.1 Aliovalent doping

It is possible for zirconia to undergo solid solution formation with MgO, CaO, Y_2O_3 and rare earth oxides[11]. By introducing aliovalent dopants such as Mg^{2+}, Ca^{2+} and Y^{3+} into the zirconia, the tetragonal and cubic polymorphs of zirconia can be stabilised at room temperature. Such a stabilisation involves the substitution of an aliovalent cation for zirconium, with an corresponding introduction of oxygen vacancies as the charge compensating species. This substitution reaction is shown in equations 1 and 2, using the Kröger-Vink notation (Appendix 1) for M^{2+} and M^{3+} respectively. The introduction of oxygen vacancies leads to oxide-ion conductivity in doped zirconia due to the decrease in co-ordination number.

$$MO \xrightarrow{ZrO_2} M_{Zr}'' + V_O^{\bullet\bullet} + O_O^{x} \qquad \text{Equation 1}$$

$$M_2O_3 \xrightarrow{ZrO_2} 2M_{Zr}' + V_O^{\bullet\bullet} + 3O_O^{x} \qquad \text{Equation 2}$$

As the ionic radii of the aliovalent dopant are larger than those of the zirconium cation, the tetragonal and cubic polymorphs of zirconia are easily stabilised at lower temperatures due to the increase in the average cation

Figure 1.4: The cubic-fluorite structure

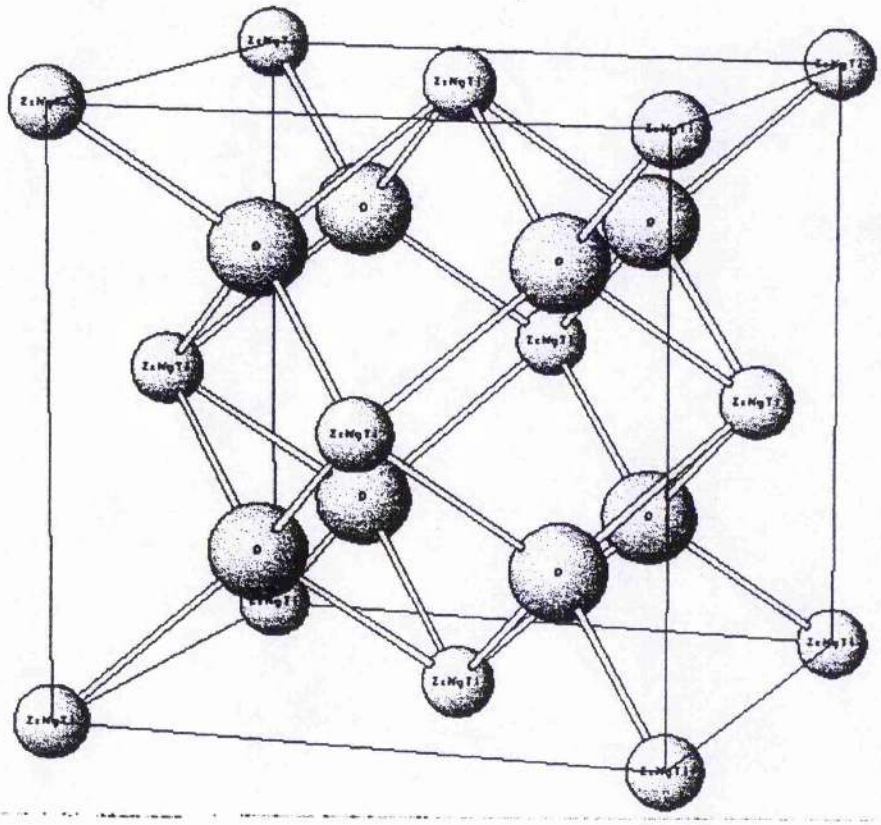

radius. This leads to an increase in the radius ratio which allows an increase in cation co-ordination from 7-fold to 8-fold. For example, from the zirconia-rich region of the ZrO_2-Y_2O_3 equilibrium phase diagram, it can be seen that by increasing the amount of dopant added reduces the temperature of the cubic-tetragonal phase-boundary (Figure 1.5). Table 1.3 shows the ionic radii of some dopant cations (8-fold coordination) which are commonly used to stabilise the cubic zirconia polymorph to room temperature illustrating the larger ionic radii of the dopant cation.

Cation	Ionic Radii (Å)
Zr^{4+}	0.98
Mg^{2+}	1.03
Ca^{2+}	1.26
Y^{3+}	1.15
Gd^{3+}	1.20
Ce^{4+}	1.11

Table 1.3 : Ionic radii of some dopant cations which could be used to stabilise ZrO_2

The stabilisation of cubic and tetragonal polymorphs of zirconia is possible by the addition of larger tetravalent ions like Ce^{4+} [12], again illustrating the stabilising effect of increasing the radius ratio through doping.

One of the most extensively studied stabilised-zirconia systems is the binary ZrO_2-Y_2O_3 phase system[13,14] due to its wide range of properties obtained with different solid solution compositions and heat treatments. Other stabilised-zirconia systems such as the MgO:TiO_2:ZrO_2 phase system have not been as extensively studied, but show promise for further investigation.

1.3 The Chemistry of Magnesium Titanate

1.3.1 Introduction

The ternary MgO-TiO-O system contains a number of binary joins which may give rise to solid solution formation. These are associated with the

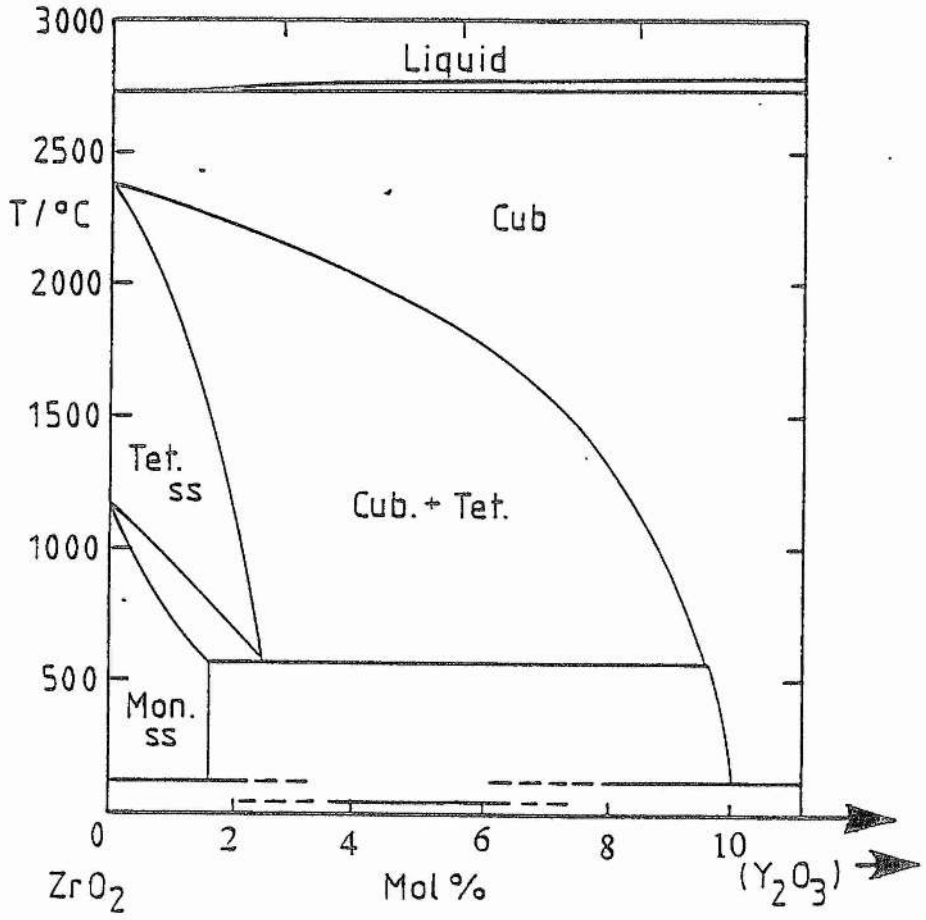

Figure 1.5: Phase diagram of the zirconia rich region of the ZrO_2-Y_2O_3 system[14]

pseudo-brookite (Ti_3O_5-$MgTi_2O_5$), the spinel ($MgTi_2O_4$-Mg_2TiO_4), the corrundum-ilmenite (Ti_2O_3-$MgTiO_3$) and rocksalt (MgO-TiO) structures (Figure 1.6). More recent investigations have revealed solid solution formation in the spinel[15,16], ilmenite[17,18] and pseudobrookite systems[19]. Such systems are thought to exhibit high electrical conductivity at low oxygen partial pressures, thus making them possible candidates for insertion into an anode of a solid oxide fuel cell. In this section, discussion is restricted to the spinel structure and its interesting properties.

1.3.2 The Structure of Magnesium Titanate Spinel and its properties

Magnesium titanate (Mg_2TiO_4) is known to exist in the inverse spinel form. Spinels take their name from the mineral $MgAl_2O_4$ whose structure was first determined by Bragg[20] and Nishikawa[21]. The spinel structure (Figure 1.7) has the general formula AB_2O_4 in which A and B can be from a wide variety of cations.

In the spinel structure, the anions form a face-centred cubic lattice with 64 tetrahedral 'A' sites and 32 'B' octahedral sites, of which only 8 and 16 respectively are occupied[6]. This enables us to write a general formula for the spinel structure as $A^{tet}B_2{}^{oct}O_4$. In the case of $MgAl_2O_4$, the Mg^{2+} ions are present in the tetrahedral sites with the Al^{3+} ions in the octahedral sites.

Inverse spinels, of which Mg_2TiO_4 is an example, exist where the A ions and half the B ions interchange positions to give $B^{tet}[AB]^{oct}O_4$. The spinels $MnFe_2O_4$ and $MgFe_2O_4$ are known as intermediate spinels as their cation arrangements lie between the extremes of normal and inverse spinels.

The spinels crystallize with the space group F_d3_m, with their cation and anion sites at the following positions:

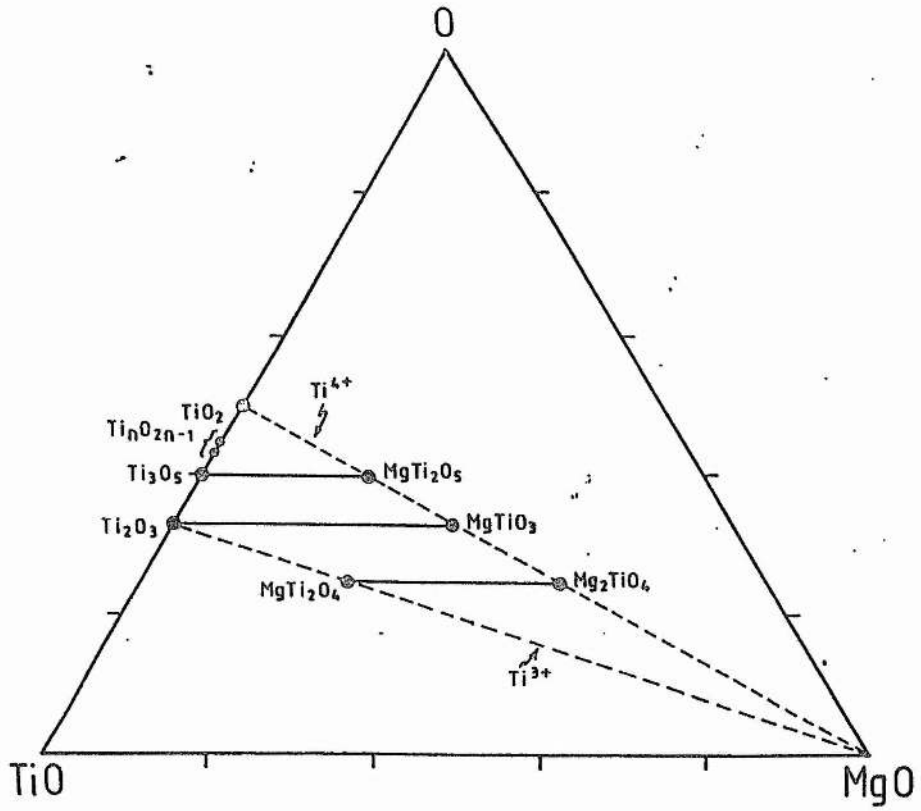

Figure 1.6 Phase relationships in the MgO-TiO-O system

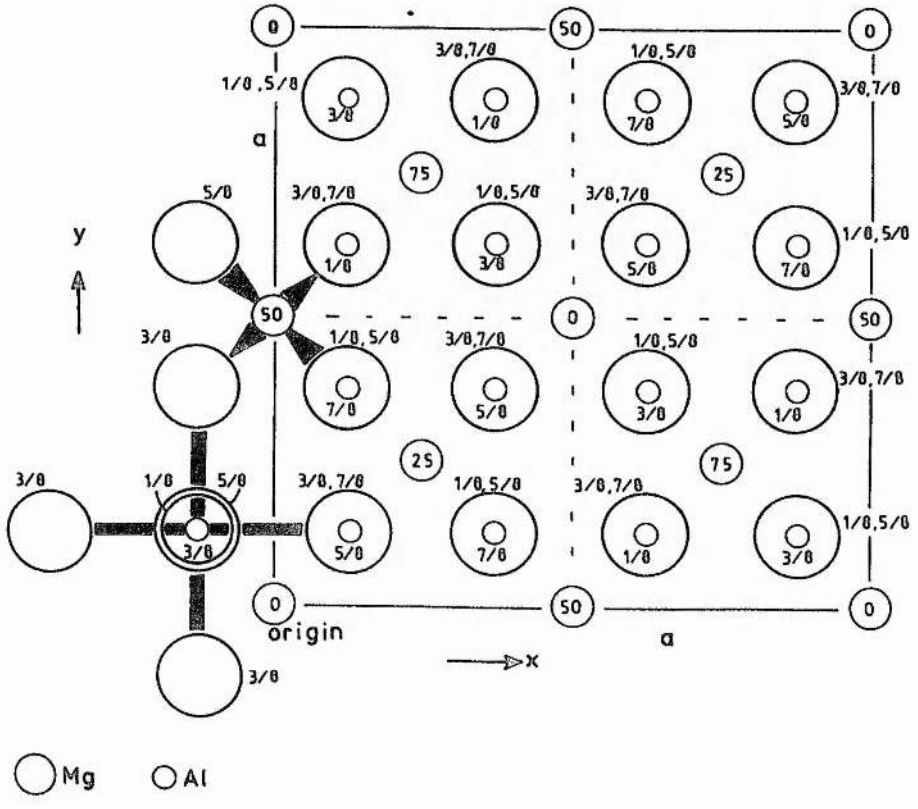

Figure 1.7 The spinel structure
(Adapted from West[6])

Atom	Position	Fractional coordinates
O	32e	$uuu; \bar{u}\bar{u}u; u\bar{u}\bar{u}; \bar{u}u\bar{u}$ $\frac{1}{4}-u, \frac{1}{4}-u, \frac{1}{4}-u; \frac{1}{4}+u, \frac{1}{4}-u, \frac{1}{4}+u;$ $\frac{1}{4}-u, \frac{1}{4}+u, \frac{1}{4}+u; \frac{1}{4}+u, \frac{1}{4}+u, \frac{1}{4}-u$ + face centring
B	16d	$\frac{5}{8}\frac{5}{8}\frac{5}{8}; \frac{5}{8}\frac{7}{8}\frac{7}{8}; \frac{7}{8}\frac{5}{8}\frac{7}{8}; \frac{7}{8}\frac{7}{8}\frac{5}{8};$ + face centring
A	8a	$000; \frac{1}{4}\frac{1}{4}\frac{1}{4}$ + face centring

(where A and B represent different cations)

Much work has been carried out on the reduced magnesium titanate spinel solid solution ($MgTi_2O_4$-Mg_2TiO_4) as it exhibits superconductivity at temperatures of around 50K[22]. Such a high superconductivity transition temperature for a non-cuprate containing compound is rather unusual as previous research on other related systems have found much lower transition temperatures (e.g. for $LiTi_2O_4$ 13K[23]) for superconductivity.

Magnesium titanate spinels at high temperatures (20-1000K) exhibit thermally activated behaviour (E_a = 50-400meV) which is reminiscent of small polaron-type semiconductivity[24]. The high temperature stability and properties of magnesium titanate spinels have been investigated at temperatures up to 1500K and exhibit many properties suitable for insertion into an anode in solid oxide fuel cells such as the thermal expansion coefficient having a magnitude similar to that of yttria-stabilised zirconia[25]. However, the ionic conductivity values of Mg_2TiO_4 spinel are much lower than the ideal value of conductivity required (>10^2S/cm at 900°C with a solid oxide fuel cell operating potential of between -1.0 and -0.7V[26]) for the anode material. Insertion of a pentavalent cation such as niobium or tantalum into the TiO_2 starting material may increase the ionic conductivity due to the charge compensation caused by electronic defects[27].

1.4 An Introduction to the Chemistry of Solid Oxide Fuel Cells

1.4.1 Introduction

A fuel cell is basically an energy conversion device which is capable of providing electrical energy by means of electrochemical reactions[28]. Unlike a normal electrochemical cell, separate streams of fuel and air are fed continuously into the fuel cell where they react (Figure1.8)This, therefore means that so long as the fuel and the oxidant are supplied, the fuel cell is capable of producing electricity[29].

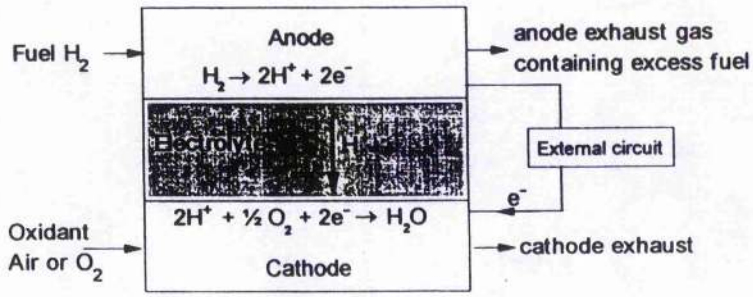

Figure 1.8: Principles of operation of an acid fuel cell schematic

As it can be seen from Figure 1.9 the fuel cell consists of three major components: the anode, cathode and the electrolyte. At the anode, the fuel gas is oxidised, thereby releasing electrons to the external circuit whereas at the cathode, the oxidant (like oxygen for example) is reduced by electrons from the external circuit. Ions are then conducted through the electrolyte to complete the circuit.

Various types of fuel cells have been produced since the reporting of the basic principles of fuel cell operation by Sir. William Grove in 1839[30] but one type of fuel cell which is receiving much attention is the solid oxide fuel

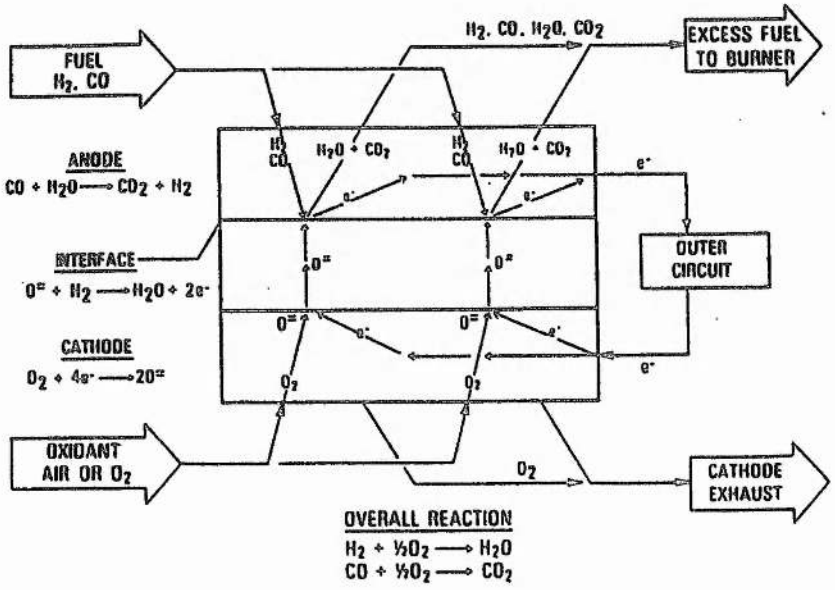

Figure 1.9: Schematic diagram of reactions occuring in SOFC's (adapted from Minh [29])

cell[31]. The solid oxide fuel cell is so called due to the choice of material selection being based mainly on metal oxides.

Solid oxide fuel cells operate at around 1000°C in order to encourage good conductivity and rapid reaction kinetics. Such a high temperature encourages the reforming of the fuel gases (ideally gases like methane) within the cell. The efficiency of the energy conversion is quite high due to minimal thermal losses during the energy transfer from chemical to electrical energy. Corrosion of the fuel cell is not a problem as there are no highly reactive metals present. As there are no liquids present in the solid oxide fuel cell, the cell can be manufactured into an unique shape for any particular application. Such a feature allows for cell design with additional performance. Economically, solid oxide fuel cells are potentially favoured over other fuel energy systems due to their low construction costs, very high energy efficiency and adaption to local circumstances.

1.4.2 Choice of materials problem

The major stumbling block and consequently the most important factor in the construction of solid oxide fuel cells is the choice of materials. The component materials, themselves, must be chemically stable in the severe oxidising and reducing environments of the cathode and anode respectively. Materials with different thermal coefficients will cause fractures and cracks in the cell on heating and cooling of the gases when mixed. The electrolyte should ideally be very dense to prevent gases from mixing during normal operating conditions with the electrodes being porous to facilitate the movement of the gases to their respective reactive sites.

Obviously, the materials must also be able to conduct in the correct manner at the operating temperature. The electrolyte itself should only conduct ionically as electronic conduction reduces the efficiency of the energy conversion process. It is advantageous that the electrode conduct both

ionically and electronically as it increases the surface area of reaction. Figure 1.9 is the schematic diagram of a simple solid oxide fuel cell.[29] The oxidant (oxygen gas) is fed into the cathode, where it is reduced to provide O^{2-} ions. Such ions are then transferred *via* the electrolyte to the anodic component (fuel electrode). The fuel (hydrogen gas) is fed to the anode, where it gets oxidised by O^{2-} producing water and electrons (Equation 3), which are passed to the external circuit.

$$H_2 + O^{2-} \longrightarrow H_2O + 2e^- \quad \text{(Equation 3)}$$

1.4.3 Selection of materials for the electrolyte

The main areas of research for a suitable electrolyte have centred upon the need for the material to be stable, flexible and easily synthesised as well as being a good ionic conductor[32]. Promising results have been obtained for yttria stabilised zirconia (Y_2O_3-ZrO_2) as it has been shown to have an acceptable ionic conductivity, very little electronic conductivity[13] and a thermal expansion coefficient of 10.8×10^{-6} K^{-1} for $(Y_2O_3)_{0.08}$ $(ZrO_2)_{0.92}$[33]. However, yttria stabilised zirconia can suffer structural damage after prolonged periods of use and on heating and cooling[55].

Other materials that have been investigated include the cubic fluorite phase of stabilised δ-bismuth-sesquioxide (Bi_2O_3) which exhibits ionic conductivity of at least one to two magnitudes higher than yttria stablilised zirconia[34]. Unfortunately stabilised δ-Bi_2O_3 is easily reduced at low oxygen partial pressures to bismuth metal. This means that it is necessary to protect the material from reducing conditions[35].

1.4.4 Selection of materials for the cathode

Doped lanthanum manganite is the current cathode material used in solid oxide fuel cells due to its high electronic conductivity in oxidising

atmospheres, adequate compatibility with ytrria stabilised zirconia based electrolytes and a similiar thermal expansion coefficient to other fuel cell components[36]. By substituting La^{3+} in $LaMnO_3$, a p-type perovskite with Sr^{2+}, one can improve the conductivity by increasing the Mn^{4+} content[37] (see equation 4).

$$LaMnO_3 \xrightarrow{SrO} La^{3+}_{1-x}Sr^{2+}_{x}Mn^{3+}_{1-x}Mn^{4+}_{x}O_3 \qquad \text{(Equation 4)}$$

By substituting 10mol% Sr^{2+}, an increase in electronic conductivity from 75 to 125 Scm^{-1} at 1000°C is noted[37]. The thermal expansion coefficient of $LaMnO_3$ is quite similar to that of yttria stabilised zirconia ($11.2 \times 10^{-6}\ K^{-1}$) and increases slightly upon the addition of strontium. A significant problem which has recently received much attention is the reaction between the cathode and electrolyte during co-sintering and in reducing atmospheres during fuel cell temperatures resulting in poorly conducting phases such as $La_2Zr_2O_7$ which increase ohmic losses and reduce fuel cell performance[38].

1.4.5 Selection of interconnecting materials

The properties required for the interconnecting material are probably the most stringent of all the fuel cell components. In addition to having high electronic conductivity and comparable thermal expansion to yttria stabilised zirconia electrodes, the interconnect must be stable in both oxidising and reducing atmospheres and have a high sintered density to prevent cross-diffusion and mixing of fuel and oxidant gases. The most commonly used material is lanthanum chloride which has similar properties to the cathode material with respect to its electronic conductivity and thermal expansion. However, the one significant difference between the cathode and interconnecting material is the very high density required for the latter which has proved to be rather difficult to obtain[39]. By producing highly reactive powders, sintering of $LaCrO_3$ to near full density in air has been made possible[39].

1.4.6 Selection of materials for the anode

The anode material currently used is a nickel/yttria-stabilised zirconia cermet, which incorporates active particles of nickel in an inactive yttria-stabilised zirconia support[40]. In order to provide very high electronic conduction as well as protection from the reducing conditions of the anode, metals are used as anode materials. The metal which satisfies these conditions as well as its low cost and high catalytic activity is nickel.

Oxidation of the fuel at the anode involves the adsorption of the fuel onto the nickel as shown in equations 5 and 6:

$$H_2 + 2Ni \leftrightarrow 2NiH \qquad \text{(Equation 5)}$$

$$2NiH + O_o^x \leftrightarrow H_2O + 2Ni + V_o^{\circ\circ} + 2e^- \qquad \text{(Equation 6)}$$

The nickel metal is dispersed in yttria-stabilised zirconia to support the nickel particles, to prevent the fusion of the nickel particles at high temperatures and to help match the thermal expansion of the electrolyte.

One problem of using the nickel-yttria stabilised zirconia material is that nickel particles sinter on long term operation, thus reducing the contact area required for conductivity[41]. It has also been found that the nickel metal, which has a low sulphur tolerance reacts with the sulphur impurities found in the fuel gas to give NiS which, in turn, reduces the active surface area and therefore the conductivity of the material.

1.4.7 Cell Design and Fabrication

Several cell configurations have been proposed: seal-less tubular design, segmented cell-in-series design, monolithic design and flat plate design[29] (Figure 1.10). All of these designs involve the basic structure of the simple fuel cell (Figure 1.8). Unfortunately, due to the cells having a rather low voltage output (typically below 1V DC[42]), the cells tend to be used in series or in parallel; such cells are known as 'stacks'. These 'stacks' have already been tested at power outputs of between 135W and 1kW[28].

The seal-less design, devised by Westinghouse is probably the most advanced of all the cell configurations proposed. Such a cell configuration involves supporting layers of anode, cathode and electrolyte material on a porous support tube, closed at one end[43]. For cell operation, oxygen flows inside the cell on the outside of the support tube. An advantage of this design is the simple separation of the gases *via* the support tube, eliminating the need for gas-tight seals as the production of gas tight seals has been a major design problem. The main disadvantages of this cell configuration is the rather poor gas diffusion through the support tube which leads to poor cell performance as well as the complex procedure of applying the electrode and electrolyte layers onto a curved support tube. Such cells have been tested for periods up to 3000 hours with typical cell performance of about 0.68V at 250mA/cm^2, 0.17W/cm^2 [43].

The monolithic design devised by Argonne National Laboratory, incorporates a complex corrugated structure which allows for separate gas flows, eliminating the need for gas tight seals. Such a design allows a high power density with low resistance losses which means that the cell can be operated at high currents[29]; however, the fabrication of the corrugated layer and the eventual scaling up of the design pose a major problem. Monolithic cells have been operated at 2.2A/cm^2 [44], 1.5W/cm^2 at 0.7V.

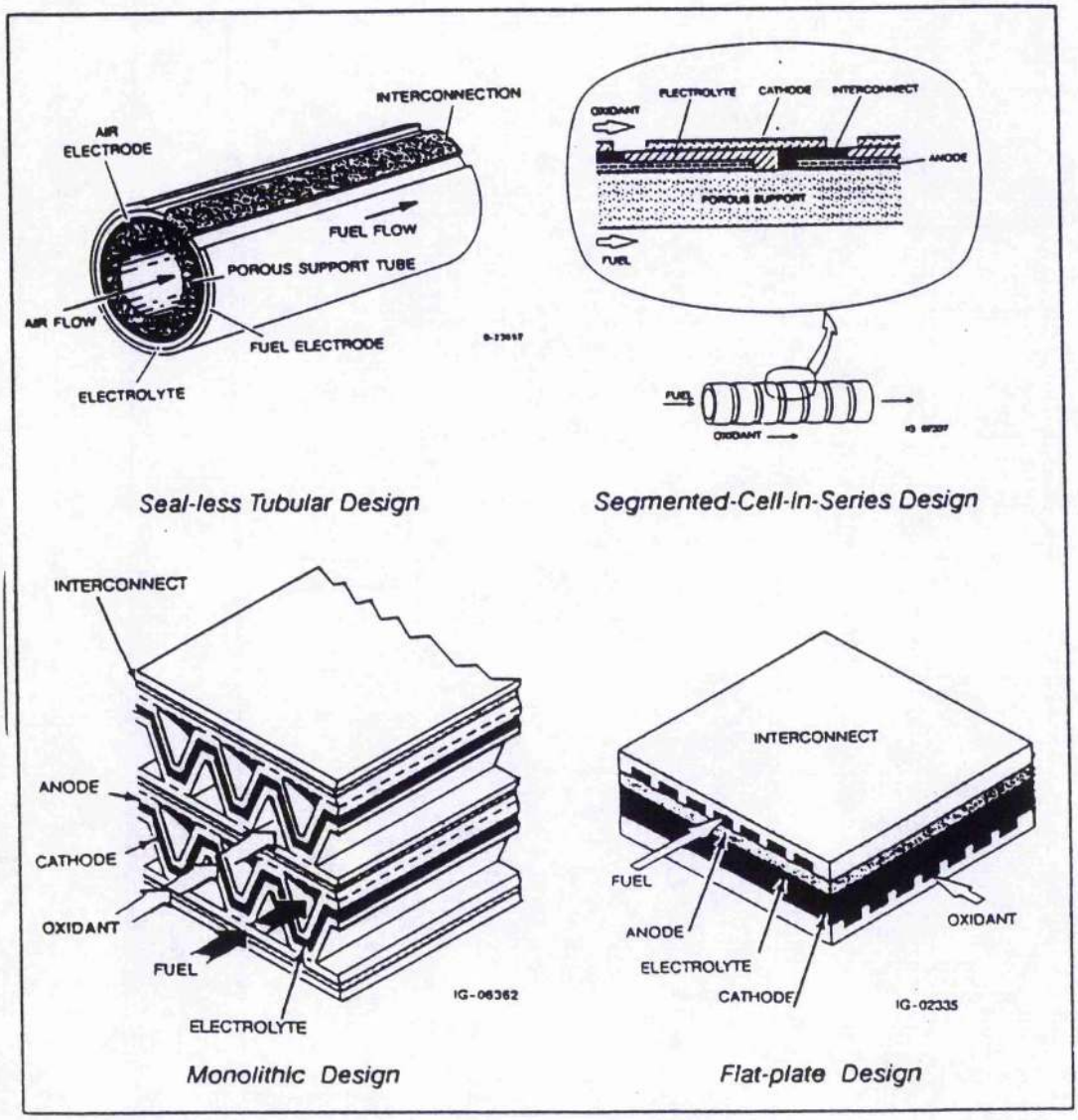

Figure 1.10 Current solid oxide fuel cell designs
(adapted from Minh [29])

The simplest design of the fuel cell components is the flat plate stack. This design, due to its simplicity requires gas tight seals along the edges of the ceramic plates. As the resistance of the cell depends only on the thickness of the component layers, the production of ultra-thin plates will minimise the resistance. By producing thin cell component plates which have very liittle resistance, there is the possibility of lower operating temperatures. Thin plate designs have produced power densities of $0.2W/cm^2$ [45].

The different cell configurations have led to a variety of methods of depositing/fabricating fuel cell components such as electro-vapour deposition, tape casting[46] and calendering[47]. Using yttria-stabilised zirconia electrolytes of thickness of 1-10μm by such methods have led to high power densities at low temperatures[48] such as $0.55W/cm^2$ at 800°C and $0.91W/cm^2$ at 1000°C, using hydrogen gas as a fuel.

1.4.8 Summary

Solid oxide fuel cells offer a cleaner alternative means of producing electrical energy; however, there are still problems to be overcome namely, materials selection for the fuel cell components and the design of the 'stacks' and even, then, if competing technologies improve their efficiency, solid oxide fuel cells may not become a commercial reality.

1.5 Mixed-conducting oxides

It is desirable to develop ceramic materials which exhibit good mixed-conducting properties at low oxygen partial pressures for practical applications such as electrode materials for solid oxide fuel cells, catalytic materials and oxygen sensors[49]. By combining both good oxide-ion conductivity with high electronic conductivity, it will be possible to attain an increased surface area for electrode reaction and therefore an increase in the efficiency.

One class of ceramics which are likely to meet those criteria are the fluorite-based metal oxides. It is possible to dope those oxides with early transition metals like Ti and Nb, so that electronic conductivity can be induced in reducing atmospheres. Unfortunately, very high levels of doping are likely to be required to achieve reasonable levels of electronic conduction and such levels are thought to be detrimental to ionic conductivity.

One of the most extensively studied high temperature oxide-ion conductors which has the cubic fluorite structure is yttria-stabilised zirconia[50,51,52]. Conduction occurs *via* the migration of oxygen vacancies, which are the charge compensating species introduced as a result of aliovalent doping. Over a wide range of oxygen partial pressures, 1 - 10^{-18} atm, the ionic transport number is close to unity[53], indicating that conduction is purely ionic. Ionic conductivity is defined as:

$$\sigma = \sum_i n_i e_i \mu_i \qquad (1.1)$$

where n_i = number of charge carriers (number of oxygen vacancies)

e_i = charge of carrier

μ_i = mobility of carrier

and ionic conductivity, σ, normally shows an Arrhenius type behaviour,

$$\sigma = A \exp (-E_a/kT) \qquad (1.2)$$

where E_a = the activation energy (eV)

A = pre-exponential factor

k = Boltzmann constant, 1.38 x 10^{-23} JK^{-1}

T = temperature (K)

For a given composition of yttria stabilised-zirconia, i.e. a fixed number of oxygen vacancies, the ionic conductivity increases with temperature in a

typical Arrhenius fashion with an activation energy of about 1 eV[53]. Figure 1.11 shows the Arrhenius plots for a variety of oxide-ion conductors[54]; the shaded area represents the desirable values for practical applications. As it can be seen from Figure 1.11, the oxide-ion conductivities of stabilised zirconias are not the highest, as the highest values of oxide-ion conductivity are observed in doped and undoped δ-Bi_2O_3 and doped ceria. It should be noted, however, that doped and undoped δ-Bi_2O_3 undergo phase transitions between 500 and 700°C and doped ceria may become electronically conductive under reducing conditions. The high conductivity observed between 800 and 1000°C and the absence of any notable phase transitions suggests that yttria-stabilised zirconia may be a useful high temperature oxide-ion conductor but at temperatures of between 500 and 700°C a decrease in activation energy is noted with increasing temperatures. This phenomen is due to vacancy-cation association[55].

Figure 1.12 illustrates the variation of ionic conductivity with dopant concentration, for a variety of dopants, at 800°C [56]. As the amount of dopant is increased, the amount of oxygen vacancies increases; an increase in conductivity with increasing dopant concentration may be expected. In reality, the conductivity reaches a maximum value for dopant concentrations between 8 and 14 mol%; different dopant types produce maxima in the ionic conductivity at different dopant concentrations. Table 1.4 lists the ionic radii of the different dopant cations; for a fixed dopant content, large ionic radii of a dopant and lower dopant cation valences generally result in lower values of conductivity being recorded.

Cation	Ionic Radii (Å)
Zr^{4+}	0.98
Yb^{3+}	1.12
Gd^{3+}	1.20
Y^{3+}	1.16
Ca^{2+}	1.26
Nd^{3+}	1.26

Table 1.4: Ionic radii of the dopant cations used to stabilise ZrO_2 in Figure 12[10]

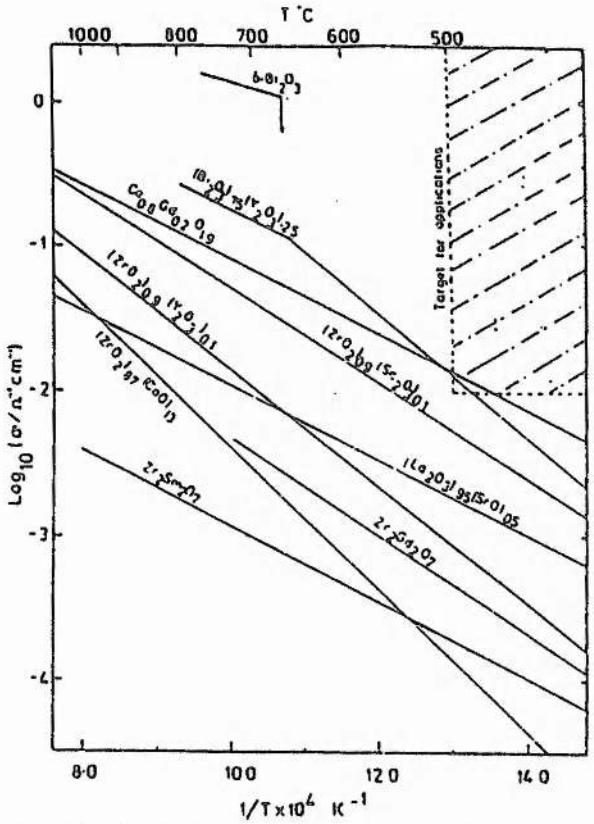

Figure 1.11 The ionic conductivities for some high temperature oxide-ion conductors, showing the desirable values for practical applications [54].

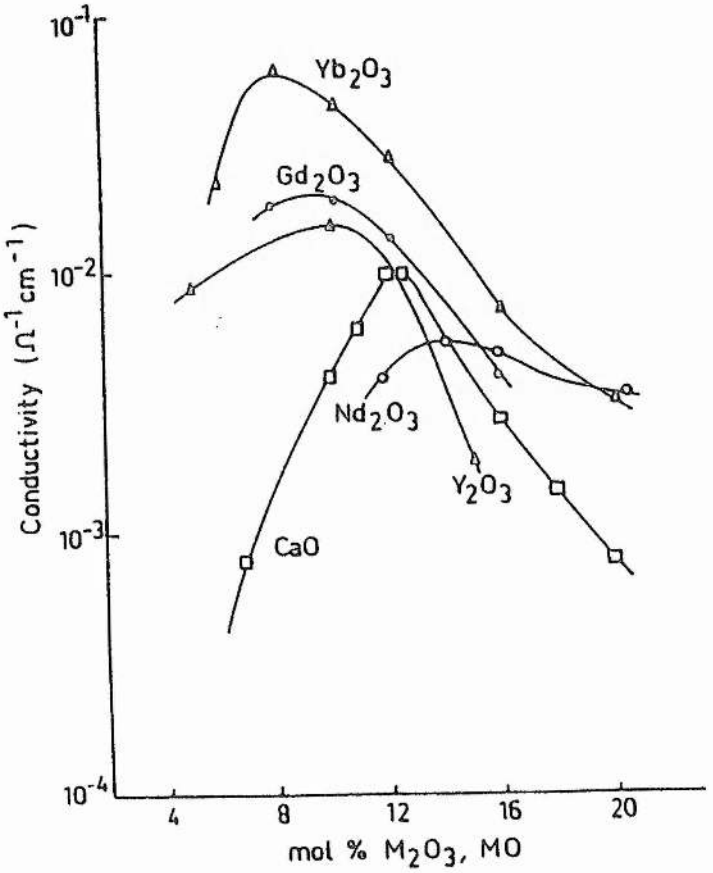

Figure 1.12 Variation of conductivity with dopant concentration for various doped zirconias (T=800°C) [56].

After the conductivity has reached a maxima, a large and dramatic decrease in conductivity is noted, due to the interaction of the oxygen vacancies with the cations, thereby reducing the mobility of the oxygen vacancies.

Titanium-substituted zirconias give the excellent electronic conductivity properties required for a ZrO_2 based fluorite material[58] but problems have been encountered such as a decrease of the unit cell size on reduction[27]. Some related systems such as the $MgO:ZrO_2:TiO_2$ phase system have not been as extensively researched with respect to oxide-ion conductivity but should provide some interesting results for analysis.

1.6 Phase diagrams

1.6.1 Introduction

The field of phase equilibria and phase diagrams is one of the cornerstones of solid state chemistry. Phase diagrams are plots of temperature (occasionally pressure) against composition. They summarize in graphical terms the ranges of temperature and composition over which certain phases or mixture of phases exist under conditions of thermodynamic equilibrium. This means that the effect of temperature on solids and the reactions that may or not occur between solids can therefore be easily deduced from the appropriate phase diagram.

The fundamental rule on which phase diagrams are based upon is the *phase rule* developed by W.J. Gibbs. It is defined as:

$$F = C - P + 2 \qquad (1.3)$$

where F = the number of degrees of freedom

C= the number of components

P = the number of phases

The quantity, F, deals with the number of variables that have to be specified to define the system completely, and usually includes the concentration of each phase present. This number is also called the variance or the number of degrees of freedom. In a system of two different chemical substances, if one has a concentration that has a mole fraction of 0.4, the concentration of the other is fixed at 0.6 because the sum of the two must be 1.0. The variance in concentration is therefore 1 not 2 [6].

The number of components, C, is the smallest number of independently variable chemical compounds that must be specified in order to describe the composition of each phase present in the system. For example, in the system liquid water, ice and water vapour, there is only one chemical present, namely water.

The number of phases is the number of physically distinct and mechanically separable portions of a system, each phase being itself homogeneous. The distinctions between different crystalline phases is usually clear. For example, the differences between chalk, $CaCO_3$, and sand, SiO_2, are obvious. The distinction between crystalline phases made from the same components but of different composition is also usually clear. Thus, the magnesium silicate minerals enstatite, $MgSiO_3$, and forsterite, Mg_2SiO_4 are different phases. They have very different composition, structure and properties. With some solids, it is possible to get different crystalline phases having the same chemical composition. This phenomen is known as *polymorphism* (see Section 1.2). For, example, the two polymorphs of Ca_2SiO_4 can be prepared at room temperature, the stable γ form and the metastable β form, but these have quite distinct physical and chemical properties and crystal structures[6].

1.6.2 Binary Phase Diagrams

Two component or binary systems have three independent variables: pressure, temperature and composition. In most systems of interest in the general area of solid state chemistry, the vapour pressure remains low for large variations in temperature and so, for work at atmospheric pressure, the vapour phase and the pressure variable need not be considered. In binary systems under these conditions an invariant phase occurs where three phases co-exist in equilibrium: an unvariant curve for two phases and a bivariant condition for one phase. Conventionally, temperature is the vertical scale and composition is the horizontal one in binary phase diagrams.

In the MgO-TiO_2 phase diagram (Figure 1.13), there are three intermediate compounds present: ilmenite ($MgTiO_3$), spinel (Mg_2TiO_4) and distorted pseudobrookite (Mg_2TiO_5). The distorted pseudobrookite and spinel species were found to be unstable at room temperature due to the configurational entropy arising from cation disorder. Phase diagram studies by Wechsler and Navrotsky[58] reveal that at 1500°C with an approximate MgO content of 67mol%, the spinel structure is present. With a 1:1 ratio of magnesium oxide to titanium oxide, the ilmenite structure crystallizes. At 33 mol% MgO, the distorted pseudobrookite structure is formed.

For the MgO-ZrO_2 binary system, it was found that the Mg^{2+} ions can stabilize zirconia to form the cubic-fluorite structure[59] but the exact boundaries of the range of where the cubic-fluorite structure is formed have been the subject of much controversy. One early reference[60] (Figure 1.14) suggests that the phase range is between 15% mol and 25% mol of MgO at 1500°C but a later reference[61] (Figure 1.15) by the same person suggests that at 1500°C, the cubic-fluorite phase range is between 10% mol and 15% mol of MgO. It was also noted that by adding excess MgO to zirconia at temperatures in excess of 1400°C can lead to MgO being precipitated outwith

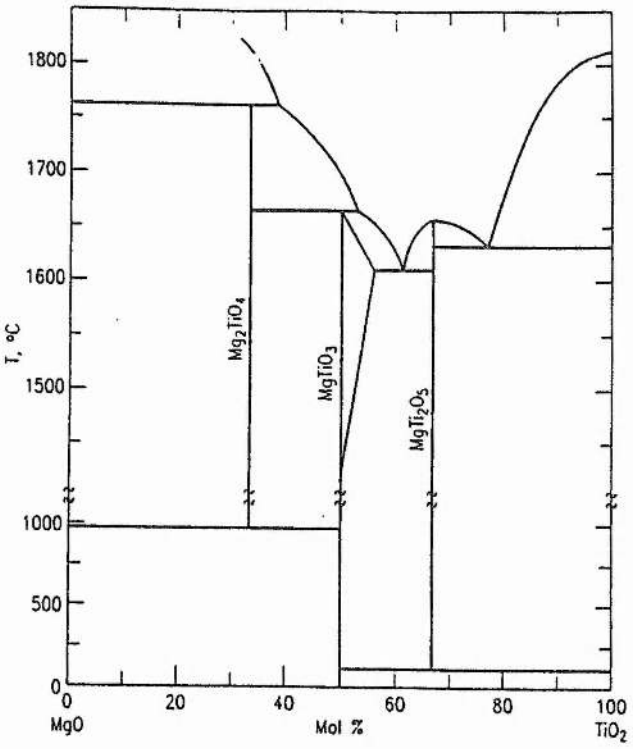

Figure 1.13 The MgO:TiO_2 phase diagram
Adapted from ref [59]

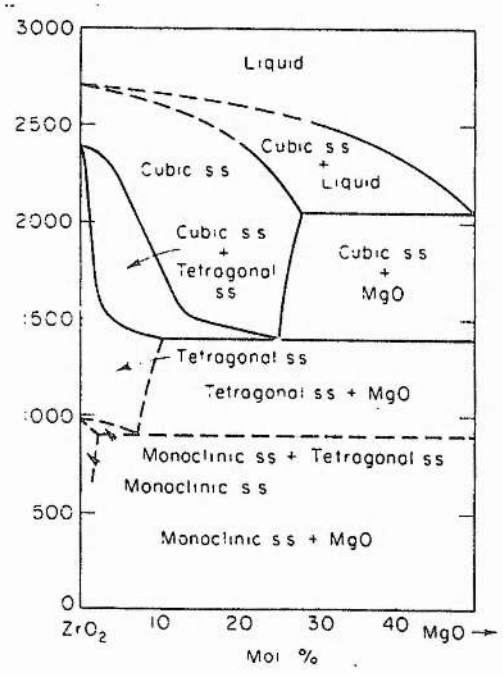

Figure 1.14 An early version of the MgO:ZrO_2 phase diagram
Adapted from ref [60]

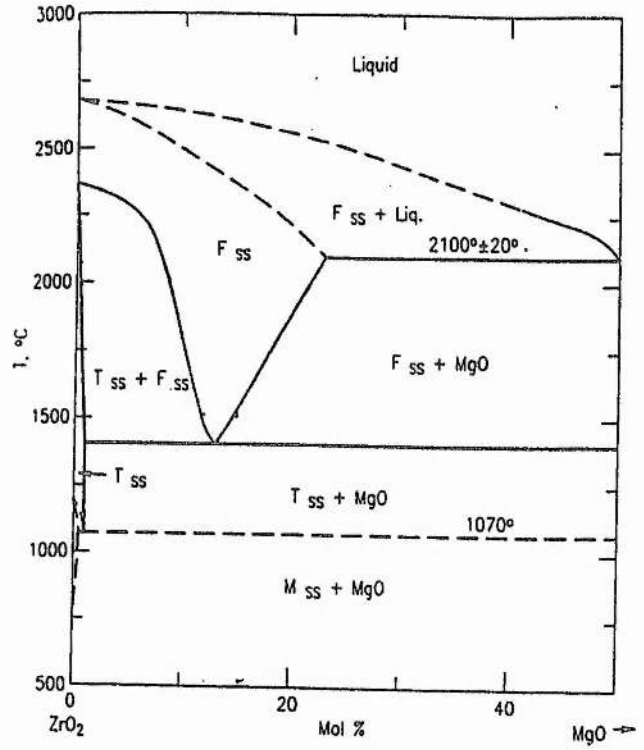

Figure 1.15: Revised version of the $MgO:ZrO_2$ phase diagram where M= monoclinic phase, T= tetragonal phase and F= cubic fluorite phase. Adapted from ref [61]

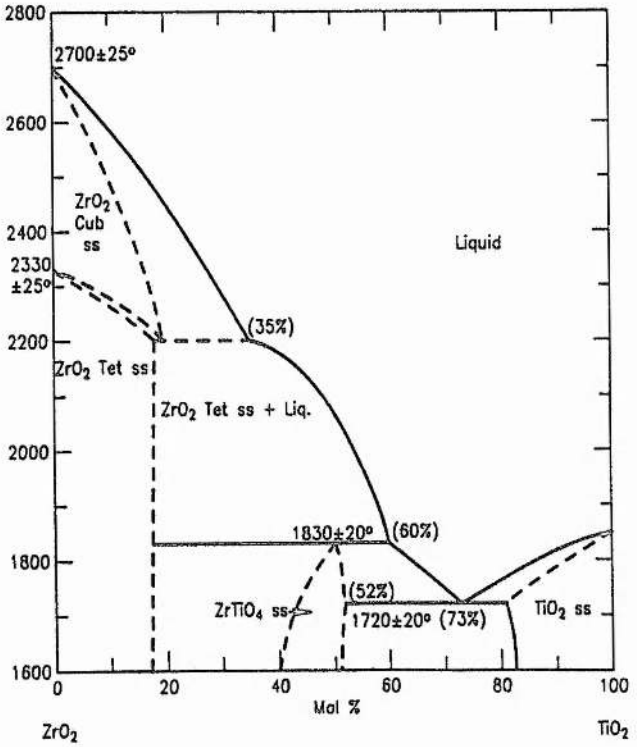

Figure 1.16: The $TiO_2:ZrO_2$ phase diagram
Adapted from ref [62]

the cubic-fluorite structure, leading to MgO peaks being observed, in addition to the cubic-fluorite structure.

The TiO_2-ZrO_2 binary system has been investigated by Shevchenko et al[62] (Figure 1.16) and consists mainly of a mixture of certain phases with very few significant single phase regions. As Ti^{4+} has a slightly smaller ionic radius than Zr^{4+} itself, it is unlikely that Ti^{4+} can stabilize the cubic-fluorite structure to room temperature (Section 1.2.1) leading to the fact that the cubic-fluorite structure will only exist at high temperatures (> 2330°C) with low concentrations of TiO_2 (< 18% mol). However, single phase samples of $ZrTiO_4$ have been characterized and were found to crystallize with the orthorhombic structure[63].

1.6.3 Ternary Phase Diagrams

Three component or ternary systems have four independent variables: pressure, temperature and the composition of the two components. If the composition or concentration of two of the components in a particular phase is fixed, the third is automatically fixed by difference. In this section, for simplicity, the MgO:TiO_2:ZrO_2 phase system is not a volatile system, which means that the condensed phase rule, i.e. $P + F = C + 1 = 4$ can be applied. Under these conditions, the ternary system is, for example, invariant when four phases - generally three crystalline phases and liquid - coexist at one fixed temperature.

Ternary sytems can be represented by equilateral triangles and the three components form the three corners of the triangle. Temperature is represented by the vertical axis perpendicular to the plane of the triangle. A three-dimensional prism is needed to fully display the effects of varying composition and temperature. In order to display ternary equilibria on paper, it is sufficient to project the melting relations onto the composition triangle or to construct isothermal sections.

Ternary compostions within equilateral triangles are given by reference to a grid (Figure I.17). Each of the three binary edges are divided into a hundred divisions. Point A corresponds to 100% A: the edge BC corresponds to 0% A; and the line XY to 10% A. Thus, the A content of any ternary composition is given by drawing a line through that composition and parallel to the BC edge. The A content is then read off from the intersection of this line with either the AB or AC edges, respectively. Point P in Figure has a composition of 30% A, 45% B and 25% C. Compositions can be either in atom per cent, in mole per cent or in weight per cent. In practice, it is usually preferable to use mole per cent for inorganic systems because the formulae of binary and ternary phases are then clearly related to the composition[6].

The $MgO:TiO_2:ZrO_2$ phase diagram was studied by Coughanour et al[64]. In their analysis,for the study of ternary fields, some selected samples (Table I. 5) were subjected to suitable heat treatment and after quenching or cooling were analysed by X-ray techniques. It was found that no ternary compositions were observed but binary joins were established for the $MgTi_2O_5$-$ZrTiO_4$, $MgTi_2O_5$-ZrO_2, $MgTiO_3$-ZrO_2 and Mg_2TiO_4-ZrO_2 subsolidus equilibrium systems. The authors admit that not a very high degree of accuracy was used in determining the solid-solution limits as the heat treatments of the samples were inconsistent from one sample to another but claim that the phase diagram proposed (Figure I.18) shows the general trends of solid-solution formation.

The paper also suggests that single phase cubic-fluorite samples can be obtained within the ZrO_2-rich region by quenching the samples at temperatures in excess of 1400°C. However, if a slow cooling technique was employed, monoclinic ZrO_2, cubic ZrO_2 and some MgO would be observed. It was also noticed that within the ternary system, cubic zirconia solid solutions can be found which are stable to a greater or lesser extent depending upon the TiO_2 content of the specimen.

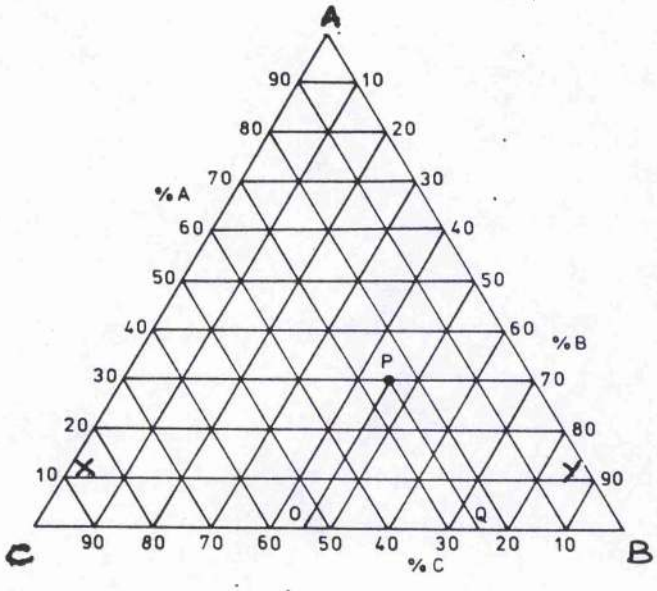

Figure 1.17 A ternary phase diagram .

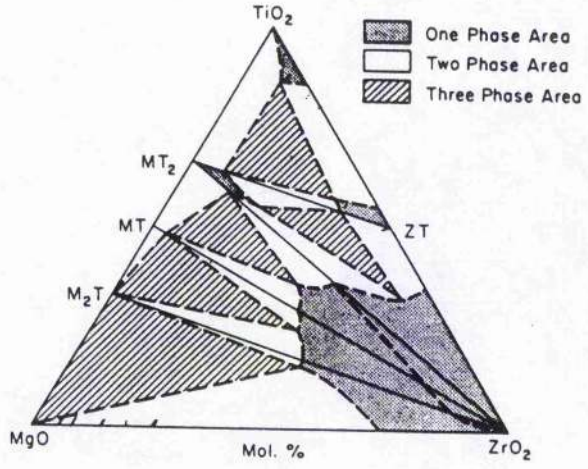

Figure 1.18 The $MgO:TiO_2:ZrO_2$ phase diagram

Adapted from ref [64]

Mole ratio M:Z:T	Binary join or ternary field	Heat treatment[a]		Phases identified by X-ray and/or petrographic means (all in solid-solution form, unless otherwise indicated)
		Time	Temperature	
		hr	*° C*	
13:5:31	MT_2-ZT	2	1,500	MT_2+ZT+trace TiO_2.
1:1:3	do	1	1,550	MT_2+ZT.
1:2:4	do	1	1,600	Do.
4:1:8	MT_2-ZrO_2	2	1,500	MT_2+trace MT (no ZrO_2 at all).
3:2:6	do	2	1,300	MT_2+monoclinic ZrO_2+trace ZT.
1:1:2	do	28	[b] 1,500	Do.
1:1:2	do	2	1,525	MT_2+monoclinic ZrO_2.
1:9:2	do	1	1,670	monoclinic ZrO_2+trace MT_2.
9:1:9	MT-ZrO_2	2	1,500	MT+trace monoclinic ZrO_2.
3:1:3	do	2	1,525	MT+monoclinic ZrO_2+trace MT_2.
3:2:3	do	1	1,610	MT+monoclinic ZrO_2+trace cubic ZrO_2.
1:1:1	do	1½	1,625	MT+monoclinic ZrO_2.
1:1:1	do	72	[b] 1,400	MT+cubic ZrO_2.
1:3:1	do	1½	1,750	Cubic ZrO_2+monoclinic ZrO_2+trace MT.
1:9:1	do	1½	1,700	Monoclinic ZrO_2+trace cubic ZrO_2.
10:1:5	M_3T-ZrO_2	2	1,500	M_3T[c]+small amount cubic ZrO_2.
6:1:3	do	2	1,500	M_3T[c]+cubic ZrO_2.
6:2:3	do	1	1,610	Do.
2:2:1	do	1½	1,750	M_3T[c]+cubic ZrO_2.
2:2:1	do	72	[b] 1,200	M_3T[c]+monoclinic ZrO_2[c].
2:3:1	do	1½	1,700	Cubic ZrO_2+trace M_3T[c].
2:4:1	do	1½	1,750	Cubic ZrO_2.
1:1:4	MT_2-ZT-TiO_2	1	1,425	MT_2+ZT+TiO_2.
1:1:9	do	1	1,425	MT_2+TiO_2+trace ZT.
1:1:19	do	2	1,550	TiO_2+MT_2.
1:3:9	do	1	1,425	TiO_2+MT_2+ZT.
2:3:6	MT_2-ZT-ZrO_2	2	1,500	MT_2+ZT.
1:2:3	do	5	1,450	MT_2+ZT+monoclinic ZrO_2.
2:1:3	MT-MT_2-ZrO_2	4	1,450	MT_2+cubic ZrO_2+MT.
2:6:3	do	16	[b] 1,500	Cubic ZrO_2+monoclinic ZrO_2.
3:2:2	M_3T-MT-ZrO_2	1½	1,625	M_3T[c]+MT+cubic and monoclinic ZrO_2.
3:3:2	do	1	1,610	M_3T[c]+cubic ZrO_2.
3:3:1	MgO-M_3T-ZrO_2	1½	1,650	Cubic ZrO_2+MgO[c]+trace M_3T[c].
5:5:1	do	1½	1,650	Cubic ZrO_2+MgO[c].
1:9:0	MgO-ZrO_2	1	1,670	Cubic ZrO_2+monoclinic ZrO_2.
1:9:0	do	72	[b] 1,490	Cubic ZrO_2.
1:9:0	do	80	[b] 1,200	Monoclinic ZrO_2+small amount MgO.[c]
1:4:0	do	1	1,610	Cubic ZrO_2+small amounts of MgO[c] and monoclinic ZrO_2.
1:1:0	do	1	1,610	Cubic ZrO_2+monoclinic ZrO_2+MgO.[c]
1:1:0	do	48	[b] 1,515	Cubic ZrO_2+MgO.[c]
1:1:0	do	80	[b] 1,200	Monoclinic ZrO_2+MgO.[c]

[a] Each sample had been calcined at least once prior to the recorded heat treatment and cooled slowly, unless otherwise indicated.
[b] The specimen was quenched from the temperature indicated.
[c] No solid-solution formation was noted in this substance.

Table 1.5: Literature results of solid state reactions in the $MgO:TiO_2:ZrO_2$ system

1.7 Conclusions

As it can be seen from this literature review that the $MgO:TiO_2:ZrO_2$ phase diagram has not been well studied. As titanium stabilised zirconias have the excellent electronic conductivity required for a ZrO_2-based fluorite material but problems have been encountered such as a decrease in unit cell size upon reduction under Solid Oxide Fuel cell conditions. This might be overcome by the addition of an aliovalent cation such as Mg^{2+}. By constructing an accurate phase diagram of the $MgO:TiO_2:ZrO_2$ system at high temperatures, it will be possible to assess its suitability with respect to stability and its ability to perform under strongly oxidising/reducing conditions.

1.8 References

1- L.K. Lenz and A.H. Heuer, *J. Am. Cer. Soc.*, 1982, **65**, 192-194.

2- J.D. McCullough and K.N. Trueblood, *Acta. Cryst.*, 1959, **12**, 507-511.

3- G. Teufer, *Acta. Cryst.*, 1962, **15**, 1187-1188.

4- D.K. Smith and C.F. Cline, *J. Am. Cer. Soc.*, 1962, **45**, 249-250.

5- A.R. West, *Basic Solid State Chemistry*, John Wiley and Sons, Chichester, 1991.

6- A.R. West, *Solid State Chemistry and its applications*, John Wiley and Sons, Chichester, 1990.

7- A. Wold and K. Dwight, *Solid State Chemistry*, Chapman and Hall, London, 1993.

8- R. C. Garvie, *J. Phy. Chem.*, 1965, **69**, 1238-1243.

9- T. Okubo and H. Nagamoto, *J. Mat. Sci.*, 1995, **30**, 749-757.

10- R.D. Shannon and C.T. Prewitt, *Acta. Cryst.*, 1969, **B25**, 925-946.

11- V. Stubican in: *Advances in Ceramics*, Vol 24, eds. S.Somiya, N. Yamamoto and H.Yanagida (The American Ceramic Society, Columbus, OH, 1988), 71-82.

12- M. Yoshimura, E. Tani and S. Somiya, *Solid State Ionics*, 1981, **3/4**, 477-481.

13- I.R. Gibson, *Ph.D. Thesis*, University of Aberdeen, 1995.

14- C. Pascual and P. Duran, *J. Am. Cer. Soc.*, 1983, **66**, 23-27.

15- T.J. Cogle, C.A.S. Mateus, J.H. Binks and J.T.S. Irvine, *J. Mater. Chem*, 1995, **1**, 289.

16- A. Feltz, M. Steinbruck, *J. Less-Common Met.*, 1991, **167**, 233.

17- A. Feltz, M. Steinbruck and F.W. Breit-Barth, *Z. Anorg. Allg. Chem.*, 1990, **137**, 137.

18- A.B. Sheikh and J.T.S. Irvine, *J. Solid State Chem.*, 1993, **103**, 30.

19- M. Steinbruck and A.Feltz, *Z. Anorg. Allg. Chem.*, 1991, **594**, 157.

20- W.H. Bragg,, *Nature*, London, 1915, **95**, 561.

21- S. Nishikawa, *Proc. Toyko-Math. Phys. Soc.*, 1915, **8**, 199.

22- A.A. Finch, A.B. Sheikh, G. Mather, C. Namgung and J.T.S. Irvine, *Proceedings of the Fifth Int. Symp. on Superconductivity*, Springer Verlag, 1992.

23- D.J. Johnson, *J. Low Temp. Phys.*, 1976, **25**, 145.

24- J.T.S. Irvine, Final report on *'Superconductivity in Reduced Titanate Spinels'*, Grant report ref. G48886, SERC, 1993.

25- D.P. Fagg, S.M. Fray and J.T.S. Irvine, *Solid State Ionics*, 1994, **72**, 235-239.

26- B.C.H. Steele, P.H. Middleton and R.A. Rudkin, *Solid State Ionics*, 1990, **40/41**, 388.

27- D.P. Fagg, *Ph.D. Thesis*, University of Aberdeen, 1996.

28- A. Dicks, *Electrochemistry Newsletter*, Royal Society of Chemistry, 1996, **86**, 24.

29- N.Q. Minh, *J. Am. Ceram. Soc.*, 1993, **16**, 563-588.

30- A. McDougall, Fuel Cells, Maximillian, 1976.

31- J.T.S. Irvine and D.P. Fagg, Conference Abstract, *Fuel Cells and Catalysis Conference*, University College, London, 1996.

32- I.R. Gibson and J.T.S. Irvine, *J. Mat. Chem.*, 1995, **6**, 895-898.

33- R. Maenner, E. Ivers-Tiffee, W. Wersing and W. Kleinlein, *in Proc. 2nd Int. Symp. on Solid Oxide Fuel Cells*, eds. F. Gross, P. Zegers, S.C. Singhal and O. Yamamoto (CEC, Luxembourg, 1991), p. 715

34- M. Miyayama, T. Nishi and H. Yanagida, *J. Mater. Sci.*, 1987, **22**, 2624-2628.

35- T. Takahashi, T. Esaka and H. Iwahara, *J. Appl. Electrochem.*, 1977, **7**, 303-308.

36- A. Hammouche, E.L. Schouler and M. Henault, *Solid State Ionics*, 1988, **28-30**, 1205-1207.

37- J.B. Goodenough, *Phys. Rev.*, 1955, **100**, 564-573.

38- H. Taimatsu, K. Wada and H. Kaneko, *J. Am. Cer. Soc.*, 1992, **75**, 401-405.

39- H.U Anderson in: *Proceedings of Crystalline Ceramics*, eds. H. Palmour III, R.F. Davis and T.M. Hare, Plenum Press, New York, 1978, 469-477.

40- S. Murakami, Y. Miyake, Y. Aliyama, N. Ishida, T. Saito and N. Furukawa in: *Proceedings of the Int. Symp. on Solid Oxide Fuel Cells*, eds. O. Yamamoto, M. Dokiya and H. Tagawa, Science House, Japan , 1990.

41- D.P. Fagg, private communication.

42- M.R. Fry, Martin R. Fry and associates, *Fuel Cells for Clean Power Generation and Transport*, EPSRC and BBSRC Clean Technology Unit, October 1994.

43- S.C. Singhal in*: Proceedings of the 2nd Int. Symp. on Solid Oxide Fuel Cells*, eds. F Grosz, P. Zegers, S.C. Singhal and O. Yamamoto, CEC Publ. EUR 13546 EN, Brussels, Belgium, 1991, 25-33.

44- D.C. Fee, P.E. Blackburn, D.E. Busch, T.D. Claar, D.W. Dees, J. Dusek, T.E. Easler, W.A. Ellington, B.K. Flandermeyer, R.J. Fousek, J.J. Hiesberger, T.E. Kraft, S. Majumdar, C.C. McPheeters, F.C.

Mrazek, J.J Piccaolo, R.B. Poeppel and S.A. Zwick, in: *1986 Fuel Cell Seminar Abstracts*, Courtsey Associates, Washington D.C. 1986, 40-43.

45- S. Sakurada and T. Yoshida in: *Proceedings of the 2nd Int. Symp. on Solid Oxide Fuel Cells*, eds. F. Grosz, P. Zegers, S.C. Singhal and O.Yamamoto, CEC Publ. EUR 13546 EN, Brussels, Belgium, 1991, 64-67.

46- C.C. McPheeters and T.D. Claar in: *1986 Fuel Cell Seminar Abstracts*, Courtesy Assoc., Washington D.C., 1986, 64-67

47- N.Q. Minh, F. Liu, P.Staszak, T. Stillwagon and J.Van Ackeren in: *1988 Fuel Cell Seminar Abstracts*, Courtesy Assoc., Washington D.C., 1988, 105-108.

48- N.Q. Minh and C.R. Horne in: *Proceedings of the 14th Risø Symp. Mat. Sci. On High Temp. Electrochem. Behav. Fast Ion & Mixed Conductors*, eds. F.W. Poulsen, J.J. Bentzen, T. Jacobsen, E. Skou and M.J.L Østergård , Risø National Laboratory, Roskilde, Denmark, 1993, 337-341.

49- J.T.S. Irvine, I.R. Gibson and D.P. Fagg, *Ionics*, 1995, **1**, 279-285.

50- J.E. Bauerle, *J. Phys. Chem. Solids*, 1969, **30**, 2657-2670.

51- J.A. Kilner and B.C.H. Steele in: *Non Stoichiometric Oxides*, ed. O.T. Sørensen , Academic Press, New York, 1981, 233- 269.

52- M. Kleitz, H. Bernard, E. Fernandez and E. Schouler in: *Advances in Ceramics*, Vol. 3, eds. A.H. Heuer and L.W. Hobbs (Amer. Cer. Soc., Columbus, OH, 1981), 310-336.

53- J.F. Baumard and P. Abelard, in: *Advances in Ceramics*, Vol. 12, eds. N. Claussen, M. Ruhle and A.H. Heuer, The Amer. Cer. Soc., Columbus, Ohio, 1984, 555-571.

54- J.A. Kilner and R.J. Brook, *Solid State Ionics*, 1982, **6**, 237-252.

55- N.Q. Minh and T. Takahashi, *Science and Technology of Ceramic Fuel Cells*, Elsevier, Amsterdam, 1995.

56- J.A. Kilner and B.C.H. Steele in: *Non Stoichiometric Oxides*, ed. O. Sørensen, Academic Press, New York, 1981, 233-269.

57- Risø Laboratory, private communication.

58- K.D.M. Harris, private communication.

59- B.A. Wechsler and A. Navrotsky, *J. Solid State Chem.*, 1984, **55**, 165-180.

60- E.N.S. Muccillo and M. Leitz, *J. Eur. Cer. Soc.*, 1996, **16**, 453-465.

61- D. Viechnicki and V.S. Stubican, *J. Am. Cer. Soc.*, 1993, **48**, 293.

62- V.S. Stubican, *Adv. Ceram.*, 1988, **24A**, 71-82.

63- A.V. Shevchenko, L.M. Lopato, I.M. Maister and O.S. Gorbunov, *Russ. J. Inorg. Chem.* (Engl. Transl.), 1988, **25**, 1379-1381.

64- C. Zheng, private communication.

65- L.W. Coughanour, R.S. Roth, S. Marzullo and F.E. Sennett, *J. Res. Nat. Bur. Stands.*, 1955, **52**, 191-199.

Chapter 2

Experimental

2.1 Structure of Chapter

As explained in the previous chapter, the principal aim of this project is to develop a more detailed phase diagram of the $MgO:TiO_2:ZrO_2$ system. The first section of this chapter will explain the experimental techniques that were employed for sample analysis such as X-ray diffraction, thermal analysis and a.c.-impedance spectroscopy. The second section is concerned mainly with the synthetic details of the experiments that were performed during the course of this project.

2.2 Experimental Techniques

2.2.1 X-ray diffraction

X-ray diffraction was carried out using a Stoe STADI P automated diffractometer operating in transmission mode. With the associated software, it is possible to obtain useful information such as lattice parameters, crystallite size and the content of each phase present. Using a germanium monochrometer, Cu $K\alpha_1$ radiation was selected and X-rays of wavelength 1.54056Å were used.

The measurement of diffracted X-rays was made possible by the use of a small linear position sensitive detector (PSD) which had a range of 7° 2θ.

The detector could move through 10 - 140 2θ in small increments - the stepwidth - which could be determined by the user.

Samples were prepared by lightly smearing an acetate foil with vaseline, on to which about 1 mg of powdered sample was applied. The acetate foil was fitted into a circular holder which was placed into the diffractometer. The holder was continuously rotated to minimise preferred orientation.

For lattice parameter determination, x-rays were collected over a 2θ range of 10-70 2θ, typically using a stepwidth of 0.5093 and measuring for 10 seconds per step. Data analysis was performed using the associated Stoe software. The collected raw data was stored in the file RAWDAT. Using the peak searching program PKS and by selecting the average peak width and the significant identity to background ratio, all reflections were determined from the raw data and an output file listing peak positions (2θ and d-spacings), the peak widths (full width and half maximum, FWHM) and relative peak identity (I/Io) were obtained.

Lattice parameters were obtained using the lattice refinement program LATREF. The refinement required the input of symmetry and/or the approximate unit cell. As the lattice parameters were being refined, and as the reflections and symmetry of cubic fluorite peaks were already known[1], it was decided to input the Millar indices for some of the peaks using the peak editing program PEAKED, prior to refinement. From the symmetry chosen by the user, the LATREF program generates all the possible reflections and using the least squares procedure, the lattice parameters were refined. The quality of the refinement could be determined by the error in the lattice parameters and the values of the maximum and average difference in $2\theta_{obs}$ and $2\theta_{calc}$ (2θ).

2.2.2 Thermal Analysis

Differential thermal analysis (DTA) is a technique in which the difference in temperature between a sample and reference material is monitored against time or temperature while the temperature of the sample, in a specified atmosphere is programmed. The DTA curve is generally a plot of the difference in temperature (ΔT) on the horizontal axis against the temperature T (or occasionally the time) on the vertical axis[2]. An endothermic event gives a downwards 'peak' (Figure 2.1).

Differential thermal analysis was carried out using a computer controlled TA SDT simultaneous DTA-TGA apparatus using pre-dried alumina (Al_2O_3) as the reference material. In all instances, thermogravimetry showed no significant change in mass during heating.

The platinium pans were cleaned out thoroughly, dried and pre-weighed. Approximately 30 mg of both sample and reference material were weighed and inserted into separate platinium pans. The furnace was then sealed and an appropriate program was made up on the computer indicating the conditions for the sample being analysed. Figure 2.2 shows a sample program that was used to analyse the $(Mg_2TiO_4)_{0.2}$ $(ZrO_2)_{0.8}$ system from 50-1400°C.

2.2.3 A.c.-impedance spectroscopy

A.c. impedance spectroscopy is a well-defined technique used to investigate and characterise the electrical properties and microstructure of a wide variety of ceramic materials[3]. The technique has been extensively used for studying the ionic conductivity of stabilised zirconia systems such as yttria-stabilised zirconia[4]. In addition to establishing the ionic conductivity values of stabilised zirconia systems, a.c. impedance spectroscopy has been

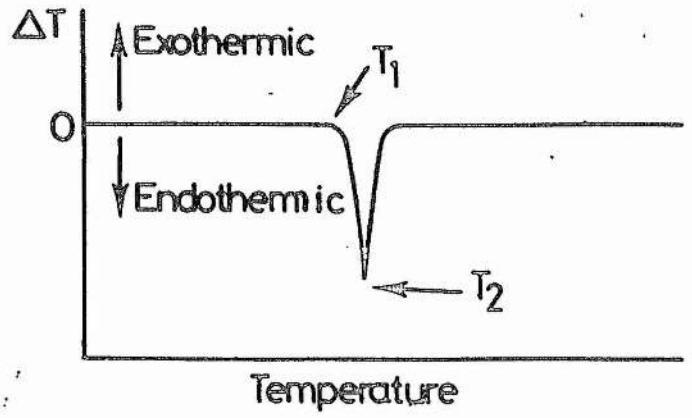

Figure 2.1 A D.T.A. graph showing evidence of an endothermic peak

Segment Description

1. Jump to 50°C
2. Isothermal for 5 minutes
3. Ramp 10°C/minute to 1400°C
4. Isothermal for 10 minutes
5. Ramp 10°C/minute to 200°C
6. Air cool (using O_2 as purge gas)
7. Mark end of cycle 0

Figure 2.2 Sample program for TGA-DTA instrument. This program was used to evaluate the $(ZrO_2)_{0.8}$ $(Mg_2TiO_4)_{0.2}$ system between 50 and 1400°C.

extensively used to investigate the effects of corrosion[3], segregation of impurities[5], defect interactions and ageing phenomen[6].

The a.c. measurement

The electrical properties of a variety of materials were initially studied by the d.c. resistance measurement. However, the applications of this technique are limited as it measures only the total resistance of the cell, which includes contributions from the material and the electrodes. A.c. impedance spectroscopy has the advantage that individual components of the material can be separated e.g. bulk grain boundary, sample/electrode interface, allowing detailed characterisation to be made. A comprehensive study of a.c. impedance spectroscopy and its applications has been made by MacDonald[7].

The a.c. impedance technique involves the application of an a.c. voltage (V) of varying frequency across the sample:

$$V = V_o \sin \omega t \qquad (2.1)$$

The resultant current (denoted by I) leads the voltage by φ, the phase shift of the transfer function; therefore:

$$I = I_o \sin (\omega t + \varphi) \qquad (2.2)$$

The transfer function can be defined as:

$$H(\omega) = |H(\omega)| e^{i\varphi}$$

where $|H(\omega)| = V_o/I_o$ and $|H|$ is the modulus of the transfer function.

The impedance is given by:

$$Z = \frac{V}{I} \qquad (2.3)$$

Impedance is a vector quantity and can be defined using the complex numbers terminology:

$$Z^* = Z' - j\,Z'' \qquad (2.4)$$

complex real imaginary

The magnitude and direction of the complex impedance Z^* can be expressed as real (Z') and imaginary (Z'') components. The complex impedance can be plotted by cartesian (Z' vs. Z'') or polar co-ordinates ($|Z|$ vs. φ), Figure 2.3.

Thus:

$$Z' = |Z| \cos \varphi \qquad (2.5)$$

$$Z'' = |Z| \sin \varphi \qquad (2.6)$$

By measuring the amplitude and phase shift (φ) of the current for any frequency (ω), with a fixed applied voltage (V), the impedance is calculated (equation 2.3) and Z' and Z'' can be determined (equations 2.5 and 2.6 respectively). By varying the frequency from 100-10^7 Hz, a complex impedance plot such as Figure 2.4can be obtained.

Equivalent circuits

Ceramic materials can contain many components e.g. bulk ferroelectric, grain boundary, which can be identified by a.c. impedance spectroscopy; each component can be considered as consisting of a combination of both resistive and capacitive elements. This combination of resistive and capacitive elements is called an equivalent circuit, and, depending on the properties of the material, different combinations will apply.

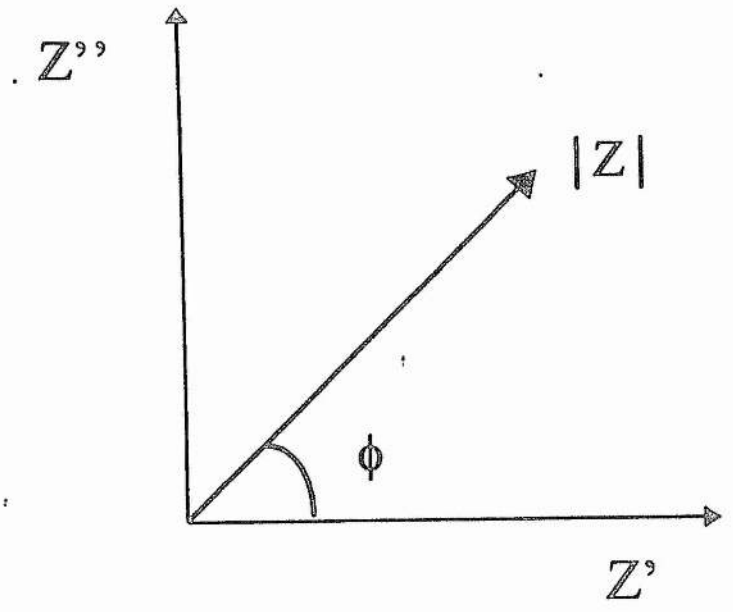

Figure 2.3 The complex impedance plane which can be plotted as cartesian (Z''vs. Z') or in polar form (|Z| vs.φ).

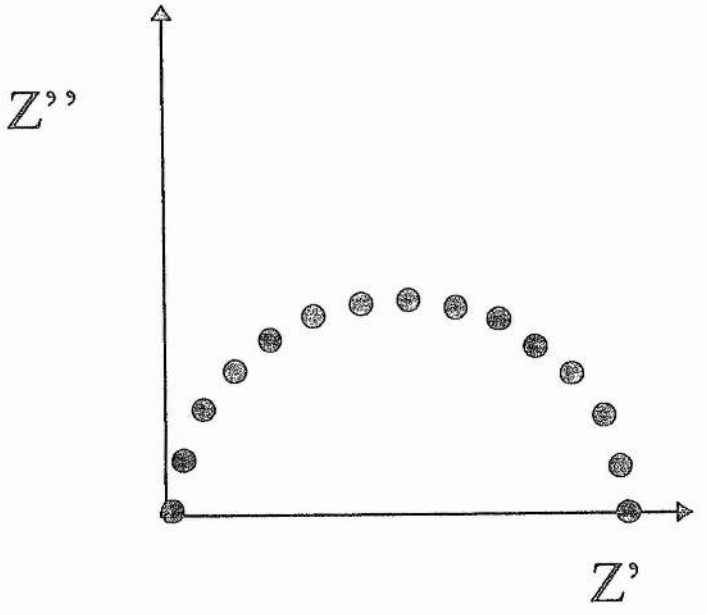

Figure 2.4 A typical complex impedance plot, obtained over a wide frequency range.

The simplest equivalent circuit can be obtained for either an ideal individual resistor or an ideal individual capacitor. For an ideal resistor, current and voltage are in phase and from equations 2.1 and 2.2:

$$R = \frac{V_o}{I_o}$$

where R is the resistance (Ω); therefore, from equation 2.3:

$$Z = R$$

So, from a phase shift $\varphi = 0$, Figure 2.5(a) is obtained. An alternative formalism is the complex admittance, Y'', which is equal to the inverse of the complex impedance $(Z^*)^{-1}$, so for an ideal resistor:

$$Y^* = R^{-1} \qquad (2.7)$$

For an ideal capacitor, the capacitance (F) is given by:

$$C = \frac{q}{V}$$

where q is the charge stored (C) and V is the voltage across the capacitor.

$$I = \frac{dq}{dt} = C\left(\frac{dV}{dt}\right)$$

For a capacitor, the current leads the voltage by 90° - out of phase - and from equation 2.1:

$$I = \omega c v_o (\sin \omega t + \pi/2) \qquad \text{since } \varphi = 90°$$

From equation 2.2:

$$I = \omega c v_o$$

An ideal capacitor allows the flow of an a.c. current but blocks a d.c. current (i.e. Z' = 0); from equations 2.3 and 2.4:

$$Z^* = \frac{1}{j\omega c}$$

and

$$Y^* = j\omega c \qquad (2.8)$$

producing the complex plane plot in Figure 23 (b).

Most components e.g. bulk can be modelled in terms of a resistive element in parallel. The complex impedance of the parallel RC element is defined as:

$$\frac{1}{Z^*T} = \frac{1}{Z^*_1} + \frac{1}{Z^*_2}$$

or:

$$Y^*_T = Y^*_1 + Y^*_2$$

and from equations 2.7 and 2.8,

$$Y^*T = \frac{1}{R} + j\omega c$$

i.e. $Y' = \frac{1}{R}$ and $Y'' = \omega c$

The total complex impedance is given by:

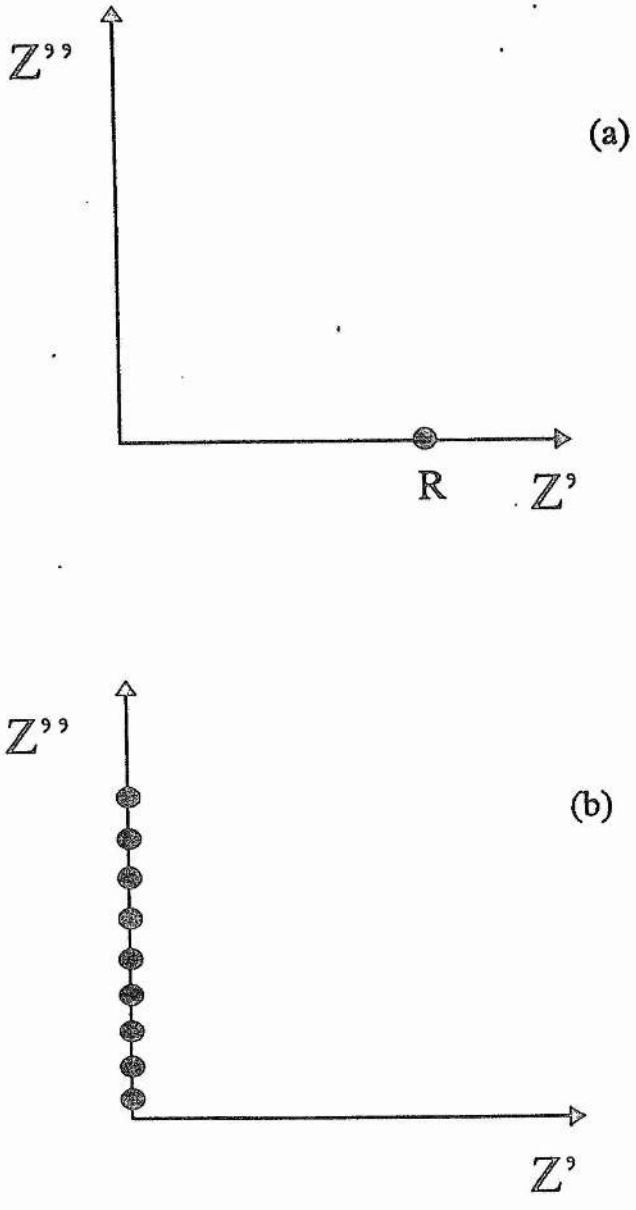

Figure 2.5 Complex impedance plane plots for (a) a resistor behaving ideally and (b) an ideal capacitor

$$Z^*_T = (Y^*_T)^{-1} = \left(\frac{1}{R} + j\omega c\right)^{-1}$$

$$= \frac{R}{1 + j\omega RC} \cdot \frac{(1 - j\omega RC)}{(1 - j\omega RC)}$$

$$= \frac{R(1 - j\omega RC)}{1 + (\omega RC)^2}$$

$$= \frac{R}{1 + (\omega RC)^2} - j\,\frac{R(\omega RC)}{1 + (\omega RC)^2}$$

$$Z' \quad - \quad j\,Z''$$

i.e. $$Z' = \frac{R}{1 + (\omega RC)^2} \text{ and } Z'' = \frac{R(\omega RC)}{1 + (\omega RC)^2} \qquad (2.9)$$

By varying the frequency from 0 to 10^6-10^8 Hz, a complex plane plot, illustrated in Figure 22, is obtained. When ωRC = 1, a maximum Z'' is obtained and at this point $Z' = Z'' = \frac{R}{2}$.

From this simple derivation, the resistance and capacitance of an unknown component can be determined by obtaining the real and imaginary impedance over a wide range of frequencies. From Figure 2.4 the resistance equals the real impedance when the frequency equals zero i.e. at the intercept on the x-axis. The capacitance is calculated from the equation:

$$\omega RC = 1 \qquad (2.10)$$

using the frequency (ω) when Z'' is at a maximum.

Real ceramic materials can consist of many like parallel RC elements, connected in series. The equivalent circuit, for example, yttria-stabilised zirconia materials consists of three parallel RC elements and a diffusion element connected in series, producing a complex plane plot of three semi-

circles and a low frequency inclined spike respectively (Figure 2.6). The low frequency spike, or Warburg spike, is due oxygen diffusion at the electrode surface. The first, low frequency semi-circle is also associated with the electrode, and is due to the charge transfer reaction $2O^{-} <\!\!\longrightarrow O_2 + 2e^{-}$.

The two remaining semi-circles are due to grain boundary (low frequency) and bulk (high frequency) components are are associated entirely with the yttria-stablised zirconia ceramic. From equations 2.9 and 2.11, the real and imaginary contributions from each RC element are simply summed:

$$Z = Z_1 + Z_2 \qquad (2.11)$$

So: $$Z' = R_1\left[\frac{1}{1+(\omega R_1 C_1)^2}\right] + R_2\left[\frac{1}{1+(\omega R_2 C_2)^2}\right]$$

$$Z'' = R_1\left[\frac{\omega R_1 C_1}{1+(\omega R_1 C_1)^2}\right] + R_2\left[\frac{\omega R_2 C_2}{1+(\omega R_2 C_2)^2}\right]$$

In addition to a complex plane plot, a plot of the imaginary impedance (Z'') versus log(frequency) is extremely useful. For ceramics like yttria-stabilised zirconia, two extreme cases may be observed, Figure 2.7 (a) and 2.7 (b). Case (a) is observed for a ceramic material with a high grain boundary resistance, probably due to poor sintering. By contrast, case (b) is observed with a small grain boundary resistance, suggesting a high degree of sintering.

The combination of RC elements in series is a simplified model and it has been shown that more complicated circuits can describe experimental data more accurately[7,8]. The simplified model describes exact semi-circles for each RC element; however, semicircles can often appear compressed, with their centres appearing below the real Z'-axis. This non-ideal behaviour might be due to a distribution in relaxtion times within each component and models using a constant phase element (CPE) have been used to describe such

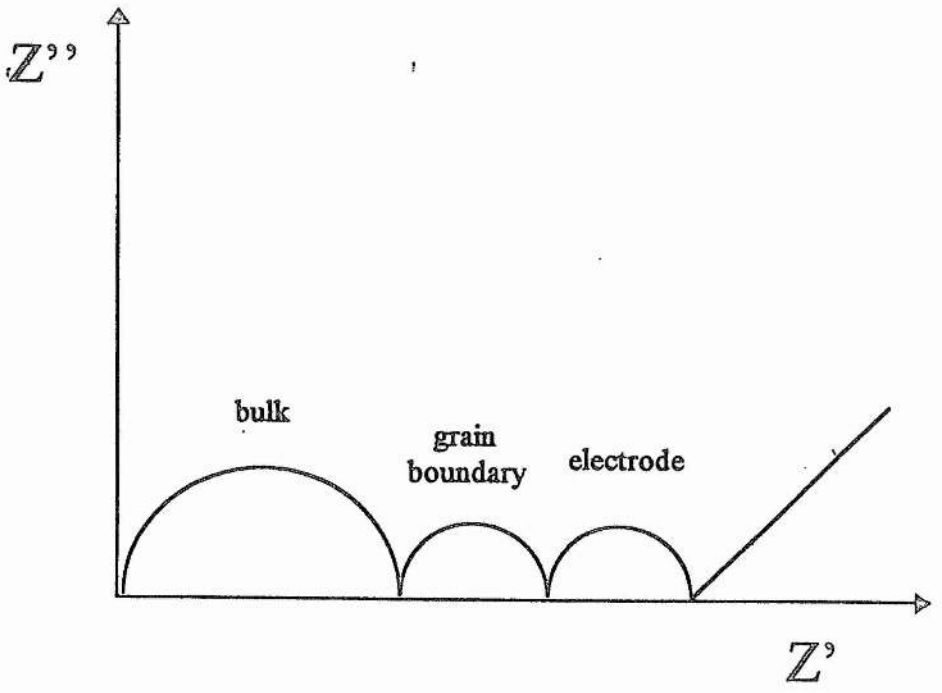

Figure 2.6 Typical complex impedance plane plot for 8 mol% yttria stabilised zirconia [Adapted from Gibson[12]]

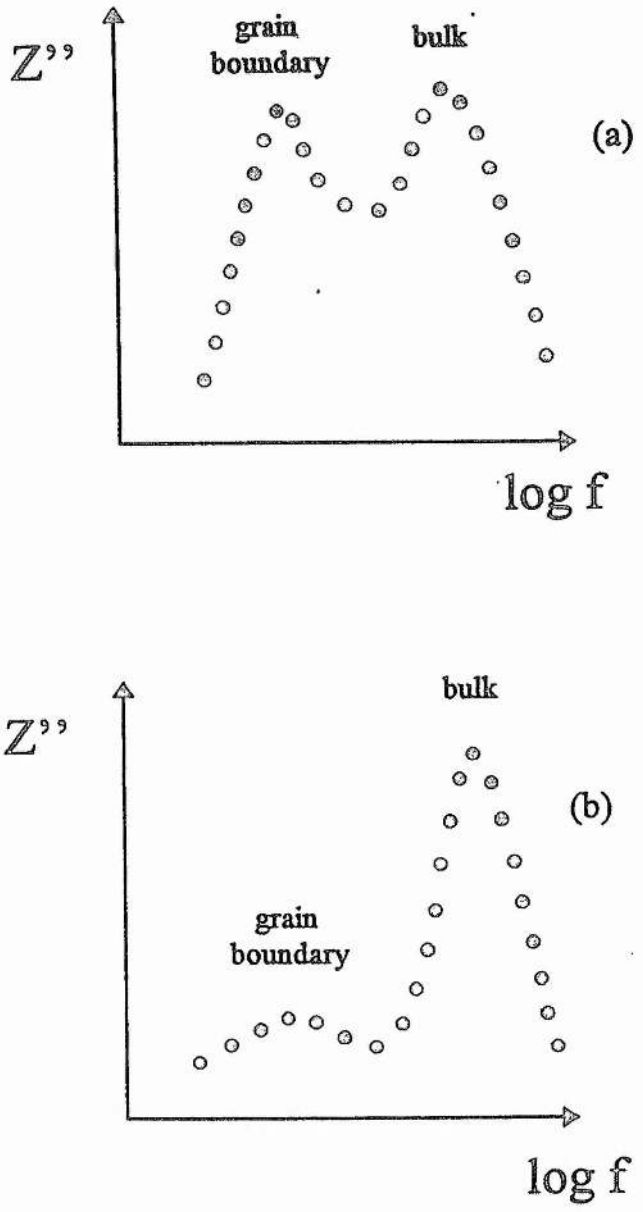

Figure 2.7 Imaginary impedance versus log (frequency) plots for (a) a poorly sintered porous, and (b) a well sintered dense YSZ ceramic [Adapted from Gibson[12]]

behaviour. Although computer software is now available to incorporate CPE's into the equivalent circuit, the simplified model has been used in this project.

Activation energies

Activation energy in solids can be defined as the *minimum* energy required for ions to be mobile in a way that they move from one site to another. This leads to ionic conductivity. The general requirements for ionic conduction to occur are:

(i) a number of the ions of one species should be mobile;
(ii) there should be a number of empty sites available for the mobile ions to jump into.

Ionic conductivity can be characterised by means of the Arrhenius equation:

$$\sigma = A/T \exp^{(-Ea/kT)}$$

The activation energy of conduction for any component can be obtained by measuring the change in conductivity with temperature. The slope of the Arrenhenius plot ($\log\sigma T$ vs. 1000/T) allows the activation energy to be calculated.

$$E_A = \frac{2.303 \times slope \times 1.38 \times 10^{-23}}{1.6 \times 10^{-19}} \qquad (eV)$$

Sample preparation

Platinium electrodes were attached to both faces of a disc using platinium paste (Engelhard). The platinium paste was initially dried at 100°C

for 10 minutes. The disc is then sintered in air at 850°C for 30 minutes. This procedure was repeated for the other face of the disc.

Experimental procedure

The sintered sample was connected to a platinium wire jig *via* the applied platinium electrodes. The jig was a 30cm rod of alumina with four narrow longitudinal holes through it; two platinium wires and a chromel/alumel thermocouple was threaded through these holes. The sample end of the jig was placed into a Gallenkamp horizontal tube furnace connected to a Eurotherm temperature controller. The temperature was accurately measured (± 1°C) using the chromel/alumel thermocouple, which was attached to a digital multimeter. Two terminal A.C. measurements wre performed using a Solartron 1260 Impedance Analyser, which was linked to the ZView computer program. An a.c. voltage of 100mV was applied, over a frequency range of 10MHz to 100mHZ, with ten measurements for every decade in frequency. An integration time of 1 second per measurement was used with a delay time of 0.2 seconds between each measurement. The measurements were made in air, over a temperature range of 200°C to 1000°C. The data collected were corrected for sample geometry and the complex impedance plots allowed the conductivity (Scm^{-1}) to be determined.

Jig correction [10]

To correct for the resistance of the platinium wires, the resistance of the jig was connected to make a short circuit which was measured between 300-1000°C. The jig resistance was found to increase in slight increments with temperature and an equation was derived which was applied to each impedance value obtained. The resistance of the jig was significant with respect to sample resistance at temperatures in excess of 650°C.

2.3 Synthetic experimental procedures

2.3.1 Synthesis and characterization of the Mg_2TiO_4 spinel phase

Previous work on the synthesis of the magnesium titanate spinel had centred upon using stoichiometric amounts of MgO, TiO_2 (dried at 800°C) and Ti metal powder (stored under vacuum and heated at 1350°C for 24 hours). It was found that due to the rapid uptake of moisture/CO_2 by magnesium oxide, that unsatisfactory results were obtained.

This consequently led Fagg et al[11] to develop a novel synthetic route to prepare the magnesium titanate by means of a Mg_2TiO_4 precursor.

Synthesis of the precursor

Stoichiometric amounts of TiO_2 (rutile polymorph; Tioxide) and magnesium carbonate pentahydrate ($MgCO_3.Mg(OH_2).5H_20$) (Aldrich) were ground intimately under acetone, using an agate pestle and mortar. The powder is dried in air and transferred to an alumina crucible and fired at 800°C (to allow decarbonation to occur). The remaining residue, was then transferred to a platinium crucible and fired at 1450°C. Phase purity was confirmed by STADI P Stoe X-ray analysis (Figure 2.8).

N.B. The peak at ~ 21.5 2θ should be **ignored** as it is a vaseline peak.

2.3.2 Synthesis of $(ZrO_2)_x$ $(Mg_2TiO_4)_y$ samples

Stoichiometric amounts of zirconia (Tioxide; vacuum dried) and magnesium titanate (as prepared in previous section) were ground initially with a Fritsch planetary micromill for 1 hour. The sample was then transferred to an alumina/platinium crucible and fired at 1500°C for 24 hours. After 24

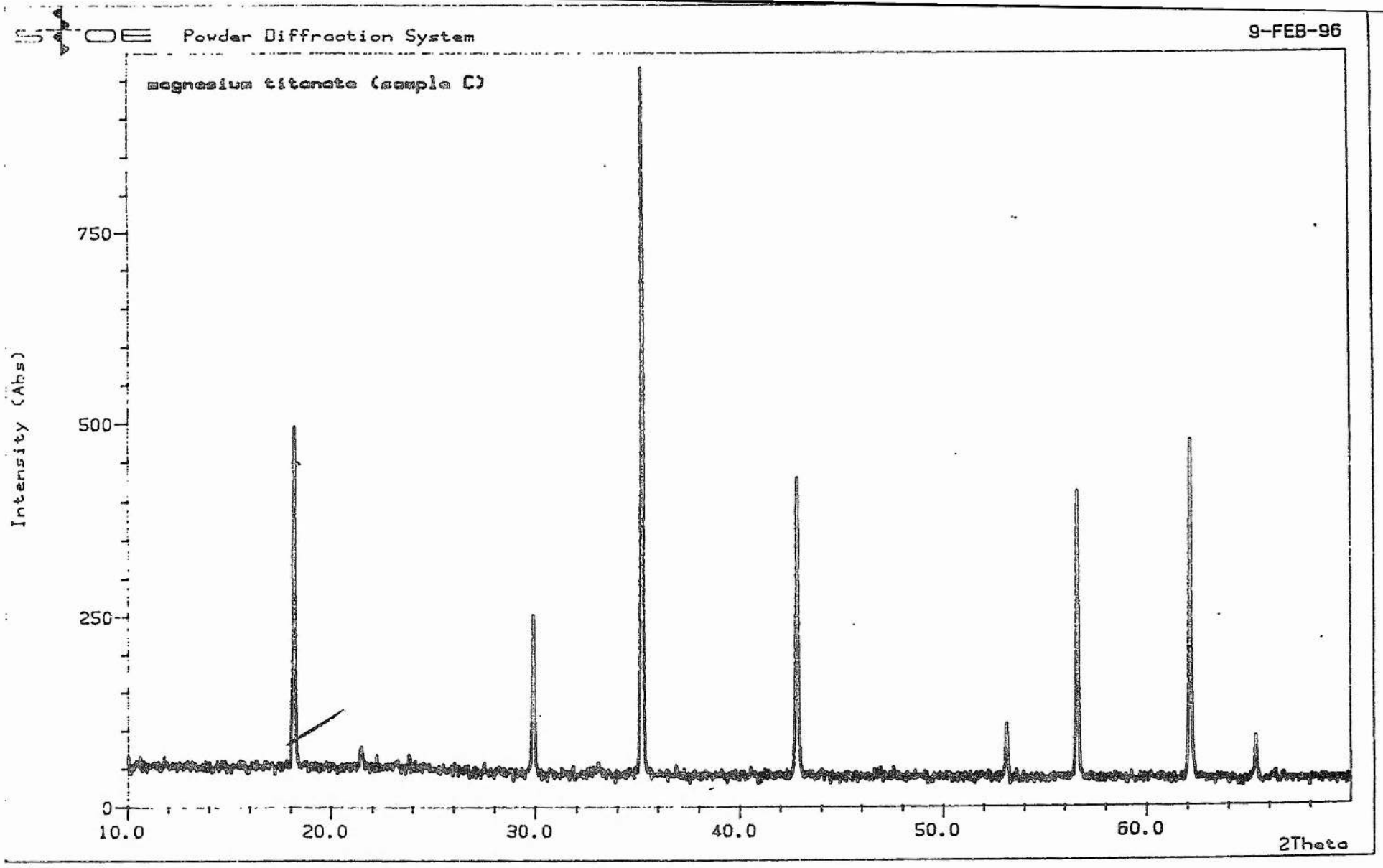

Figure 2.8 : The Mg_2TiO_4 x-ray pattern

hours, the sample was taken out of the furnace and ground under acetone using a pestle and mortar for 30 minutes. The reground sample was transferred to an alumina/platinium crucible and left for 48 hours at 1500°C.

Table 2.1 shows the samples that were prepared within the $(ZrO_2)_x$ $(Mg_2TiO_4)_y$ join alongside with the appropriate amounts of starting materials.

2.3.3 Synthesis of $(ZrO_2)_x$ $(MgO)_y$ $(TiO_2)_z$ samples by the carbonate technique

Due to the poor reaction kinetics, even at 1500°C which was required for the synthesis of magnesium titanate, it was decided to develop an alternative synthesis for the preparation of samples that were outwith the Mg_2TiO_4-ZrO_2 join.

Experimental Procedure

Stoichiometric quantities of zirconia (Tioxide; vacuum dried), titanium dioxide (Tioxide; rutile polymorph; dried at 800°C) and magnesium carbonate pentahydrate (Aldrich) were ground intimately using an agate prestle and mortar. The residue was transferred to an alumina crucible and inserted into a Carbolite muffle furnace at 800°C and left for 18 hours. The sample was taken out of the furnace after 18 hours and left to cool before transferring the sample to a Fritsch planetary micromill where the samples were ground for approximately 1 hour. The ground sample was then transferred to an alumina/platinium crucible and inserted into a Carbolite high temperature furnace where it was left to react for approximately 72 hours.

Table 2.2 shows the samples that were prepared by the above experimental procedure alongside with the appropriate quantities of starting materials.

Sample Number	Sample Composition		
	ZrO_2	MgO	TiO_2
3	20	40	40
7	40	40.2	19.8
8	40	30	30
9	50	33.5	16.5
14	54	30.82	15.18
15	55	30.15	14.85
16	56	29.48	14.52
18	57.1	28.74	14.16
26	65	23.33	11.67
27	67	22	11
32	70	20.1	9.9
53	83	11.33	5.67
56	87	8.67	4.33

Table 2.1 : Listing of samples prepared by the precursor technique

Sample Number	Sample Composition		
	ZrO_2	MgO	TiO_2
1	20	70.4	9.6
2	20	53.6	26.4
4	20	26.4	53.6
5	20	12	68
6	30	4.9	65.1
10	50	25	25
11	50	16.5	33.5
12	50	---	50
13	40	3.6	56.4
17	57.1	28.74	14.16
19	59	27.47	13.53
20	60	26.8	13.2
21	59	26.24	14.76
22	62	22.8	15.2
23	64	20.16	15.84
24	67	16.5	16.5
25	62	25.46	12.54
28	60	20	20
29	60	13.2	26.8
30	70	26.4	3.6
31	67	20.79	12.21
33	70	15	15
34	70	16.8	13.2
35	70	9.9	20.1
36	76	0.48	23.52
37	75	25	---
38	73	24.03	2.97
39	74	21.32	4.68
40	75	16.675	8.25
41	75	15.75	9.25
42	75	14.75	10.25
43	75	12.5	12.5
44	75	10	15
45	75	8.25	16.75
46	79	14	7
47	80	10	10
48	80	6.66	13.34
49	80	4.6	15.4
50	85	15	---
51	86	11.9	2.1
52	81	12.7	6.3
54	84	10.67	5.33
55	86	9.33	4.67
57	92	5.33	2.67
58	84	8	8
59	87	6.5	6.5
60	83	6.8	10.2
61	86	4.67	9.33
62	90	1.5	8.5

Table 2.2: Listing of samples prepared by the carbonate method

Figure 2.9 shows the location on the ternary phase diagram of all the samples that were prepared by the two different experimental procedures (Section 2.3.2 and this section).

2.3.4 Quenching techniques

It was decided to quench some samples to see if any significant changes happened to the sample structure as the majority of samples were left to cool in alumina crucibles after removal from the furnace on completion of reaction. It is known that alumina cools much more slowly than platinium which led us to believe that upon slow cooling of a sample, some of the sample might undergo a tranformation back to its low temperature structure. By using small masses in platinium foil, the rate of cooling is much faster, meaning that any structure transformations that occur during cooling are minimal.

Quenching experimental procedure

Platinium envelopes of *ca.* 2cm square were made and approximately 0.1g of sample was inserted into the envelope. The envelopes were placed into a Carbolite high temperature furnace for 30 minutes at 1500°C. After 30 minutes, the envelopes were removed as quickly as possible from the furnace onto a retractory brick which was turned over to catch the platinium foil. Table 2.7 gives a listing of the samples that were quenched.

2.4 References

1- JCPDS file number 27-997.

2- Haines, P.J., *Thermal Methods of Analysis*, Blackie Pubs., 1995.

3- N. J. Evans, *Electrochemistry Newsletter*, Royal Society of Chemistry, 1996, **86**, 11.

4- A. Feighery, private communication.

Sample	Composition		
	ZrO_2	MgO	TiO_2
14	54	30.82	15.18
17	57.1	28.74	14.16
20	60	26.8	13.2
24	67	16.5	16.5
37	75	25	---
52	81	12.7	6.3

Table 2.3 Listing of samples that were quenched

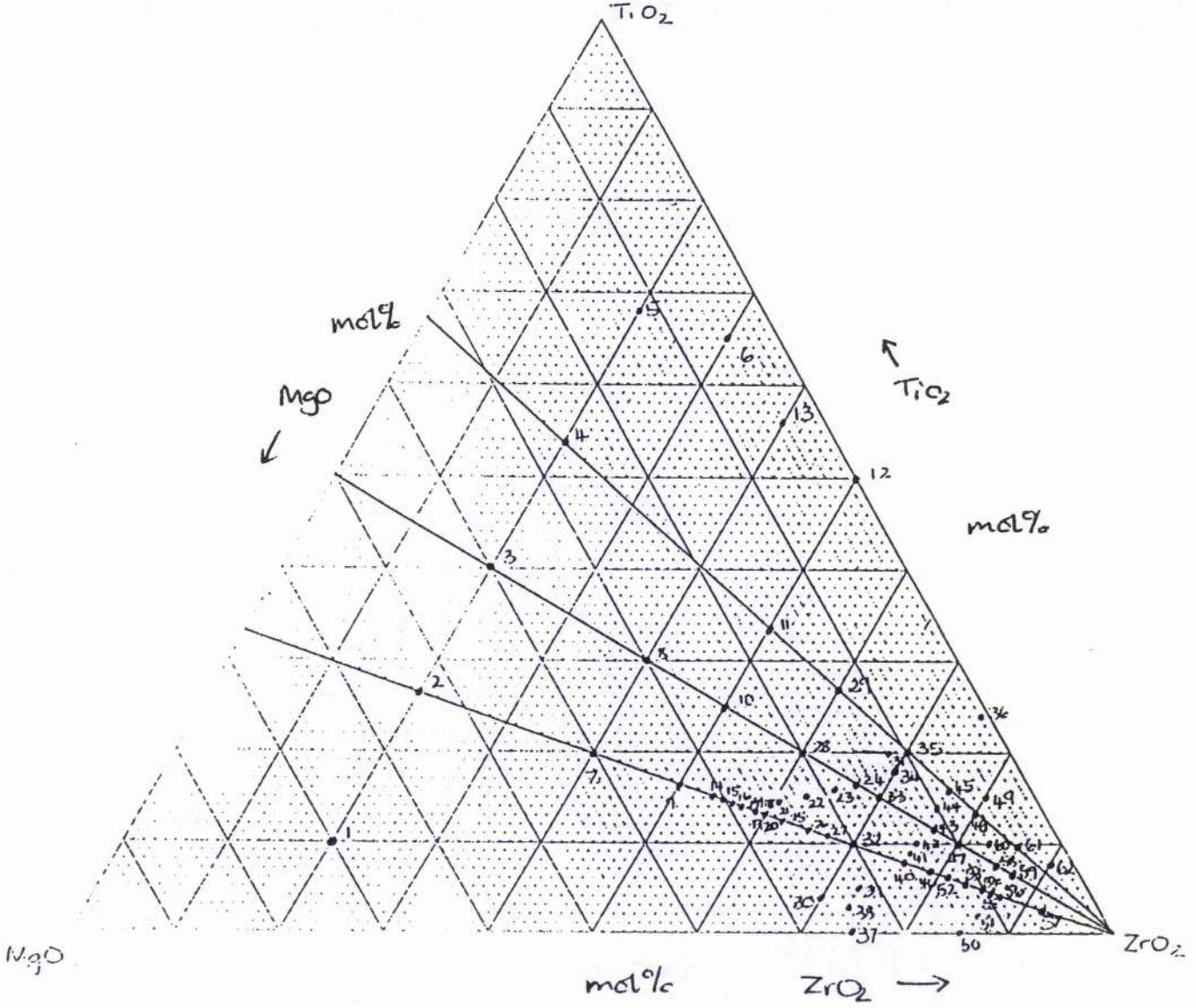

Figure 2.9: Phase diagram showing location of samples selected

5- S.P.S. Badwar, *Solid State Ionics*, 1995, **76**, 67-80.

6- F.T. Ciacchi, K.M. Crane and S.P.S. Badwal, *Solid State Ionics*, 1994, **73**, 49-61.

7- J. Ross Macdonald, *Impedance Spectroscopy*, John Wiley and Sons, 1989.

8- P.G. Bruce, A.R. West and D.P. Almond, *Solid State Ionics*, 1982, 7, 57-60

9- A.K. Jonscher, *J. Mat. Sci.*, 1978, 5, 553-562.

10- I.R. Gibson, *Ph.D. thesis*, University of Aberdeen, 1995.

11- D.P. Fagg, S.M. Fray and J.T.S. Irvine, *Solid State Ionics*, 1994, 72, 235-239.

Chapter 3

Results and Discussion

3.1 X-ray results

When a X-ray pattern was obtained of a sample like that shown in Figure 3.1, it was necessary to identify the phases that were present. By using the peak listing program, PKS, a printout was obtained of all the significant peaks present in the X-ray pattern. It is possible to identify the peaks present by using a X-ray pattern database such as the one provided by the Joint Committee on Powder Diffraction Standards (JCPDS). By selecting the X-ray reference pattern data in the JCPDS database of both the starting materials (MgO, TiO_2 and monoclinic ZrO_2) and the possible resulting structures (such as ilmenite, distorted pseudobrookite, cubic-fluorite, tetragonal zirconia and orthorhombic), it was possible to identify the phases that were present. For example, consider Figure 3.1, by checking the JCPDS files for magnesium oxide[1] and cubic-fluorite phase[2], it was possible to assign all the peaks present as either magnesium oxide or cubic-fluorite phase. As a safeguard, the PKS listing was used to double check that the peaks present had all been identified.

3.2 The $MgO:TiO_2:ZrO_2$ phase diagram

A preliminary phase diagram based upon the reference binary systems $MgO\text{-}TiO_2$ [3], $MgO\text{-}ZrO_2$ [4] and $TiO_2\text{-}ZrO_2$ [5] is given in Figure 3.2. From the previously reported ternary phase diagram[6] it appeared that a large single cubic-fluorite phase region should exist in the zirconia-rich area of the phase diagram. Initial investigations were made on the M_2T:Z(c) phase join with

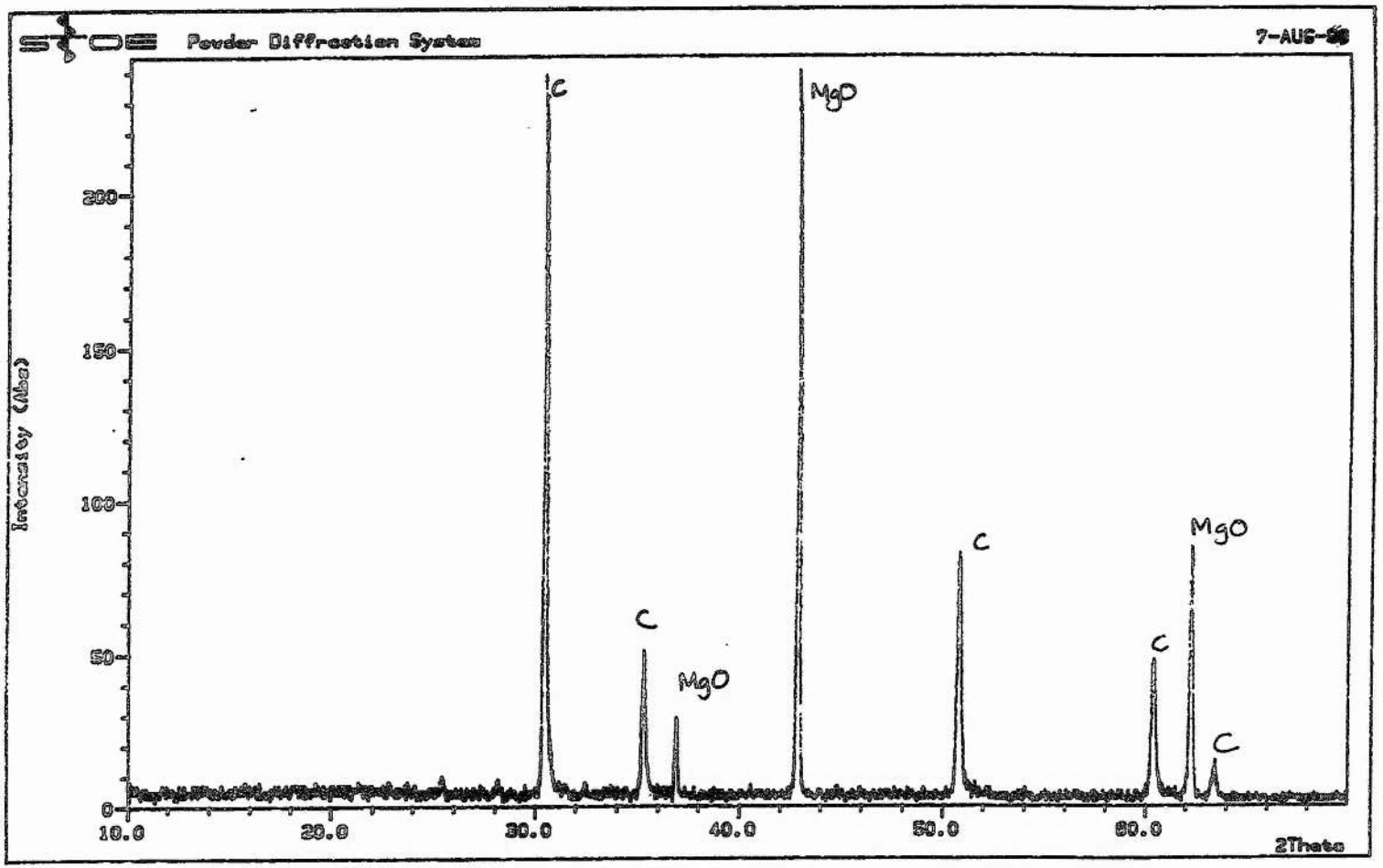

Figure 3.1: X-ray pattern of $(ZrO_2)_{0.75}$ $(MgO)_{0.25}$ (Sample 37)

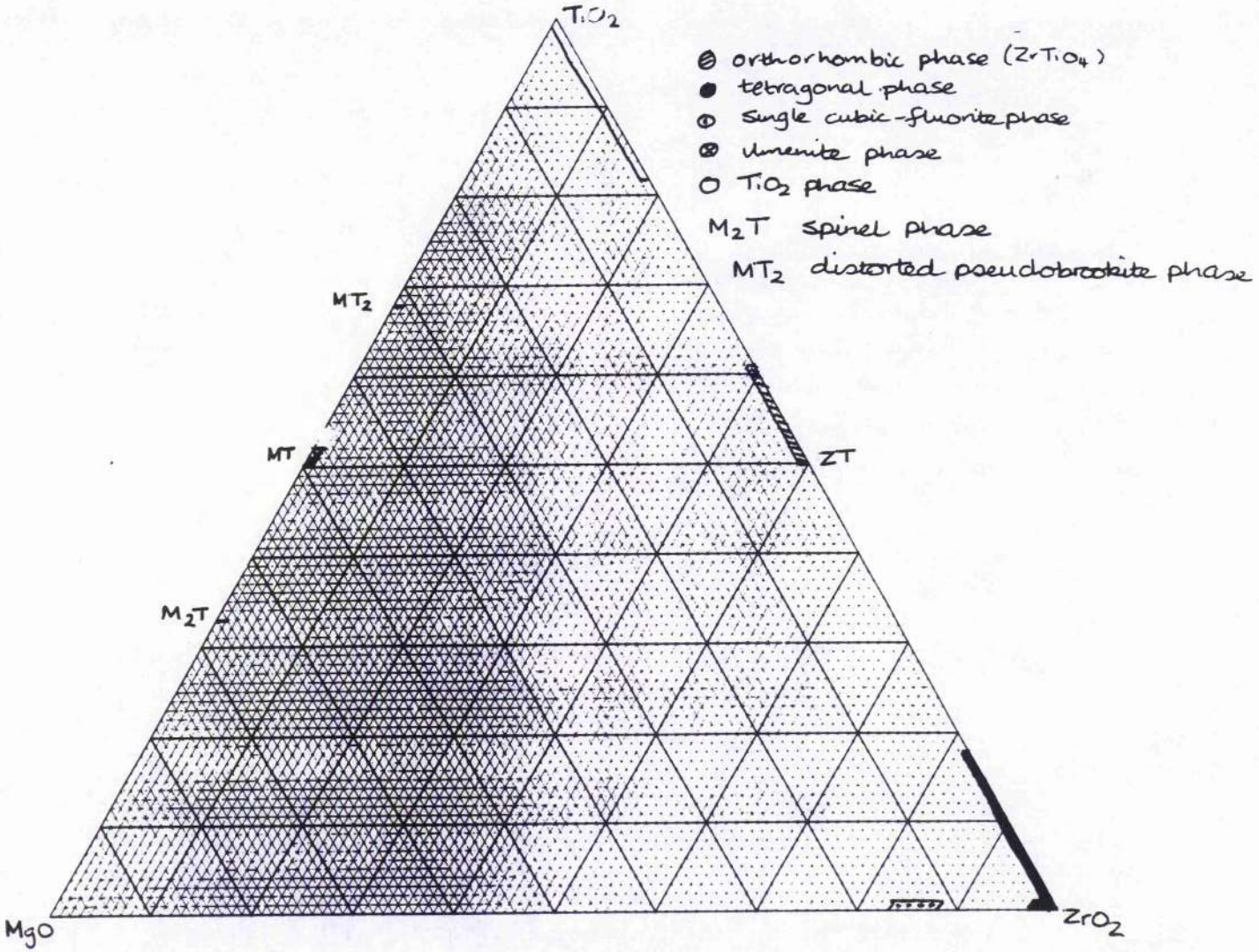

Figure 3.2: Prelimary phase diagram based upon the single phases in the reference binary systems MgO-TiO_2, MgO-TiO_2 and TiO_2- ZrO_2 at 1500°C

particular emphasis on the zirconia-rich region as it was thought that a single phase region containing the cubic-fluorite phase.

Table 3.1 shows the results that were obtained by the experimental procedures described in Chapter 2. The results were plotted onto a phase diagram using colour coding as shown in Figure 3.3. The X-ray patterns of some selected points in the phase diagram are shown in Appendix 2. It can be clearly seen from Table 3.1 that there are eleven separate and distinct phases within the $MgO:TiO_2:ZrO_2$ phase diagram from the samples that were analysed.

By considering the phase rule for this ternary system, one would expect, at most four phases to co-exist at equilibrium. However, in a solid system where the solids have high melting temperatures, the vapour pressure of both the solid phases and the liquid phase, if any, is negligible in comparison with atmospheric pressure. The vapour phase is, therefore non-existent and need not be considered. This means, that for the $MgO:TiO_2:ZrO_2$ system, there should be, at most, three phases present at equilibrium which has been proved experimentally (Table 3.1).

The cubic-fluorite, MgO and spinel triphasic region

As it can be seen from Table 3.1, one of the $(ZrO_2)_{0.8}$ $(Mg_2TiO_4)_{0.2}$ samples (Sample 18) which was prepared by the precursor method as described in Chapter 2.3.2 was single phase (Figure 3.4) but later attempts to reproduce similar results have proved to be rather fortuitous. This may be due to the fact that the quantity of zirconia used in the sample was incorrect.

In the first half of the line joining Z(c) with spinel where samples 1, 2, 7, 9, 14 and 15 are involved, there are three separate and distinct phases present: magnesium oxide, spinel and cubic-fluorite zirconia (Figure 3.5). The presence of spinel is likely to be due to an excess of dopant present as only a

Table 3.1: Listing of experimental results obtained after reaction at 1500°C

Sample Number	Amount of each material present			Phases present
	ZrO_2	MgO	TiO_2	
1	20	70.4	9.6	C + MgO + S
2	20	53.6	26.4	C + MgO + S
3	20	40	40	C + I + S
4	20	26.4	53.6	C + P
5	20	12	68	P + O + TiO2
6	30	4.9	65.1	O + TiO2
7	40	40.2	19.8	C + MgO + S
8	40	30	30	C + I + S
9	50	33.5	16.5	C + MgO + S
10	50	25	25	C + I + S (t)
11	50	16.5	33.5	C + P
12	50	----	50	O
13	40	3.6	56.4	O
14	54	30.82	15.18	C + MgO + S
15	55	30.15	14.85	C + MgO + S
16	56	29.48	14.52	C + MgO + S
17	57.1	28.74	14.16	C + MgO + S
18	57.1	28.74	14.16	C
19	59	27.47	13.53	C + MgO + S
20	60	22.8	15.2	C + MgO + S
21	59	26.24	14.76	C + MgO + S
22	62	22.8	15.2	C + MgO + (S)
23	64	20.16	15.84	C + MgO
24	67	16.5	16.5	C + MgO + S
25	62	25.46	12.54	C + MgO + S
26	65	23.33	11.67	C + MgO + S
27	67	22	11	C + MgO + S
28	60	20	20	C + MgO + S
29	60	13.2	26.8	C + P
30	70	26.4	3.6	C + MgO
31	67	30.79	12.21	C + P (t)
32	70	20.1	9.9	C + MgO + S (t)
33	70	15	15	C + MgO + S (t)
34	70	16.8	13.2	C + P (t)
35	70	9.9	20.1	C + P (t)
36	76	0.48	23.52	M
37	75	25	---	C + MgO
38	73	24.03	2.97	C + MgO
39	74	21.32	4.68	C + MgO
40	75	16.675	8.25	C + M
41	75	15.75	9.25	C + M
42	75	14.75	10.25	C + M
43	75	12.5	12.5	C + M (t)
44	75	10	15	C
45	75	8.25	16.75	C + M (t)
46	79	14	7	C + M
47	80	10	10	C
48	80	6.66	13.34	C + M
49	80	4.6	15.4	M
50	85	15	---	C
51	86	11.9	2.1	C
52	81	12.7	6.3	C + M
53	83	11.33	5.67	C + M
54	84	10.67	5.33	C + M (t)
55	86	9.33	4.67	C

Sample Number	Amount of each material present			Phases present
	ZrO_2	MgO	TiO_2	
56	87	8.67	4.33	C + M (t)
57	92	5.33	2.67	C + M
58	84	8	8	C
59	87	6.5	6.5	C + M
60	83	6.8	10.2	C + M
61	86	4.67	9.33	M
62	90	1.5	8.5	M

Key

C - Cubic-fluorite phase
MgO - Magnesium oxide
TiO_2 - Titanium dioxide (rutile polymorph)
M - Monoclinic phase
P - Distorted pseudobrookite phase
I - Ilmenite phase
O - Orthorhombic phase
S - Spinel phase
(t) - trace amount of indicated phase

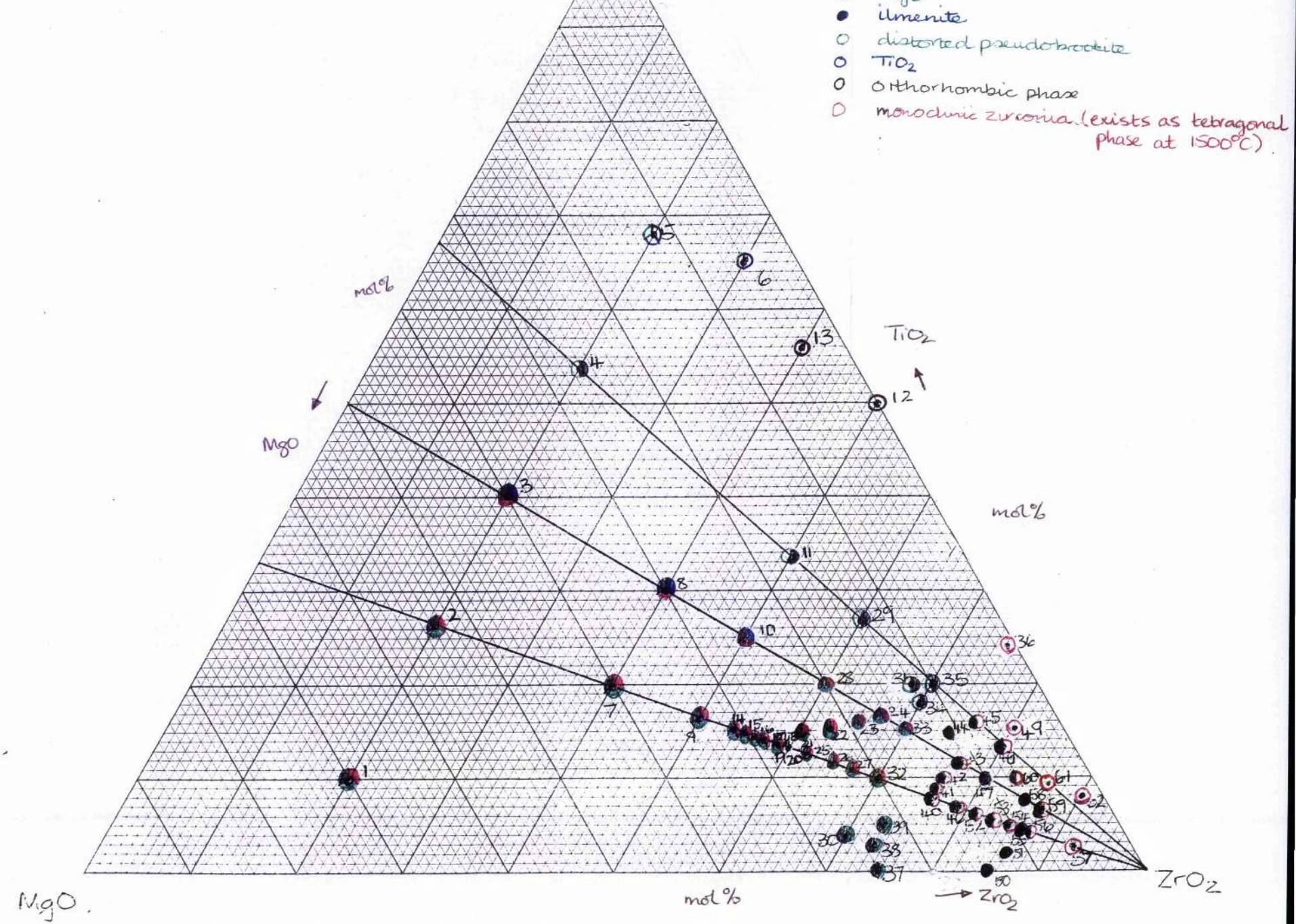

Figure 3.3: Phase diagram with sample colour coding to indicate phases present at 1500°C.

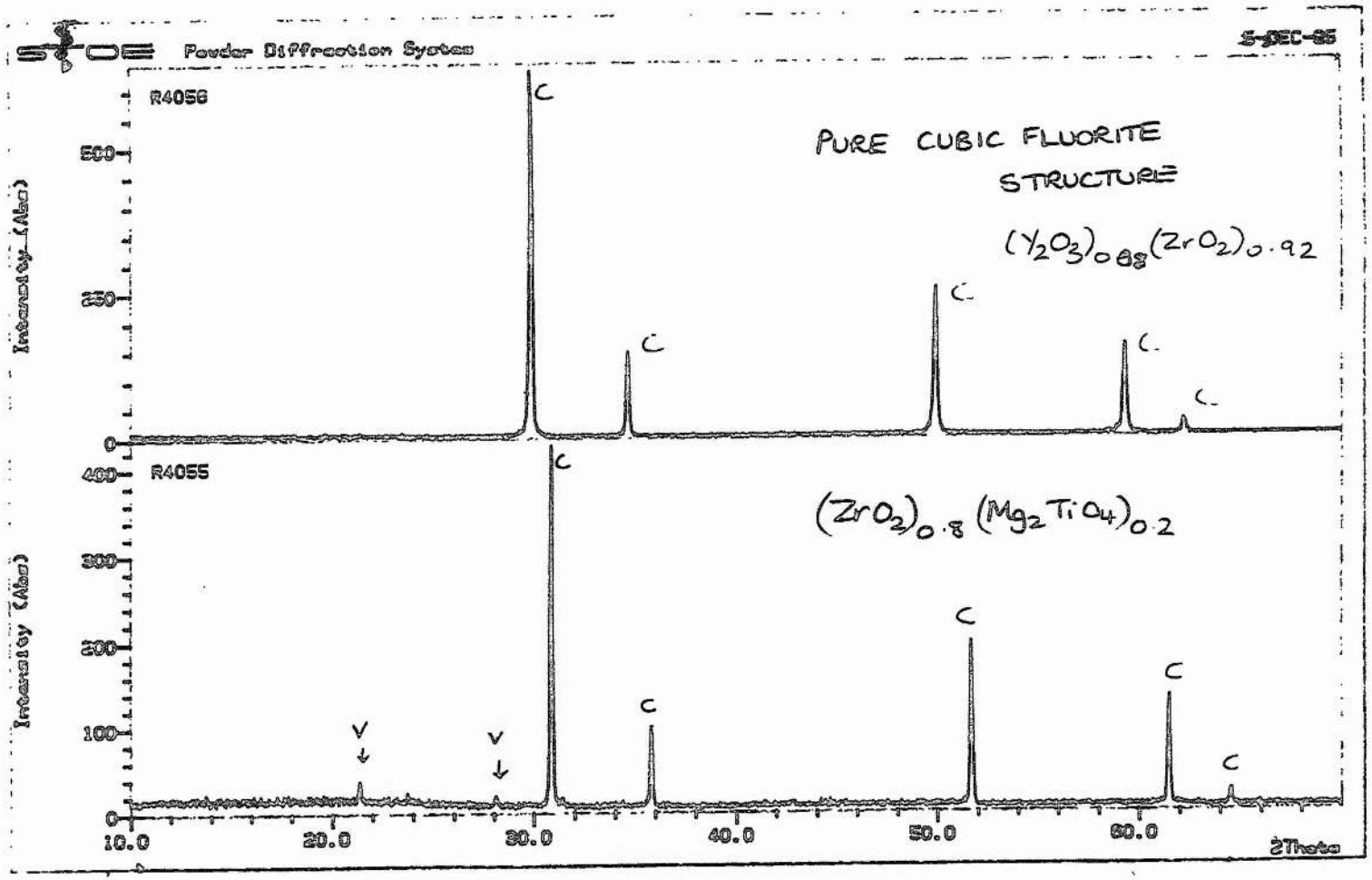

Figure 3.4: X-ray pattern for Sample 18: $(ZrO_2)_{0.8}$ $(Mg_2TiO_4)_{0.2}$

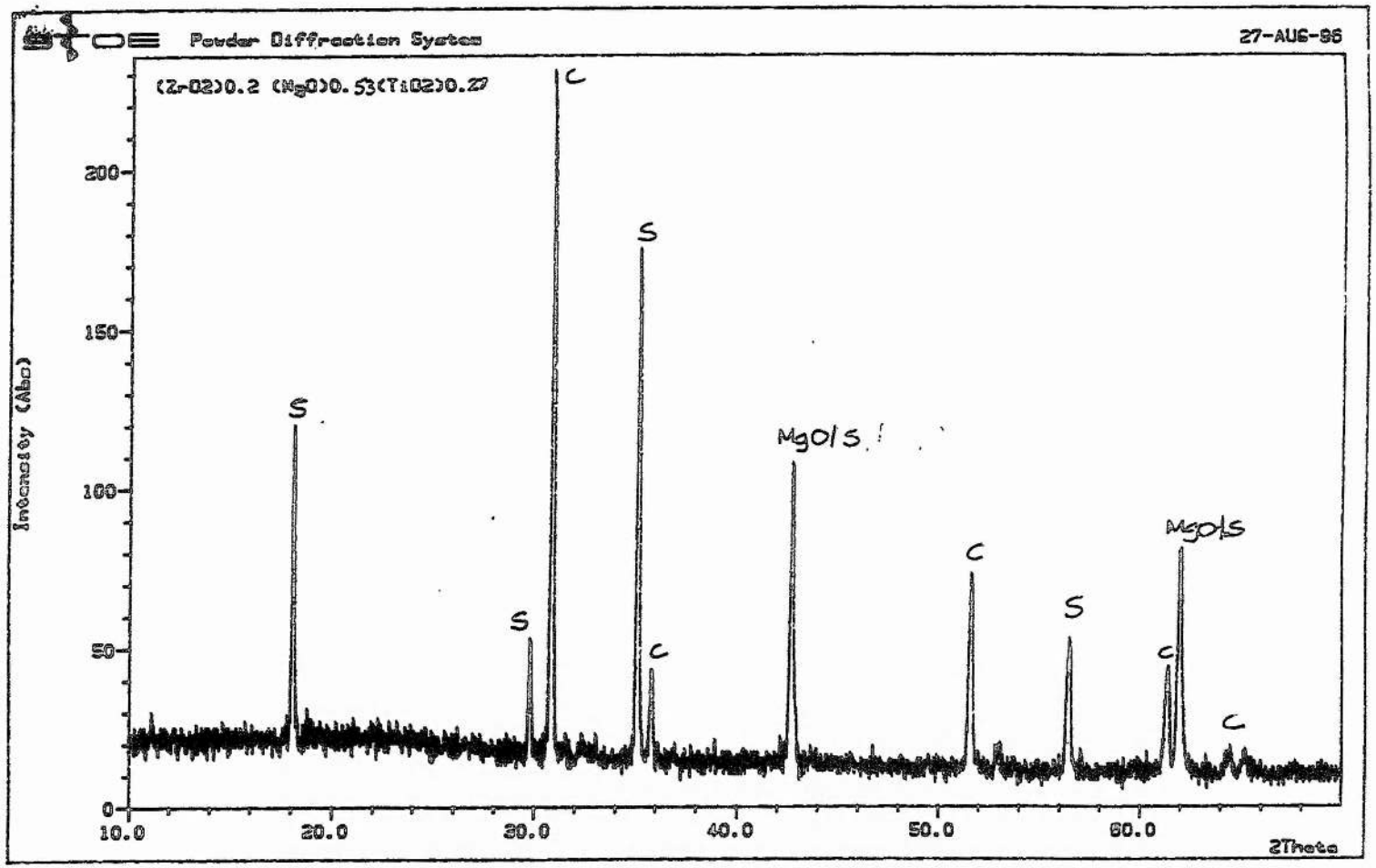

Figure 3.5: X-ray pattern for Sample 1: $(ZrO_2)_{0.2}$ $(MgO)_{0.53}$ $(TiO_2)_{0.27}$

certain quantity of spinel is soluble in the cubic-fluorite structure. Once the cubic-fluorite structure has been stabilised, any unreacted magnesium titanate will be left in its original form.

Due to the presence of MgO and no evidence of TiO_2 peaks, it implies that all of the titanium ions have been substituted into the cation sites. When Mg^{2+} ions (with a similar ionic radius as zirconium) are substituted into the distorted cubic-fluorite structure, two oxygen vacancies are created. However, for titanium ions (which have a smaller ionic radius than zirconium), the titanium ion replaces the zirconium cation with no oxygen vacancies. As it can be seen from Table 3.2, when a sample contains titanium ions, the unit-cell size of the cubic-fluorite phase is smaller. For a sample which contains yttria, which has a larger ionic radius than zirconium, the unit-cell size of the cubic-fluorite phase will be larger than pure-cubic-fluorite zirconia. By refining lattice parameters on the $(ZrO_2)_{0.54}(MgO)_{0.31}(TiO_2)_{0.15}$ sample, it was found that the unit-cell size was smaller than pure cubic-fluorite zirconia implying that all the titanium ions had indeed been substituted into the cubic-fluorite structure. It has been explained in the literature, that for similar systems[7], wiith increasing concentrations of vacancies, the cations move away from the oxygen vacancies and the oxygen vacancies move away from the cations, thus causing the lattice to expand.

The second half of the M_2T:Z(c) join which involves samples 16, 17, 19, 20, 25-27 and 32, there are two clear and distinct phases present: magnesium oxide and cubic-fluorite phase zirconia. However, upon further investigation, using the magnesium titanate X-ray pattern, it was noted that the peak at $2\theta = 42.5$ in Figure 3.6 had a higher intensity than expected, considering that the ratio of intensity between the peak at $2\theta = 35$ and $2\theta = 42.5$. Analysis of the magnesium oxide JCPDS file[1] revealed that the most intense peak of magnesium oxide is at $2\theta = 42.5$, implying that MgO is present.

Table 3.2: Unit cell sizes of selected samples containing the cubic-fluorite phase

Sample	Phases present	Unit Cell Size/
$(ZrO_2)_{0.92}$ $(Y_2O_3)_{0.08}$	C	5.139(5)
$(ZrO_2)_{0.85}$ $(MgO)_{0.15}$	C	5.122(6)
$(ZrO_2)_{0.54}$ $(MgO)_{0.31}$ $(TiO_2)_{0.15}$	C + MgO + S	4.999(6)
ZrO_2 (quenched from 2500°C)[2]	C	5.080(3)
$(ZrO_2)_{0.8}$ $(MgO)_{0.1}$ $(TiO_2)_{0.1}$	C	4.992(3)
$(ZrO_2)_{0.571}$ $(MgO)_{0.287}$ $(TiO_2)_{0.1416}$	C+ MgO + S	5.047(4)
$(ZrO_2)_{0.81}(MgO)_{0.127}(TiO_2)_{0.063}$	C + M	5.003(7)

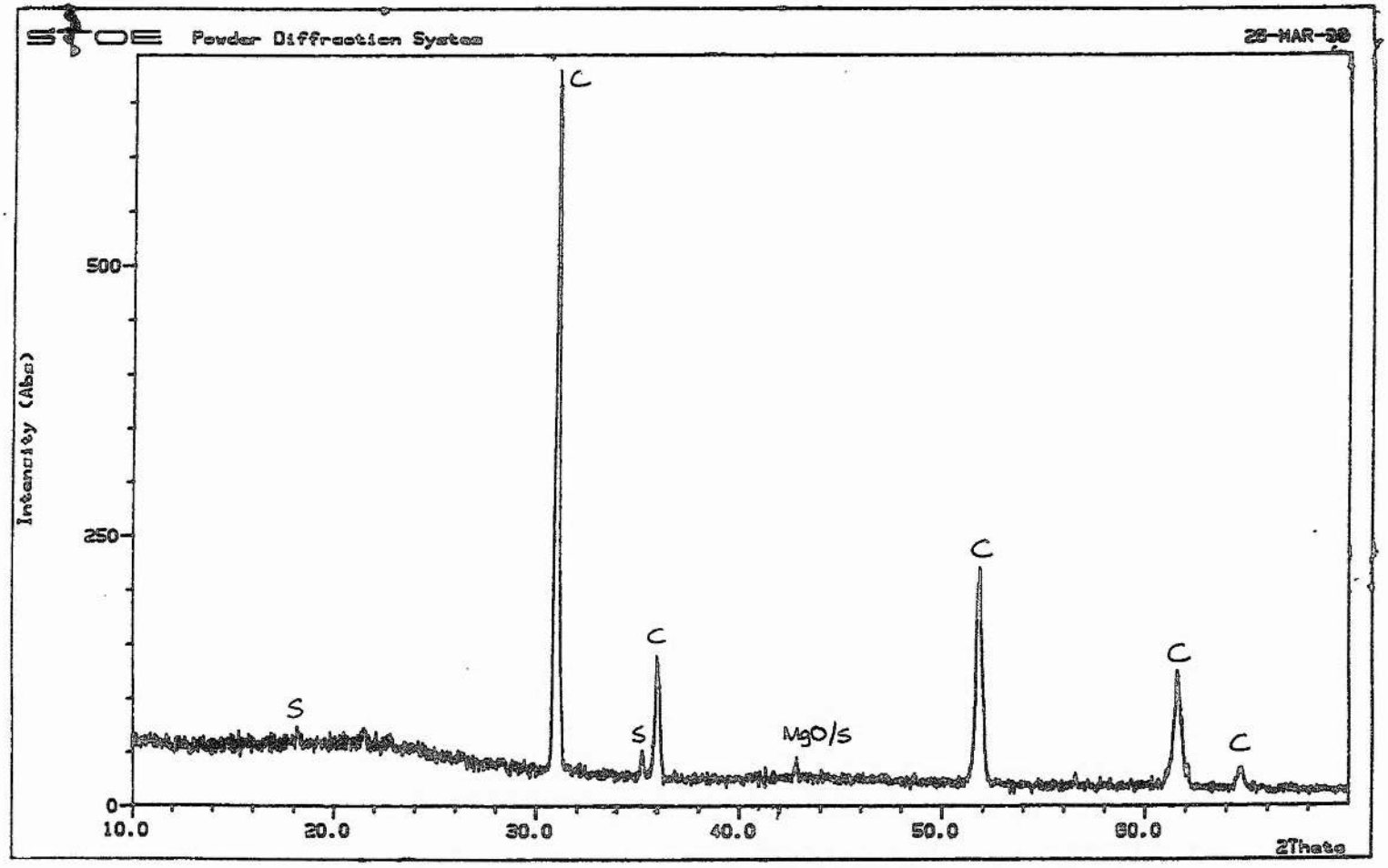

Figure 3.6: X-ray pattern for Sample 32: $(ZrO_2)_{0.7}\ (MgO)_{0.201}\ (TiO_2)_{0.099}$

This would imply that a general trend is being followed along the M_2T:Z(c) phase join because, as the amount of magnesium titanate is reduced, the amount of magnesium titanate being left unreacted is decreasing. Support for this trend is very clearly shown when comparing the X-ray patterns for samples 1 (Figure 3.5) and 32 (Figure 3.6). In sample 1, the magnesium titanate peaks are clearly visible whereas in sample 32, the peaks are only just visible and easily missed

The cubic-fluorite and MgO biphasic region

The second region of the phase diagram containing samples 30, 37, 38 and 39, on the MgO-rich side of the line joining Z(c)and Mg_2TiO_4 there are two phases present: magnesium oxide and cubic-fluorite phase zirconia. Sample 37 is on the MgO:ZrO_2 binary phase line and by checking the MgO:ZrO_2 binary phase diagram (Figure 1.15), the results agreed with the previous report[4]. For samples 30, 38 and 39, there is too little titanium dioxide present in the reaction mixture for titanium ions to play a major role in the stabilisation of the final product. Such behaviour has been observed in other related systems[8]. The presence of magnesium oxide implies that there is an excess of dopant present meaning, that for pure cubic-fluorite samples to be synthesised, the amount of MgO dopant will have to be reduced further.

The $ZrTiO_4$ single-phase region

The X-ray patterns for samples 12 and 13 were in accord with the orthorhombic ($ZrTiO_4$) structure. This means that, for at least, this region of the phase diagram, the experimental results coincided with those of the literature[6]. The unit-cell lengths of the orthorhombic structure were calculated and are shown in Table 3.3 and it was noted that the experimental values of ZT (Sample 12) gave a good agreement with the values obtained with the

Table 3.3 Unit cell data derived for orthorhombic values

Sample Number	Composition			Unit Cell Data/Å		
	ZrO_2	MgO	TiO_2	a	b	c
12	50	----	50	5.0382(3)	5.4875(2)	4.8021(5)
13	40	3.6	56.4	5.0265(3)	5.5432(8)	4.7912(5)
reference values [8]	50	----	50	5.0385(5)	5.4874(6)	4.8048(6)

previous report[9] . The change in unit cell for sample 13 confirms the presence of a solid solution in this region of the phase diagram.

The distorted pseudobrookite and cubic-fluorite phase region

Sample 4 consists of both distorted pseudobrookite and cubic-fluorite structures which agrees with the previous report[6]. However for samples 11, 29, 31, 34 and 35 which from the previous report[6] were expected to be cubic-fluorite phase only, instead of both distorted pseudobrookite and cubic-fluorite phase. This anomaly is further confirmation that the phase limit for where the pure cubic-fluorite structure is supposed to exist is incorrect. As there is obviously an excess of dopant present, the amount of dopant must be reduced further, if single phase cubic-fluorite samples are to be synthesised.

The tetragonal-zirconia single-phase region

In samples 36, 49, 57, 61 and 62, there was only one phase present: monoclinic zirconia. As there is a high proportion of zirconia present and with very little dopant available in the reaction mixture, it is not surprising that the final product was related to one of the zirconia polymorphs. At high temperatures, the samples exist in the tetragonal form and upon cooling, the samples revert back to the monoclinic-form. The tetragonal polymorph, as explained in Chapter 1, is unstable at room temperature which means that upon X-ray analysis at room temperature, only the monoclinic structure would be observed, whereas a X-ray pattern at 1200°C would show the tetragonal structure.

Titania-rich region

Sample 6 which is just outwith the orthorhombic phase boundary consists of both the orthorhombic and rutile (TiO_2) structures as expected from the previous report[6]. For sample 5, three phases were present: distorted

pseudobrookite, rutile (titanium dioxide) and orthorhombic $ZrTiO_4$ which was also expected. The actual reason behind synthesising such samples was to ensure that the previous report[6] was accurate in determining the phases present in other regions of the phase diagram, apart from the cubic-fluorite phase region.

The cubic-fluorite, ilmenite and spinel phase region

For samples 3, 8 and 10 which are on the line joining the compositions $MgTiO_3$ and Z(c), three phases were present: cubic-fluorite, ilmenite and spinel (Figure 3.7). In samples 23, 24, 28 and 33, which are also on this line, there are three phases present: spinel, magnesium oxide and the cubic-fluorite phase. Clearly the binary phase join between the spinel and cubic-fluorite must cross the composition line joining $MgTiO_3$ and ZrO_2 as shown in Figure 3.8.

The cubic fluorite, MgO and spinel phase region

Samples 21 and 22 were on the MgO-rich side of the M_2T:Z(c) phase join, and contain magnesium titanate, magnesium oxide and cubic-fluorite phase zirconia. The amount of magnesium titanate present decreases as the amount of titanium dioxide present in the solid solution increases.

The single phase cubic-fluorite region

Single phase cubic-fluorite samples have been located at points 44, 47, 50, 51, 55 and 58. Table 3.4 gives the unit cell data of those samples in angstroms. The general trend appears to be that as the amount of titanium dioxide is increased, the unit cell edge of the cubic-fluorite sample decreases due to the increased presence of the titanium species in the fluorite phase. Figure 3.9 is a graph of titanium content versus unit-cell edge of the cubic-fluorite phase. It was noted that the cubic-fluorite peaks in the X-ray pattern of sample 58 are rather broad (Figure 3.10) implying the non-attainment of

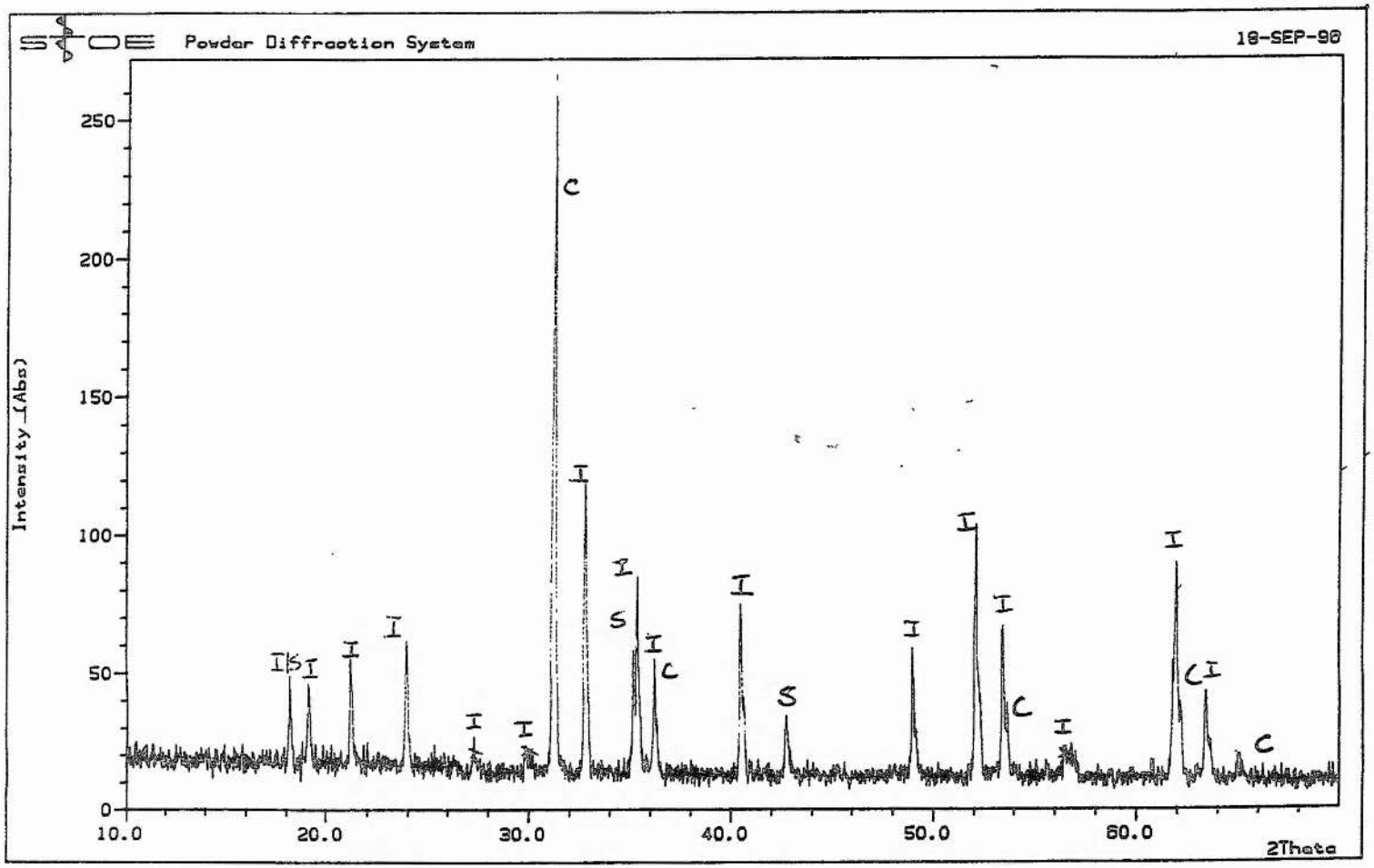

Figure 3.7: X-ray pattern for Sample 8: $(ZrO_2)_{0.4}$ $(MgO)_{0.3}$ $(TiO_2)_{0.3}$

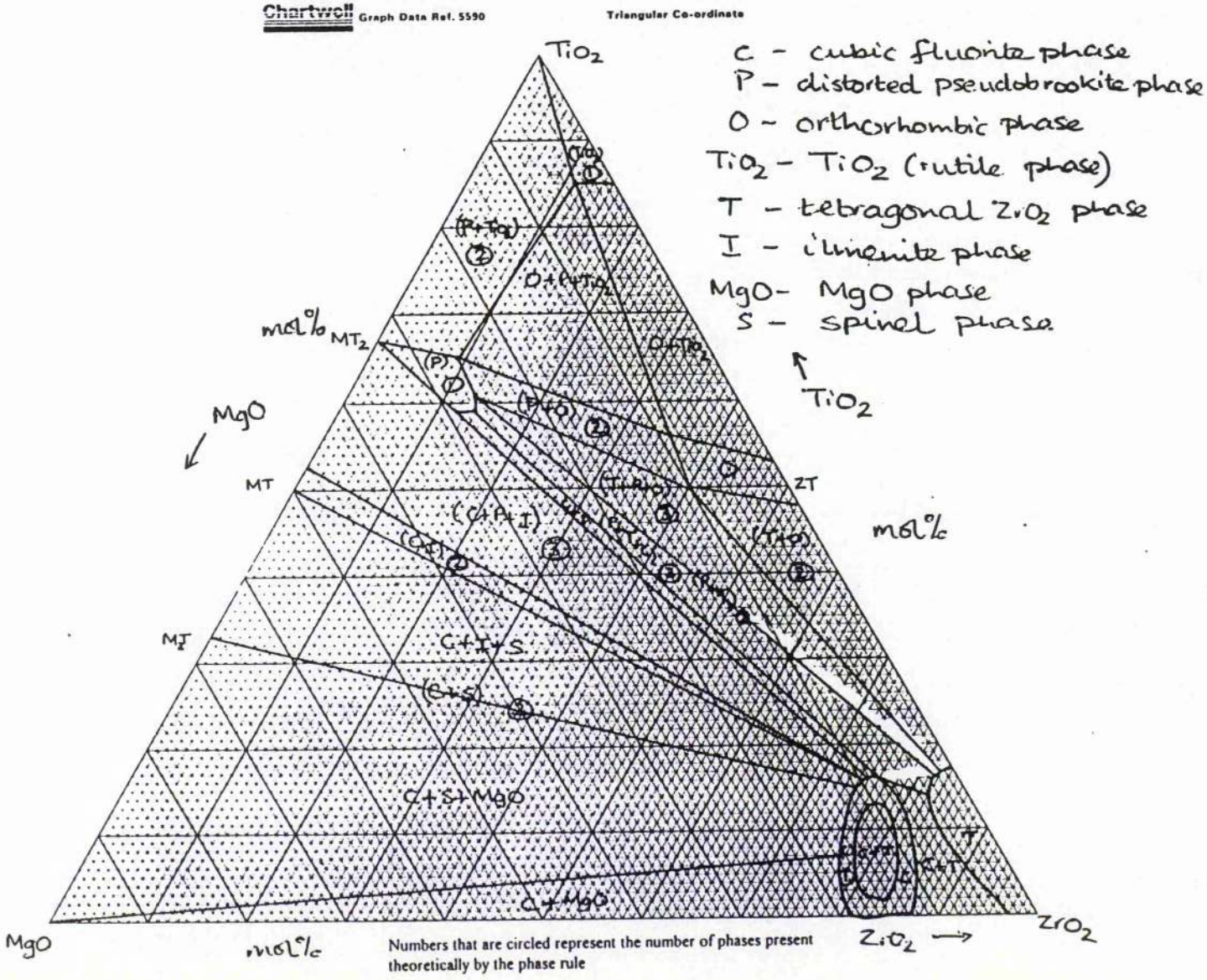
Chartwell Graph Data Ref. 5590
Triangular Co-ordinate
TiO2
C - cubic fluorite phase
P - distorted pseudobrookite phase
O - orthorhombic phase
TiO2 - TiO2 (rutile phase)
T - tetragonal ZrO2 phase
I - ilmenite phase
MgO - MgO phase
S - spinel phase
mol% MT2
MgO
MT
ZT
mol%
MI
C+I+S
C+S+MgO
C+MgO
MgO
mol%
ZrO2
Numbers that are circled represent the number of phases present theoretically by the phase rule

Table 3.4: Unit cell data for samples containing cubic-fluorite phase only

Sample	Unit cell edge / Å
$(ZrO_2)_{0.85}$ $(MgO)_{0.15}$	5.122(6)
$(ZrO_2)_{0.86}$ $(MgO)_{0.119}$ $(TiO_2)_{0.021}$	5.054(4)
$(ZrO_2)_{0.86}$ $(MgO)_{0.0933}$ $(TiO_2)_{0.0467}$	5.016(7)
$(ZrO_2)_{0.8}$ $(MgO)_{0.1}$ $(TiO_2)_{0.1}$	4.992(3)
$(ZrO_2)_{0.75}$ $(MgO)_{0.1025}$ $(TiO_2)_{0.1475}$	4.967(8)

Figure 3.9: Graph illustrating the variation of unit cell edge with titanium content

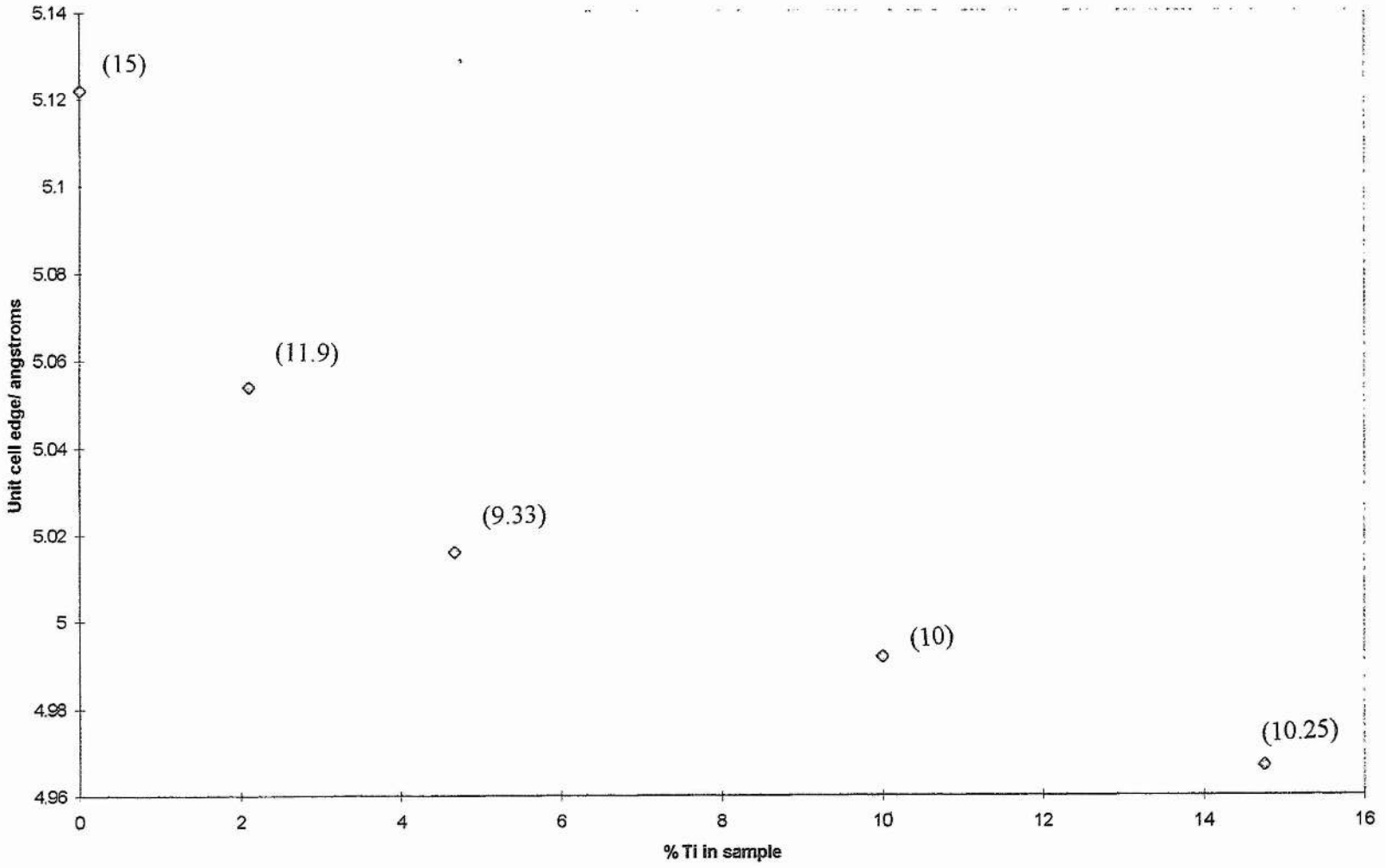

Figures in brackets represent MgO content

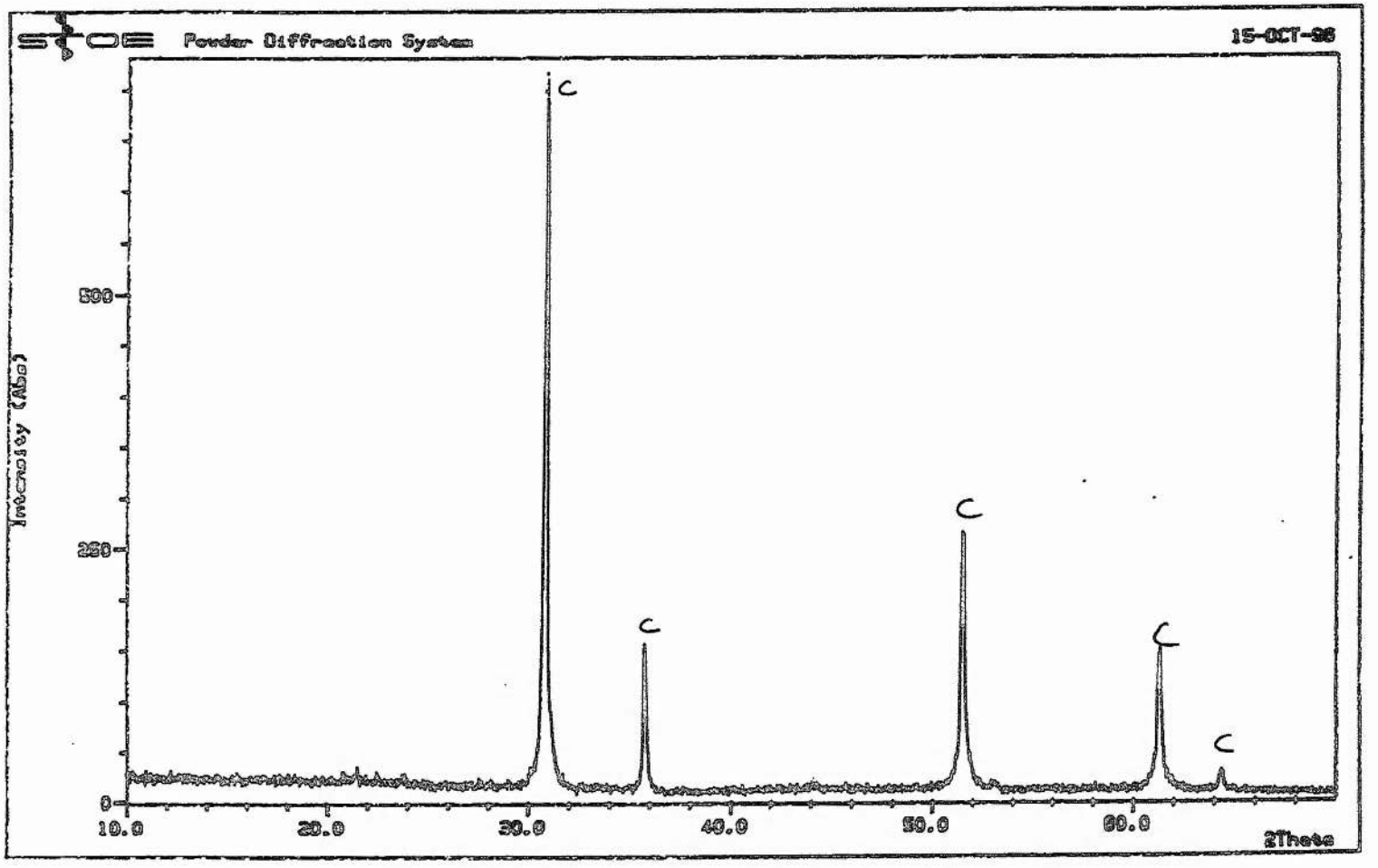

Figure 3.10: X-ray pattern for Sample 58: $(ZrO_2)_{0.84}\ (MgO)_{0.08}\ (TiO_2)_{0.08}$

equilibrium. It may be possible to attain the equilibrium state using higher temperatures or longer reaction times.

The tetragonal and cubic-fluorite phase region

On the ZrO_2-rich side of the cubic-fluorite single phase region, there is a two phase region: cubic-fluorite phase and monoclinic zirconia which involves samples 46, 48, 56 and 57. At 1500°C, the monoclinic phase would have existed in the tetragonal form. Such behaviour is not unusual because if the $MgO:ZrO_2$ phase diagram is considered (Figure 1.15), at compositions between 3 and 14% MgO, there is a similar two phase region present at 1500°C: tetragonal zirconia and cubic-fluorite phase. This is further evidence that the previous report[6] was incorrect in determining a large single-phase region in the zirconia-rich region.

The two-phase region within the cubic-fluorite domain

The final region of the phase diagram where samples 40-43, 45, 52, 53 and 54 are concerned, there are two phases present: monoclinic zirconia and the cubic-fluorite phase. This is rather surprising as in the samples whose compositions are either MgO-rich or MgO-deficient with respect to this region show the presence of cubic-fluorite, but not of tetragonal zirconia. By sketching a circle round the cubic-fluorite phase samples, and by making the assumption that a crescent of single-phase cubic-fluorite exists between samples 45 and 51, it can be seen that the bi-phasic region is in the centre of circle drawn. This region must imply that in the central part of the cubic-fluorite domain the stability limit of the cubic-fluorite form is above 1500°C. At higher temperatures, the entire region might be expected to be cubic-fluorite phase only.

The yttria-stabilised zirconia experiment

For comparison purposes, selected samples of yttria-stabilised zirconia were doped with an appropriate quantity of magnesium titanate precursor to see if similar trends were observed when subjected to similar experimental treatment as the M_2T:Z(c) samples. Table 3.5 shows the samples that were selected alongside with the final products obtained after experimental treatment and the unit-cell size of the cubic-fluorite phase.

As it can be seen from Table 3.5 that similar trends are observed when compared to the trend observed with the M_2T:Z(c) samples as there is no evidence of any titanium dioxide peaks present in the samples, implying that the titanium ions are not much less soluble in yttria-stabilised zirconia than magnesium ions. By studying the unit-cell sizes of the cubic-fluorite phase, it was noted that the unit-cell size is smaller than the cubic-fluorite phase of yttria-stabilised zirconia and larger than that of pure cubic-fluorite phase zirconia. As MgO was precipitated, it implies that the titanium ions have been substituted into the cation sites of the cubic-fluorite structure, leading to a decrease in the unit-cell size of the cubic-fluorite phase.

3.3 Quenched samples

The samples shown in Table 2.3 were quenched in small masses of platinium foil in contrast to the conventional method of removing the samples from the furnace in alumina crucibles, as it was thought that the sample might reverse back to its original structure during the slow cooling period in alumina. Table 3.6 shows the results that were obtained, as well as the results that were obtained by the conventional procedures as described in Chapter 2.3. From these results, it would appear that quenching has no significant effect on the samples that were prepared by the conventional methods described in Chapter 2.

Table 3.5: Results for the yttria-stabilised zirconia experiment

Sample	Composition			Phases present
	Y_2O_3	Mg_2TiO_4	ZrO_2	
$Y_{0.128}Zr_{0.736}Mg_{0.4}Ti_{0.2}O_{2.464}$	6.4	20	73.6	Cubic-fluorite + MgO
$Y_{0.152}Zr_{0.874}Mg_{0.1}Ti_{0.05}O_{2.176}$	7.6	5	87.4	Cubic-fluorite + MgO
$Y_{0.158}Zr_{0.91}Mg_{0.02}Ti_{0.01}O_{2.099}$	7.9	1	91.1	Cubic-fluorite + MgO

Sample	Unit Cell edge of cubic-fluorite phase
$Y_{0.128}Zr_{0.736}Mg_{0.4}Ti_{0.2}O_{2.464}$	5.0968(3)
$Y_{0.152}Zr_{0.874}Mg_{0.1}Ti_{0.05}O_{2.176}$	5.1008(7)
$Y_{0.158}Zr_{0.91}Mg_{0.02}Ti_{0.01}O_{2.099}$	5.1230(2)

Table 3.6: Quenched samples results

Before quenching

Sample Number	Composition			Phases present	Unit cell edge/Å
	ZrO_2	MgO	TiO_2		
14	54	30.82	15.18	C + MgO + S	5.054(6)
17	57.1	28.74	14.16	C + MgO + S	5.047(5)
20	60	22.8	15.2	C + MgO + S	5.028(2)
24	67	16.5	16.5	C + MgO + S	5.002(3)
37	75	25	----	C + MgO	5.147(3)
52	81	12.7	6.3	C + M	5.003(7)

After quenching

Sample Number	Composition			Phases present	Unit cell edge/Å
	ZrO_2	MgO	TiO_2		
14	54	30.82	15.18	C + MgO + S	5.049(2)
17	57.1	28.74	14.16	C + MgO + S	5.034(5)
20	60	22.8	15.2	C + MgO + S	5.019(3)
24	67	16.5	16.5	C + MgO + S	4.996(3)
37	75	25	----	C + MgO	5.128(2)
52	81	12.7	6.3	C + M	4.998(4)

The unit-cell edge of the cubic-fluorite phase was calculated and it was found that there was no significant change in the unit-cell edge, implying that quenching has no significant effects on the samples concerned. What was originally thought was that the long cooling periods allowed structure transformations to occur. In reality, it has been shown that the results obtained by quenching are similar to the results obtained by the conventional experimental methods (Figures 3.11 and 3.12) and hence that the samples were cooled fairly rapidly by these conventional methods.

3.4 Annealing techniques

Selected stabilised cubic-fluorite phase samples were annealed at 1000°C for 48 hours prior to DTA analysis. By taking an X-ray pattern of an annealed sample, it will be possible to determine as to whether the cubic-fluorite phase is thermodynamically stable or not at lower temperatures. Table 3.7 shows the thermal history of the samples that were analysed as well as the results that were obtained.

For the annealed samples, the X-ray patterns (Figure 3.13) showed evidence of the cubic-fluorite phase, monoclinic zirconia and magnesium oxide. The presence of MgO and monoclinic zirconia as well as the cubic-fluorite phase at 1000°C implies that the cubic-fluorite phase is thermodynamically unstable. It was also noted that the cubic-fluorite to tetragonal (+ MgO)[4] transition is kinetically limited due to the presence of cubic-fluorite with monoclinic ZrO_2 and MgO in the X-ray pattern.

3.5 DTA analysis

Selected samples as shown in Table 3.8 were subjected to DTA analysis. The X-ray patterns obtained from the annealed samples were used to gain an insight as to what transformations were likely to occur during DTA

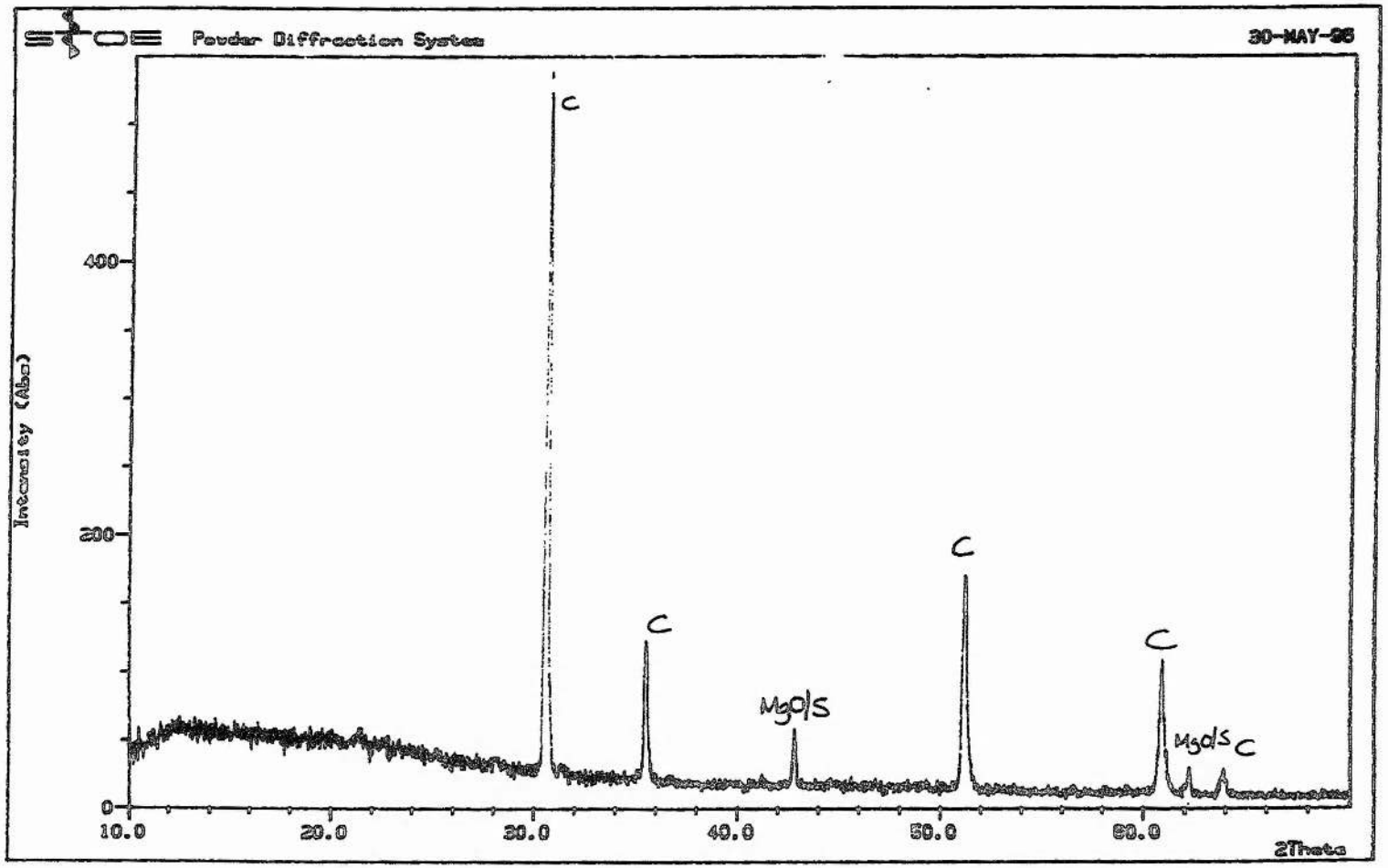

Figure 3.11: X-ray pattern for Sample 17: $(ZrO_2)_{0.57}$ $(MgO)_{0.29}$ $(TiO_2)_{0.14}$ before quenching

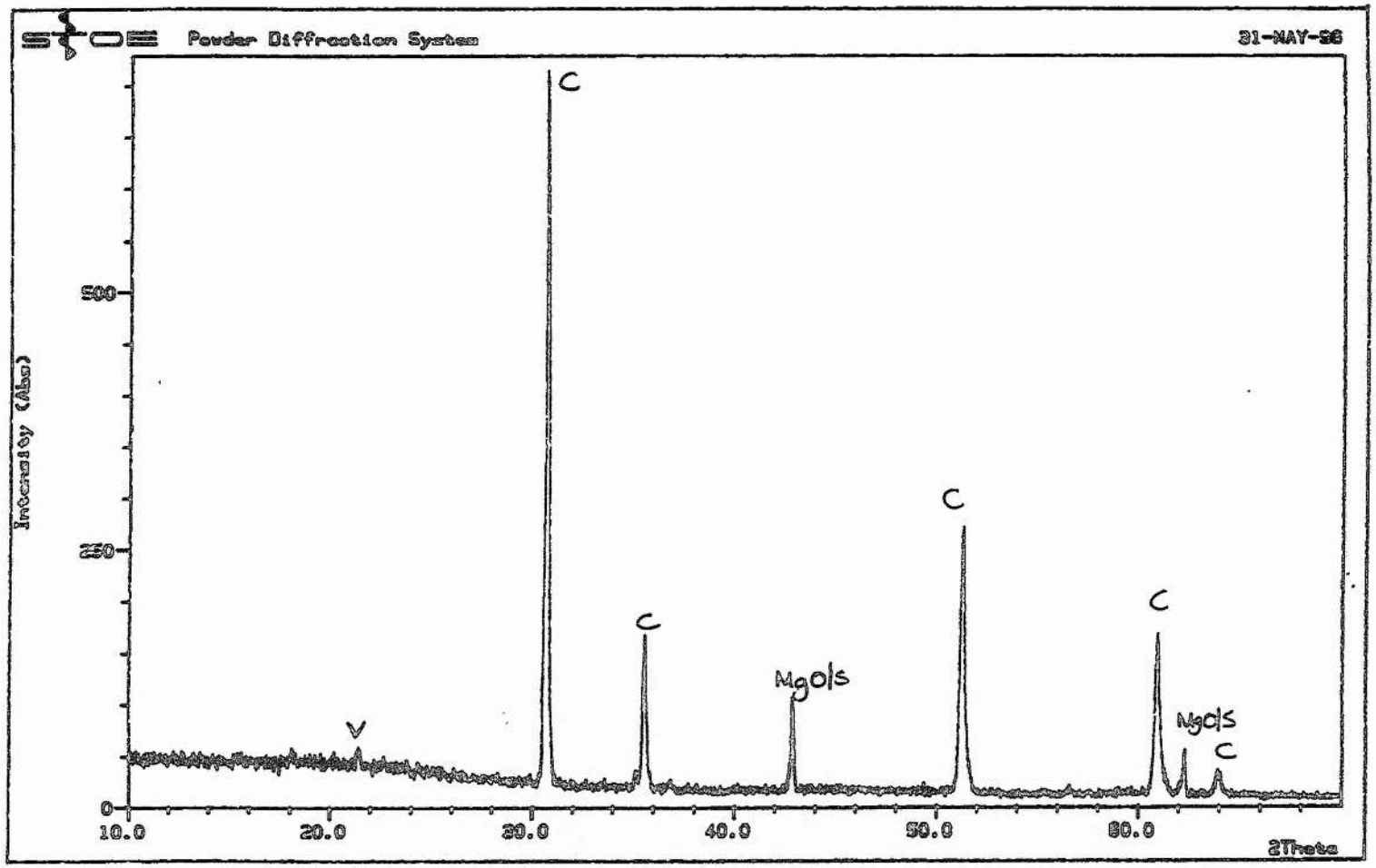

Figure 3.12: X-ray pattern for Sample 17: $(ZrO_2)_{0.57}$ $(MgO)_{0.29}$ $(TiO_2)_{0.14}$ after quenching

Starting composition	Phases present after solid state reaction at 1500°C for 72hrs	Phases present after annealing 1500°C samples at 1000°C for 48hrs
$(ZrO_2)_{0.85}(MgO)_{0.15}$	C	C + MgO + M
$(ZrO_2)_{0.86}(MgO)_{0.119}(TiO_2)_{0.021}$	C	C + MgO + M
$(ZrO_2)_{0.86}(MgO)_{0.0933}(TiO_2)_{0.0467}$	C	C + MgO + M
$(ZrO_2)_{0.8}(MgO)_{0.1}(TiO_2)_{0.1}$	C	C + MgO + M
$(ZrO_2)_{0.75}(MgO)_{0.1025}(TiO_2)_{0.1475}$	C	C + MgO + M

Table 3.7: Results of 1000°C annealed samples

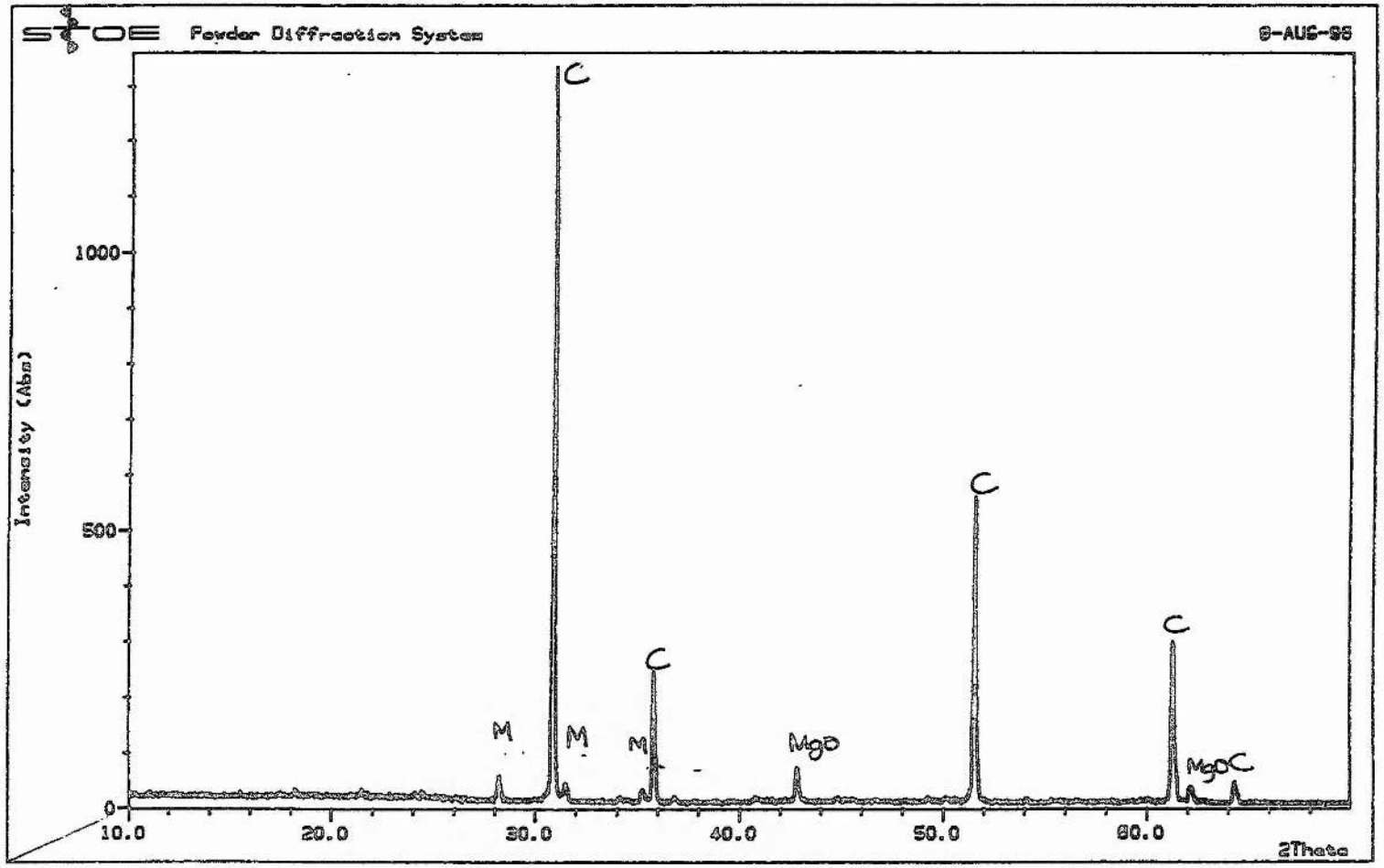

Figure 3.13: X-ray pattern of $(ZrO_2)_{0.86}$ $(MgO)_{0.0933}$ $(TiO_2)_{0.0467}$ after annealing at 1000°C for 48 hours

Starting composition	Phases present after solid state reaction at 1500°C for 72hrs	Transition temperatures
monoclinic zirconia (Hopkins)	n/a	forwards 1150°C reverse 850°C
monoclinic zirconia (Tioxide)	n/a	forwards 1190°C reverse 900°C
$(ZrO_2)_{0.85}(MgO)_{0.15}$	C	forwards 1320°C reverse 1320°C
$(ZrO_2)_{0.86}(MgO)_{0.119}(TiO_2)_{0.021}$	C	forwards 1310°C reverse 1310°C
$(ZrO_2)_{0.86}(MgO)_{0.0933}(TiO_2)_{0.0467}$	C	forwards 1305°C reverse 1305°C
$(ZrO_2)_{0.8}(MgO)_{0.1}(TiO_2)_{0.1}$	C	forwards 1290°C reverse 1290°C
$(ZrO_2)_{0.75}(MgO)_{0.1025}(TiO_2)_{0.1475}$	C	forwards 1210°C, 1310°Cand 1350°C reverse at 1310°C and 1350°C

Starting composition	Transitions occuring
monoclinic zirconia (Hopkins)	forwards: monoclinic to tetragonal reverse: tetragonal to monoclinic
monoclinic zirconia (Tioxide)	forwards: monoclinic to tetragonal reverse: tetragonal to monoclinic
$(ZrO_2)_{0.85}(MgO)_{0.15}$	forwards: tetragonal (+ MgO) to cubic-fluorite reverse: cubic-fluorite to tetragonal (+ MgO)
$(ZrO_2)_{0.86}(MgO)_{0.119}(TiO_2)_{0.021}$	forwards: tetragonal (+ MgO) to cubic-fluorite reverse: cubic-fluorite to tetragonal (+ MgO)
$(ZrO_2)_{0.86}(MgO)_{0.0933}(TiO_2)_{0.0467}$	forwards: tetragonal (+ MgO) to cubic-fluorite reverse: cubic-fluorite to tetragonal (+ MgO)
$(ZrO_2)_{0.8}(MgO)_{0.1}(TiO_2)_{0.1}$	forwards: tetragonal (+ MgO) to cubic-fluorite reverse: cubic-fluorite to tetragonal (+ MgO)
$(ZrO_2)_{0.75}(MgO)_{0.1025}(TiO_2)_{0.1475}$	1290°C: forwards: tetragonal (+ MgO) to cubic-fluorite reverse: cubic-fluorite to tetragonal (+ MgO)

Table 3.8: DTA results

analysis. The information obtained by DTA will be of valuable assistance in the construction of a temperature phase diagram showing what transformations occur during a particular temperature range.

Figures 3.14 and 3.15 show the DTA patterns for two different samples of monoclinic zirconia. The Hopkins zirconia shows the martensitic transformation of the monoclinic phase to the tetragonal phase starting at 1150°Cand upon cooling, the reversible reaction beginning to occur at 850°C whereas with the Tioxide zirconia which has a much smaller particle size, the martensitic transformation begins at 1190°C and the reverse reaction at 900°C . The reason behind the different transformation temperatures is that the two samples have been prepared using different experimental methods by the manufacturers[10]. By knowing the location of where the martensitic transition occurs, it will be possible to check each DTA pattern for evidence of the martensitic transition.

From the X-ray pattern obtained of the 1000°C annealed $(ZrO_2)_{0.85}(MgO)_{0.15}$ sample (Sample 50), which at 1500°C existed in the single cubic-fluorite phase, it was possible to predict what transitions were likely to occur during DTA analysis. The DTA trace for this annealed sample should show evidence of two transitions: monoclinic (+ MgO) to tetragonal (+ MgO) and tetragonal (+ MgO) to cubic-fluorite. As there was evidence of the cubic-fluorite phase at 1000°C, it implies that the reverse transition of cubic-fluorite to tetragonal (+ MgO) may not be as observable as the forward transition from tetragonal (+ MgO) to single phase cubic-fluorite due to the slow reaction kinetics. What was observed (Figure 3.16) was that there was only one broad but sharp peak present in the forward direction at approximately 1320°C and one small peak barely observable at 1320°C. By checking the previous binary phase diagram[4], the transformations can be attributed to the tetragonal (+ MgO) to single-phase cubic-fluorite transformation and vice versa. As expected, the reverse transformation is barely distinguishable implying that not all the cubic-fluorite has been converted back to the

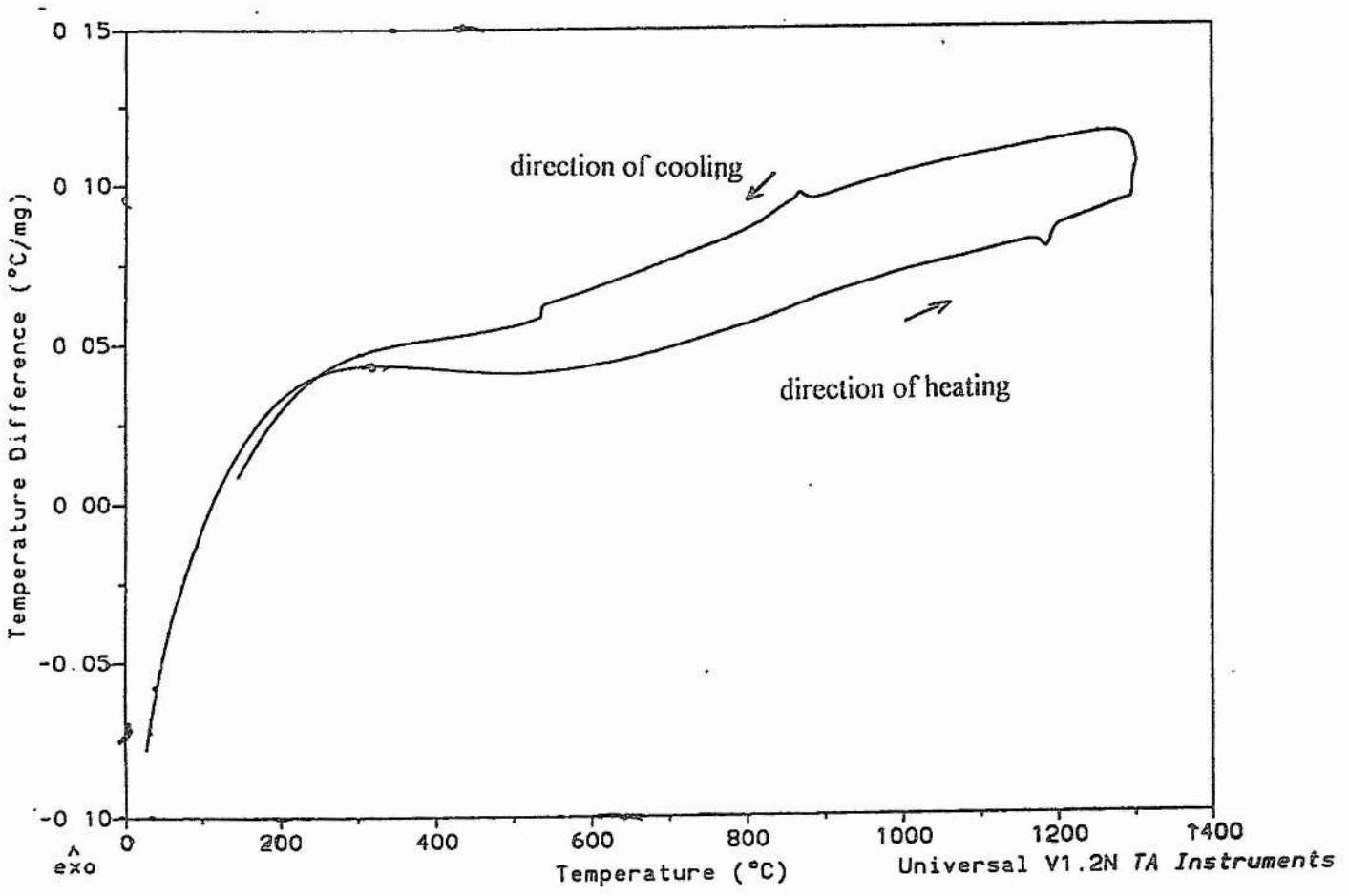

Figure 3.14: DTA pattern for Hopkins monoclinic ZrO_2

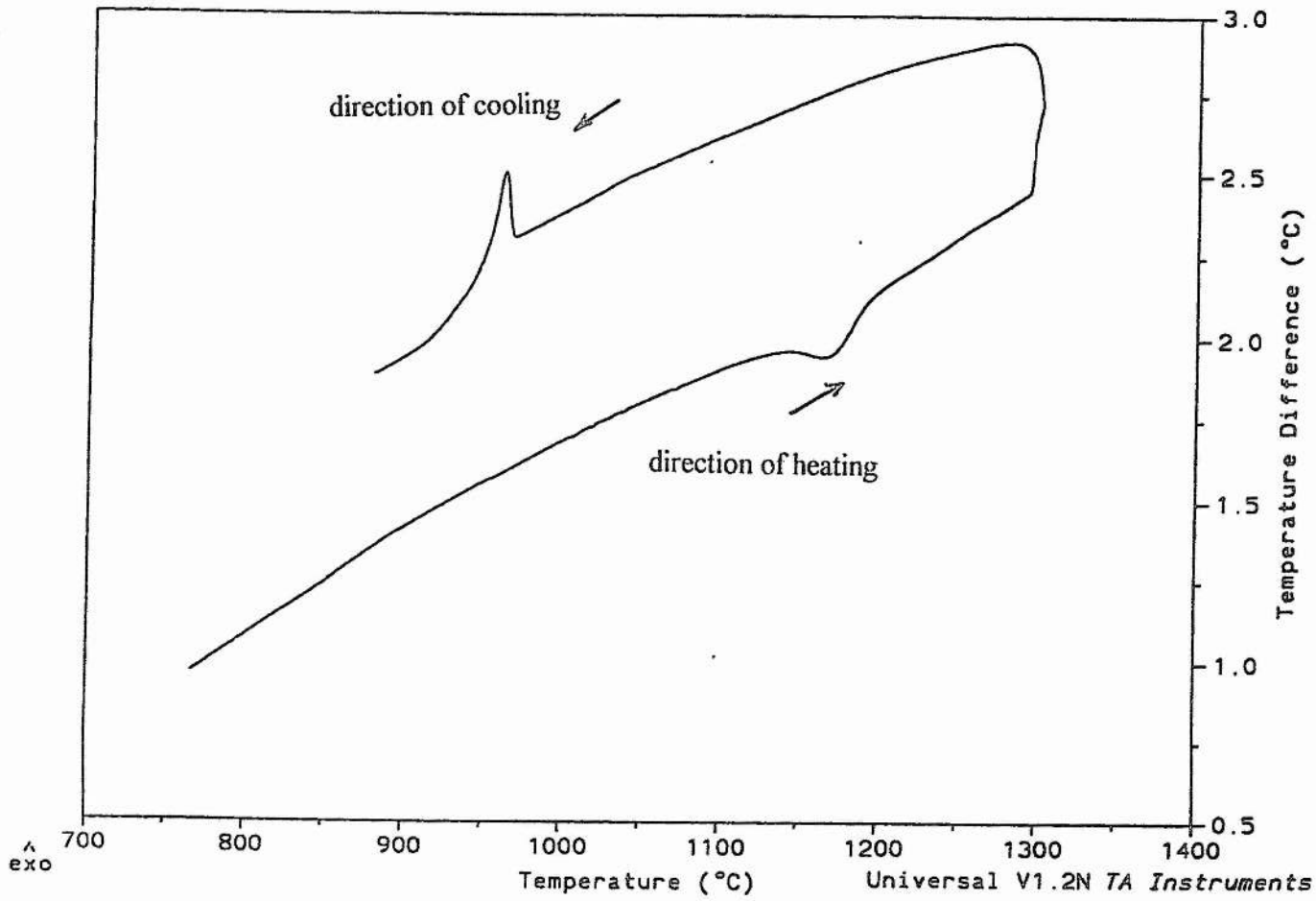

Figure 3.15: DTA pattern for Tioxide monoclinic ZrO_2

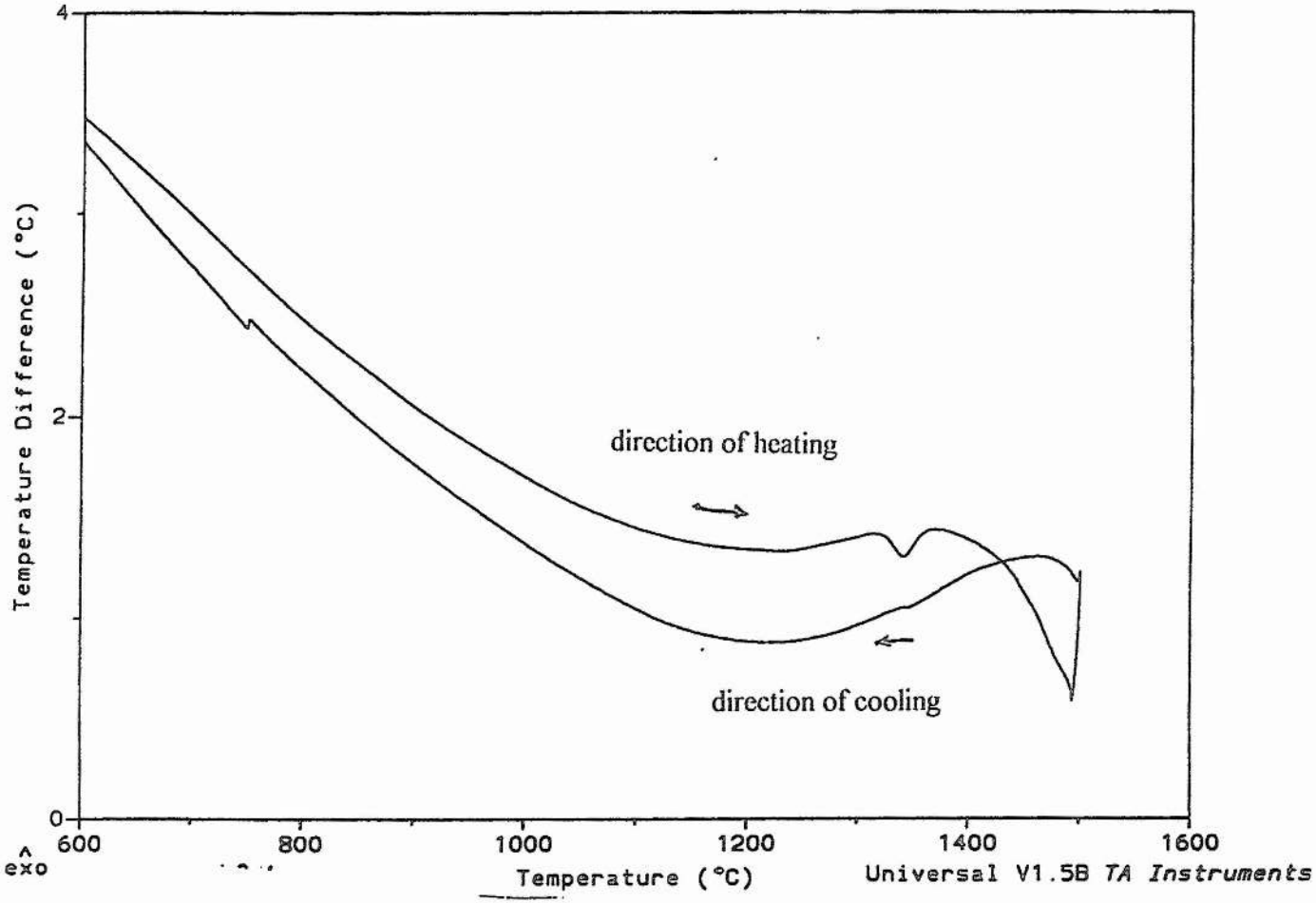

Figure 3.16: DTA pattern for $(ZrO_2)_{0.85}$ $(MgO)_{0.15}$ (Sample 50)

tetragonal (+ MgO) phase. Figure 3.17 shows a possible temperature phase diagram (between 900 and 1500°C), for the forward reaction, taking account of both the previous phase diagram[4] and an X-ray pattern of the $(ZrO_2)_{0.85}(MgO)_{0.15}$ sample which was heated at 1000°C for 48 hours prior to stabilisation of the cubic-fluorite phase which showed evidence of only the monoclinic phase and MgO structure.

A series of 1000°C annealed Mg:Ti:Zr:O samples were investigated. Each of these compositions yielded a cubic-fluorite single phase at 1500°C. The DTA trace (Figure 3.18) for the $(ZrO_2)_{0.86}(MgO)_{0.119}(TiO_2)_{0.021}$ sample (Sample 51), which is close in composition to the $(ZrO_2)_{0.85}(MgO)_{0.15}$ sample, revealed that a similar pattern was observed with a broad but sharp transformation at 1310°C and a barely observable broad peak in the reverse direction at 1310°C which can be again attributed to the tetragonal (+ MgO) to single phase cubic-fluorite transition. A similar case was observed for both $(ZrO_2)_{0.86}(MgO)_{0.0933}(TiO_2)_{0.0467}$ (Sample 55) and $(ZrO_2)_{0.8}(MgO)_{0.1}(TiO_2)_{0.1}$ (Sample 47) samples with the forward transformations occurring at 1305°C and 1290°C respectively and the reverse transformations at 1305°C and 1290°C respectively. However, for the $(ZrO_2)_{0.75}(MgO)_{0.1025}(TiO_2)_{0.1475}$ sample (Sample 44) (Figure 3.19), the DTA trace appeared to be complicated as there were three significant peaks in the forward direction and two less distinguishable peaks in the reverse direction. A possible explanation for this behaviour may be that the sample contained an impurity of some kind and therefore more transitions than expected are noted.

It was surprising that the monoclinic to tetragonal transition at ~ 1000°C was not generally observed. This may imply that the monoclinic to tetragonal transition involves a significant degree of mass transport was that there is a change in the composition at the monoclinic phase during the transition, hence making it difficult to detect by DTA methods. Figure 3.20 gives an approximate temperature phase diagram for the forward reaction of the formation of titanium-stabilised cubic-fluorite samples, making the

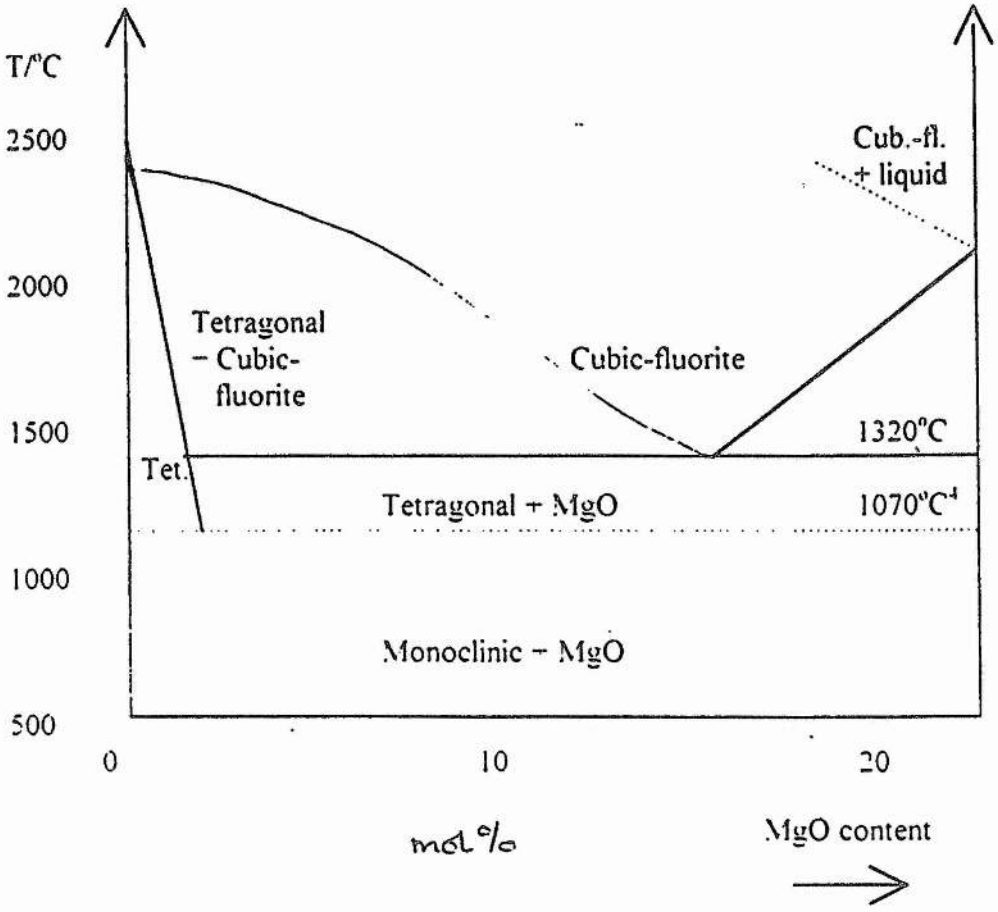

Figure 3.17 Approximate phase diagram for the $MgO:ZrO_2$ system based on both experimental results and the previous report[4]

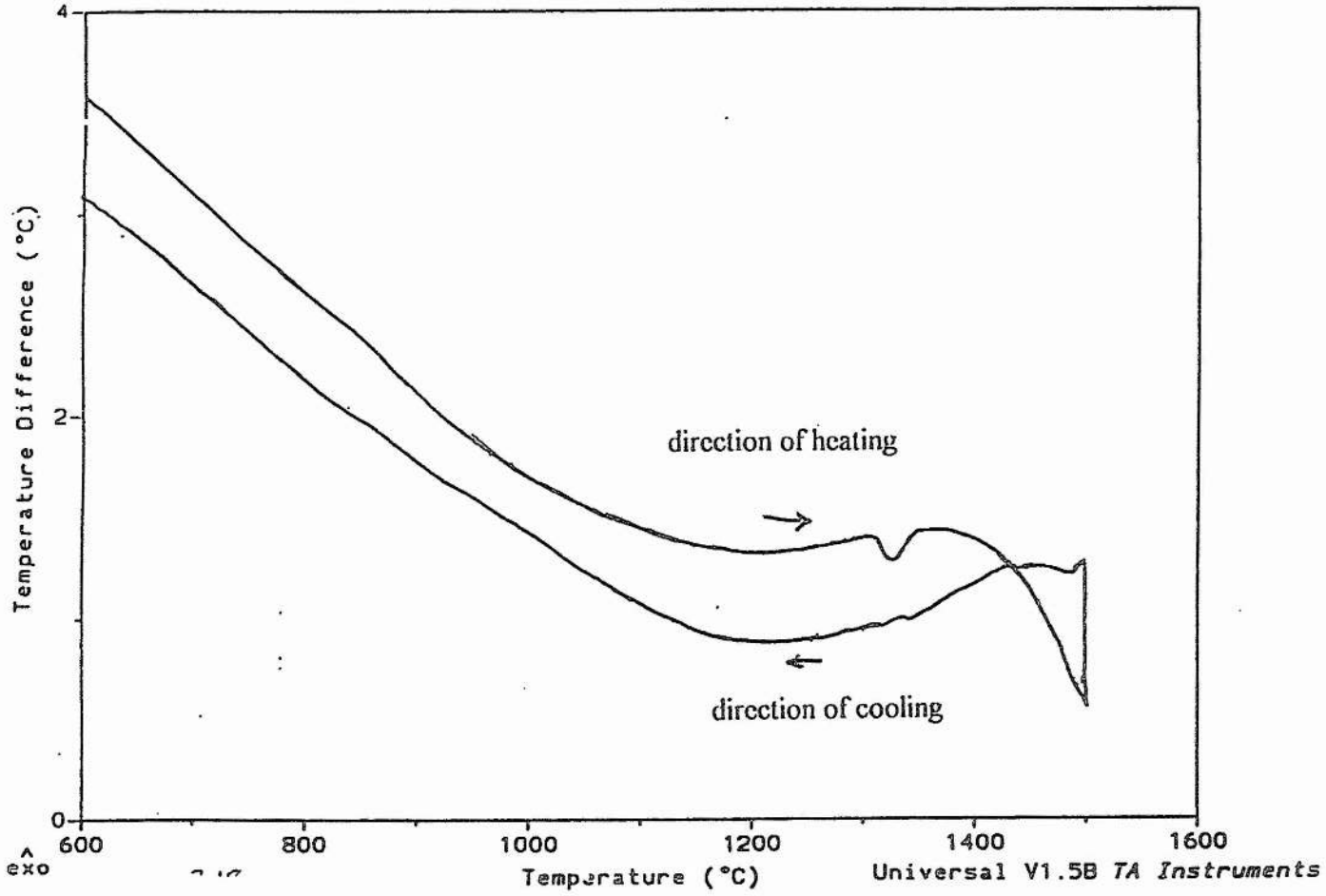

Figure 3.18: DTA pattern for $(ZrO_2)_{0.86}$ $(MgO)_{0.119}$ $(TiO_2)_{0.021}$ (Sample 51)

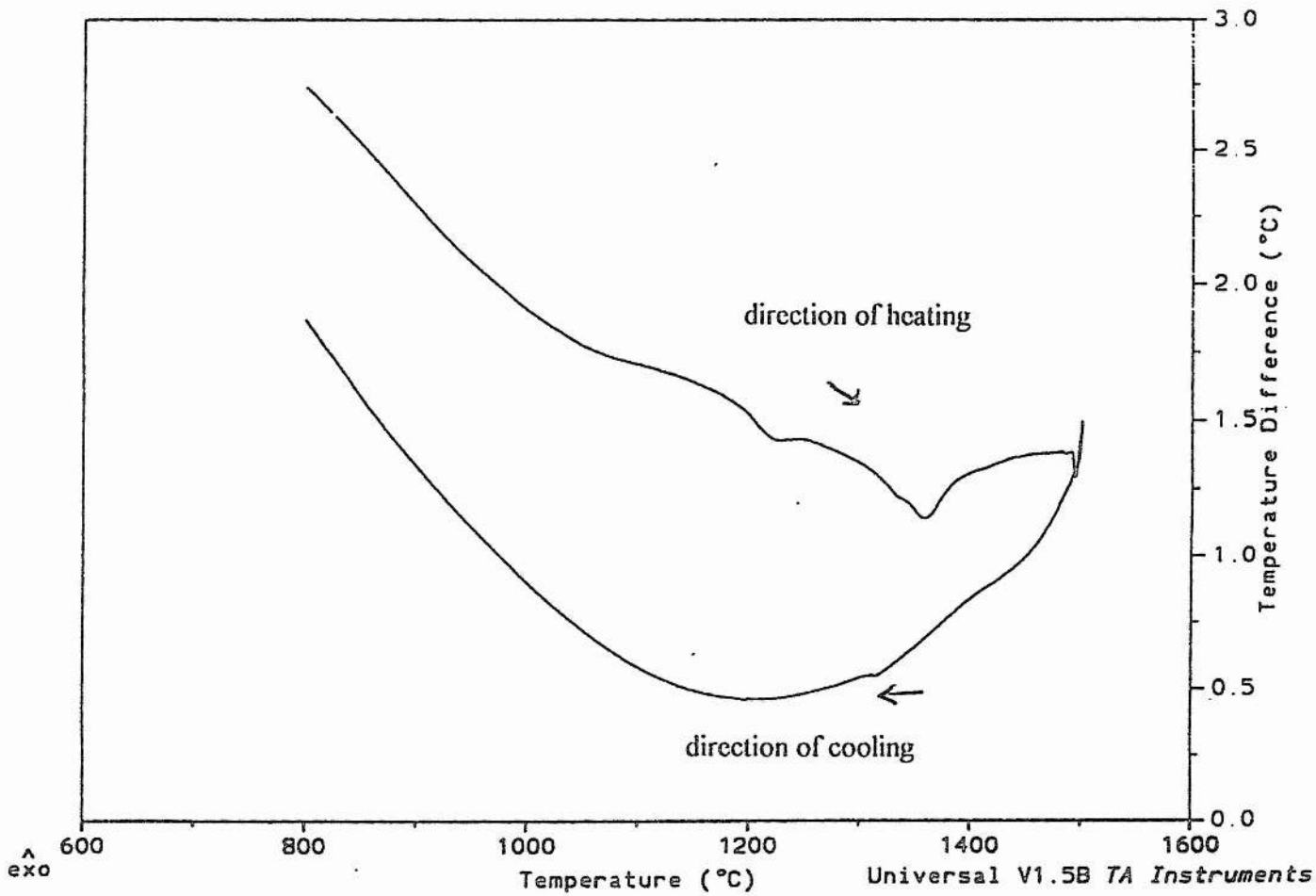

Figure 3.19: DTA pattern for $(ZrO_2)_{0.75}$ $(MgO)_{0.1025}$ $(TiO_2)_{0.1475}$ (Sample 44)

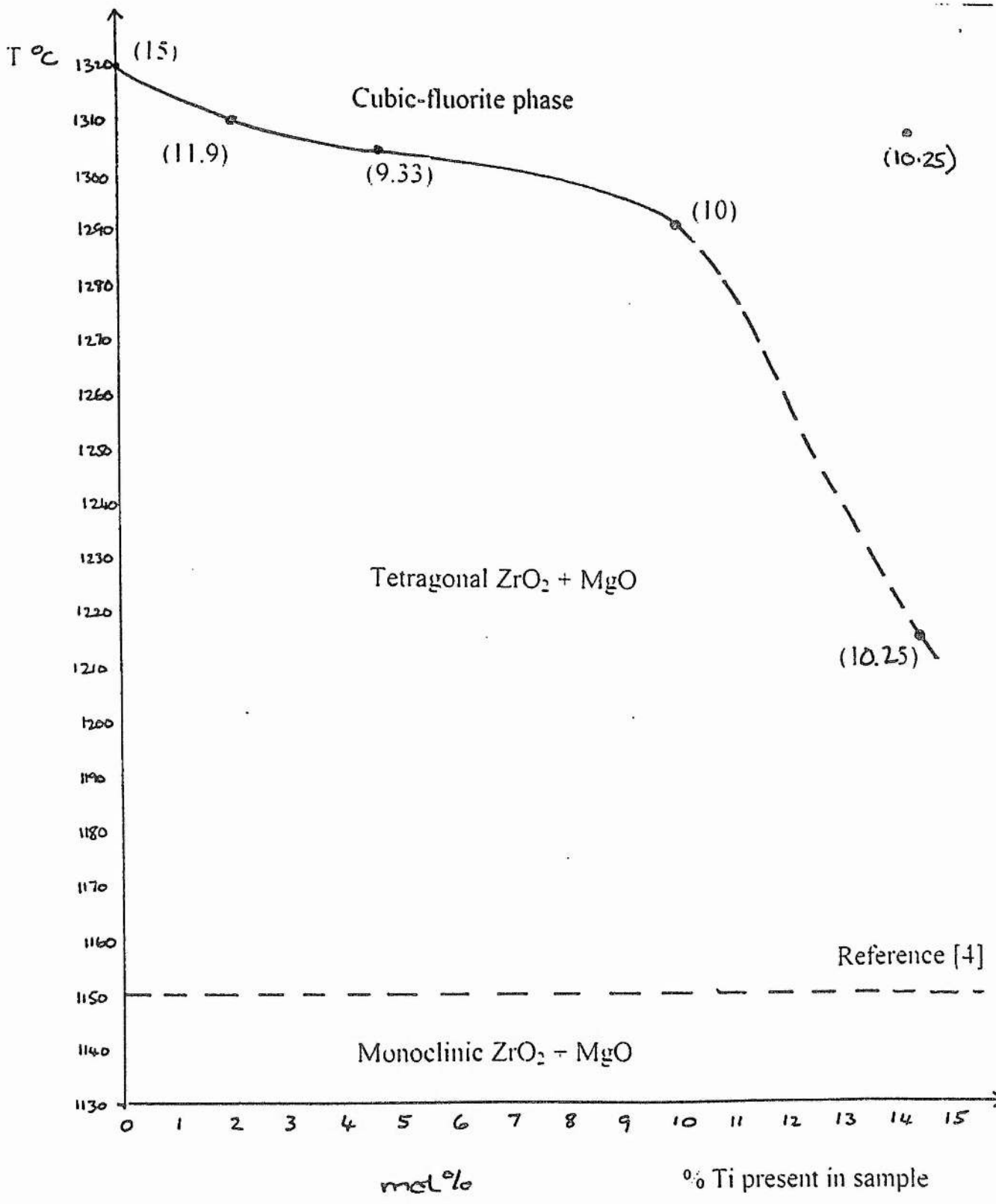

Figure 3 20: Approximate phase diagram for the formation of titanium stabilised zirconia

assumption that the transformation at 1210°C in the $(ZrO2)_{0.75}(MgO)_{0.1025}(TiO_2)_{0.1475}$ (Sample 44) sample is the tetragonal (+ MgO) to single phase cubic-fluorite transition. From Figure 3.20, an interesting trend is observed: as the titanium content in the solid solution increases, the tetragonal (+ MgO) to cubic-fluorite phase transition temperature decreases.

3.6 A.c. impedance results

Figure 3.21 is a typical impedance plot (uncorrected for geometric factor) obtained at 555°C for the $(ZrO_2)_{0.86}$ $(MgO)_{0.0933}$ $(TiO_2)_{0.0467}$ (Sample 55) sample. As there is no evidence of a grain boundary contribution, it implies that the high bulk resistance dominates the grain boundary thus making it difficult to observe a grain boundary resistance. This was the case for all the titanium-doped samples analysed.

The cubic-fluorite samples and two samples which contain other phases as well as the cubic-fluorite phase phase were selected for conductivity measurements. Figure 3.22 gives the conductivity plots for the cubic-fluorite phase samples and it would appear that the samples follow typical Arrhenius-type behaviour with the ionic conductivity increasing with temperature. The activation energy values for both the cubic-fluorite samples and the biphasic samples (cubic-fluorite + other phase) are given in Table 3.9.

Figure 3.23 illustrates the variation of ionic conductivity with TiO_2 concentration, for the $MgO:TiO_2:ZrO_2$ phase system at 800°C. From Figure 3.23, it can be deduced that as the titanium content increases, the conductivity decreases and therefore the activation energy increases as shown in Table 3.9. As titanium is a smaller ion than zirconium, the effect of local distortions and clustering leads to an increase in activation energy and therefore a decrease in the conductivity levels. For yttria-stabilised zirconia, however, where yttrium

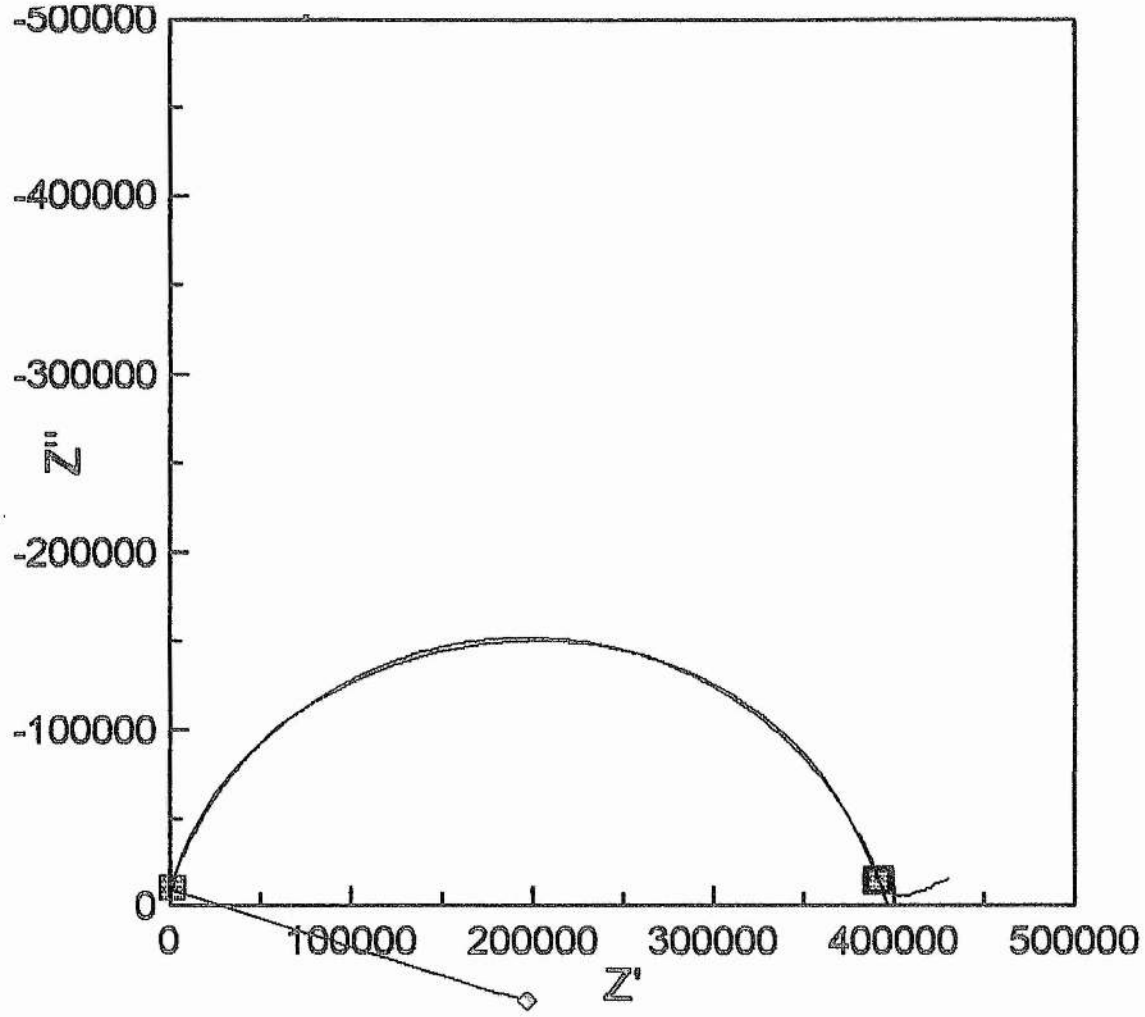

Figure 3.21: Typical impedance plot (uncorrected for geometric factor) obtained at 550°C for the $(ZrO_2)_{0.86}(MgO)_{0.0933}(TiO_2)_{0.0467}$ sample

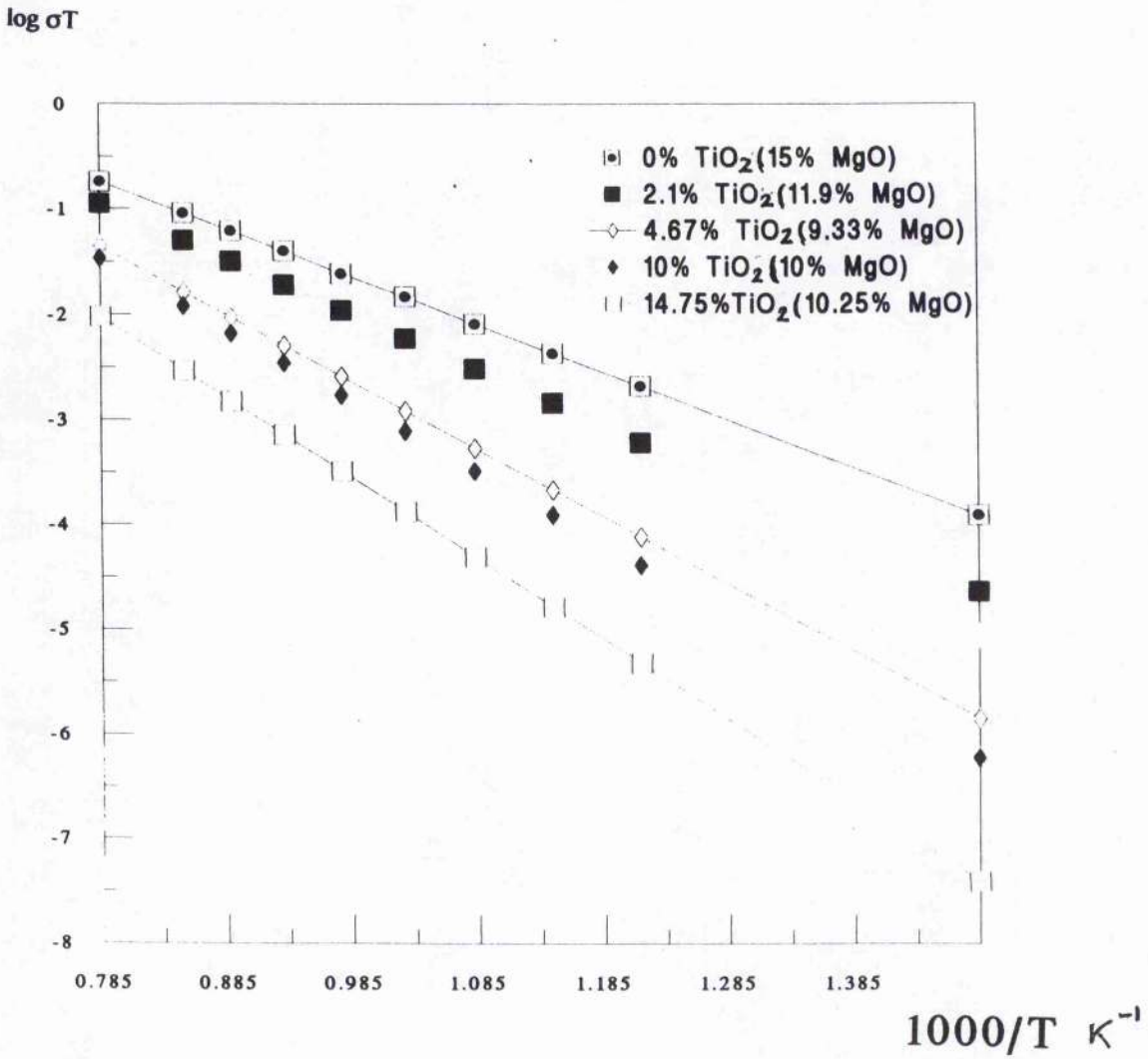

The number beside the TiO_2 content (in brackets) is the MgO content of the sample

Figure 3.22: Graph showing the variation of conductivity with temperature for the titanium substituted cubic-fluorite samples

Figure 3.23: Graph illustrating the variation between conductivity and % TiO_2 content in the titanium substituted cubic-fluorite samples at 800°C

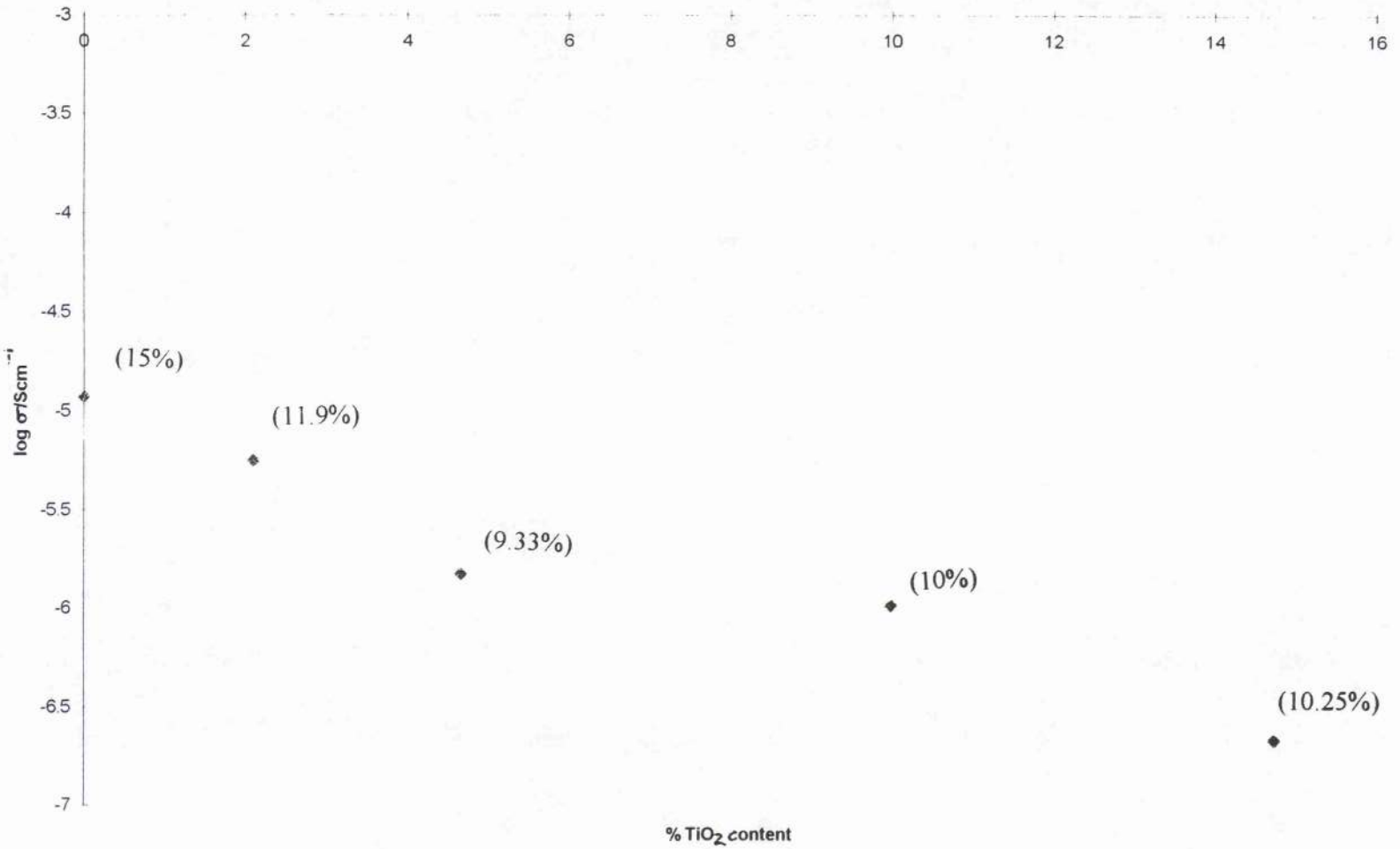

Figures in brackets represent the % MgO in the sample

Sample	Phases present	Activation energy value/eV
$(ZrO_2)_{0.85}$ $(MgO)_{0.15}$	Cubic-fluorite	0.90
$(ZrO_2)_{0.86}$ $(MgO)_{0.119}$ $(TiO_2)_{0.021}$	Cubic-fluorite	1.05
$(ZrO_2)_{0.86}$ $(MgO)_{0.0933}(TiO_2)_{0.0467}$	Cubic-fluorite	1.28
$(ZrO_2)_{0.8}(MgO)_{0.1}(TiO_2)_{0.1}$	Cubic-fluorite	1.35
$(ZrO_2)_{0.75}(MgO)_{0.1025}(TiO_2)_{0.1475}$	Cubic-fluorite	1.53
$(ZrO_2)_{0.57}$ $(MgO)_{0.28}$ $(TiO_2)_{0.15}$	Cubic-fluorite +MgO + Mg_2TiO_4	1.55
$(ZrO_2)0.67$ $(MgO)_{0.167}$ $(TiO_2)_{0.167}$	Cubic fluorite + MgO	1.74

Table 3.9: Activation energy values forsamples containing cubic-fluorite phase

has a larger ionic radius than zirconium, as the dopant level increases the activation energy increases due to cation-oxygen vacancy association[11].

3.7 References

1- JCPDS file number 45-096.

2- JCPDS file number 27-997

3- E.N.S. Muccillo and M. Leitz, *J. Eur. Cer. Soc.*, 1996, **16**, 453-465

4- V.S. Stubican, *Adv. Ceram.*, 1988, **24A**, 71-82

5- A.V. Shevchenko, L.M. Lopato, I.M. Maister and O.S. Gorbunov, *Russ. J. Inorg. Chem.* (Engl. Transl.), 1988, **25**, 1379-1381

6- L.W. Coughanour, R.S. Roth, S. Marzullo and F.E. Sennett, *J. Res. Nat. Bur. Stands.*, 1955, **52**, 191-199.

7- R. B. Neder, F. Frey and H. Schulz, *Acta. Cryst.*, 1990, **A46**, 799-809.

8- C. Zheng, private communication.

9- JCPDS file number 34-415.

10- A. Feighery, private communication

11- J.A. Kilner and R.J. Brook, *Solid State Ionics*, 1982, **6**, 237-252.

Chapter 4

Conclusions

4.1 Conclusions

The following conclusions may be drawn up on the basis of the results obtained from this thesis:

(a) This thesis has shown that the single-phase cubic-fluorite region is much smaller than the literature phase diagram[1] (Figure 1.18). The phase diagram, as shown in Figure 4.1, is therefore an amended version of the $MgO:TiO_2:ZrO_2$ ternary phase system, with particular emphasis on the ZrO_2 rich-region of the phase diagram at 1500°C. When the results are compared to the literature phase diagram, it can be seen that the literature phase diagram did not distinguish between two separate single phase regions in the zirconia-rich region as, from both theory[2,3] and Figure 4.1, there should be two separate single phase regions:tetragonal and cubic-fluorite.

(b) For the literature phase diagram, very few samples were prepared in the ZrO_2 rich region (Table 1.5), implying that the authors had not investigated the region extensively. According to Table 1.5, only two cubic-flourite samples were synthesised, one which was on the $MgO:ZrO_2$ binary join and one in the centre of the ZrO_2 rich region close to the $(ZrO_2)_{0.75}$ $(MgO)_{0.1025}$ $(TiO_2)_{0.1475}$ sample. It seems clear, therefore that the authors had not studied the region extensively. It was

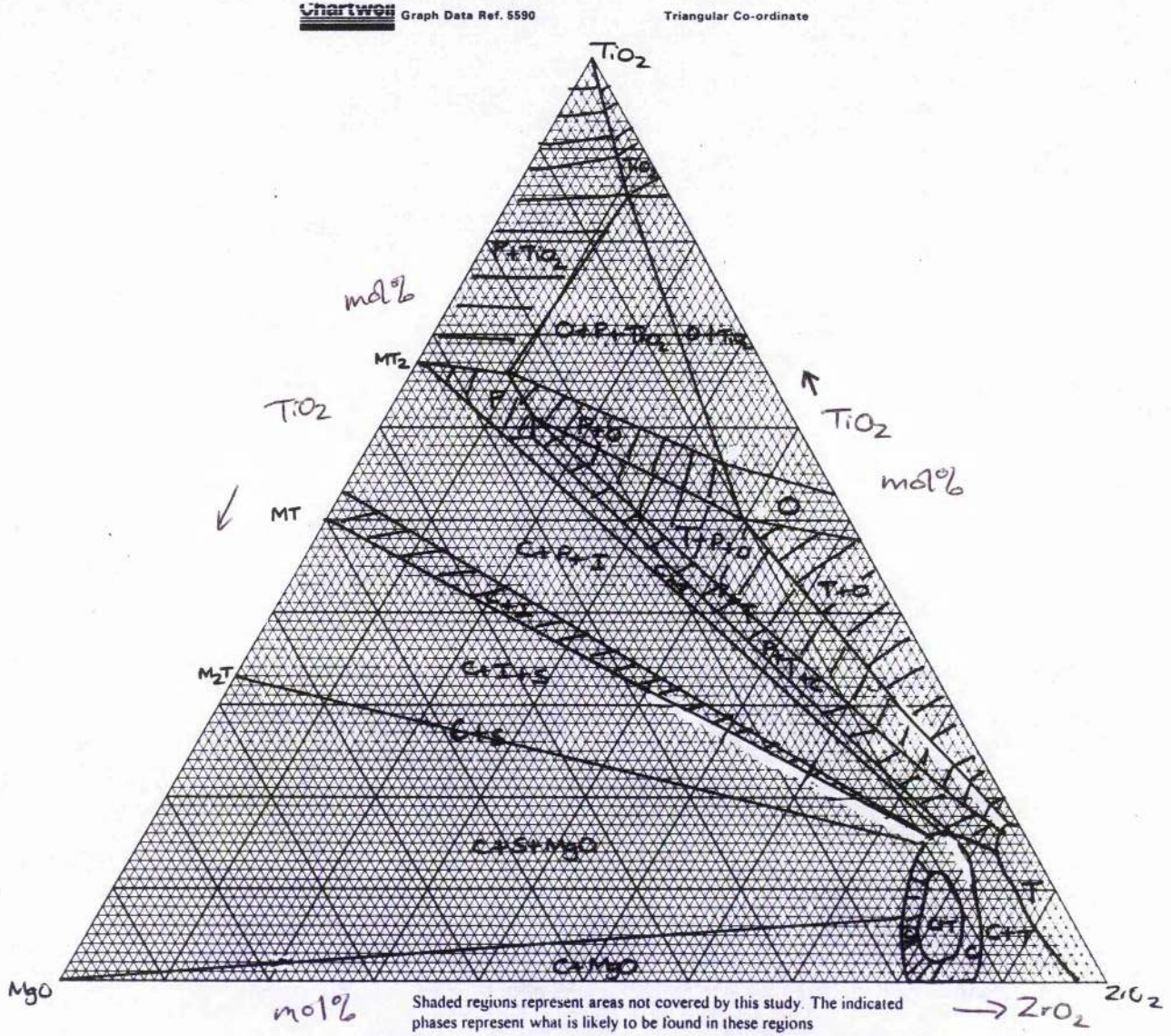

Shaded regions represent areas not covered by this study. The indicated phases represent what is likely to be found in these regions

Figure 4.1: Phase diagram showing location of both predicted and found phases at 1500°C

also noted that the literature phase diagram represented their analysis of samples at temperatures between 1450 and 1750°C. The conclusion was reached that the literature phase diagram did not pertain to 1500°C, at least.

(c) The cubic-fluorite region is circular with a two phase region in its centre with the pure cubic-fluorite region just outside the bi-phasic region. The presence of the two-phase region is due to the stability limit of the cubic-fluorite phase exceeding 1500°C in the centre of this region.

(d) Quenching of the samples did not reveal significant changes in sample structure or phase assemblage as the results of the samples obtained by quenching were similar to the results obtained by the conventional methods described in Chapter 2.3. Thus, our conventional methods pertain to cooling.

(e) The X-ray patterns of the samples that were annealed at 1000°C gave valuable information on the stability of the cubic-fluorite samples. The cubic-fluorite samples appeared to be thermodynamically unstable at 1000°C.

(f) The DTA traces of the 1000°C annealed samples which had been orignally prepared as cubic-fluorite phase only at 1500°C showed that the temperature required for the tetragonal to cubic-transition decreases as the TiO_2 content in the solid solution increased.

(g) The activation energy of conduction increases when there is an increased quantity of TiO_2 present in the solid solution. The

conductivity decreases due to the increased local distortions in the solid solution, which increases in proportion with the TiO_2 content. Overall, the ionic-conductivity of these samples is low for the cubic-fluorite phase[4].

Taking those factors into account, it will be possible to assess as to whether the $MgO:TiO_2:ZrO_2$ ternary system is a suitable material for use in solid oxide fuel cells.

(i) The materials that are used in the solid state synthesis of the cubic-fluorite phase are relatively cheap, non-toxic and easily obtainable. The time taken for synthesis is, however a problem as it is desirable to materials that are easily synthesised in a relatively short period of time as the synthesis of the cubic-fluorite phase is rather long at 72 hours.

(ii) The oxide-ion conductivity values are rather low when compared to other potential anodic materials such as ceria-stabilised zirconia .

(iii) The cubic-fluorite phase, once stabilised, is kinetically stable at temperatures between 1000 and 1500°C which may prove to be advantageous in terms of stability. It is important that the anode material must be stable during solid oxide fuel cell operation because if a sudden change in temperature occured, the material must not decompose rapidly as the solid oxide fuel cell must go back into operation as quickly as possible once the temperature change has been rectified.

4.2 Suggestions for future work

Two ideas which have not been extensively investigated could provide the basis of any future work to build up on the foundations of this project:

(i) It would be interesting to see the effects of a higher temperature on the samples in the biphasic region inside the cubic-fluorite region. If the

samples show only one phase, it would greatly assist in the explanation as to why there is a two phase region within a single phase region.

(ii) Confirmation is needed as to whether there is actually a semicircular region joining together samples 44 and 50 containing single-phase cubic-fluorite samples on the MgO rich domain as by theory there must be a join if the ZrO_2 rich domain between samples 44 and 50 is single phase cubic-fluorite, otherwise the samples on the MgO-rich side should contain tetragonal zirconia at 1500°C. This is probably the most important area of research that still needs to be done as it would be interesting to see if a trend can be made and compared with that of the other semi-circular region.

4.3 References

1- L.W. Coughanour, R.S. Roth, S. Marzullo and F.E. Sennett, *J. Res. Nat. Bur. Stands.*, 1955, **52**, 191-199.

2- V.S. Stubican, *Adv. Ceram.*, 1988, **24A**, 71-82

3- A.R.West, *Solid State Chemistry and its Applications*, John Wiley and Sons, Chichester, 1991.

4- J.A. Kilner and B.C.H. Steele in: *Non Stoichiometric Oxides*, ed. O. Sørenson, Academic Press, New York, 1981, 233-269

5- N.Q. Minh and T. Takahashi, *Science and Technology of Ceramic Fuel Cells*, Elsevier, Amsterdam, 1995.

Appendix 1

Kröger Vink [1] notation is commonly used to describe the reaction of point defects. For yttria stabilised zirconia, as an example, the point defects are:

Zr_{Zr}^{x} (x denotes zero effective charge)

$Y_{Zr}^{'}$ (' denotes a negative charge of -1)

Both cations occupy Zr lattice sites, denoted by subscript Zr.

O_{o}^{x}

$V_{o}^{\bullet\bullet}$ ($\bullet$ denotes a positive effective charge of +1)

Oxygen ion and oxygen vacancies occupy oxygen lattice sites. They are denoted by subscript O.

Reference

1- F.A. Kröger and J.A. Vink, J. Sol. State Phys., 1956, 3, 307.

Appendix 2

Selected X-ray patterns

The following pages contain the X-ray patterns of the following samples:

Number	Sample	Phases present
A2.1	$ZrTiO_4$ (Sample 12)	O
A2.2	$(ZrO_2)_{0.83}(MgO)_{0.11}(TiO_2)_{0.06}$ (Sample 53)	C + M
A2.3	$(ZrO_2)_{0.5}(MgO)_{0.165}(TiO_2)_{0.335}$ (Sample 11)	C + P
A2.4	$(ZrO_2)_{0.64}(MgO)_{0.20}$ $(TiO2)_{0.16}$ (Sample 23)	C + MgO
A2.5	$(ZrO_2)_{0.87}(MgO)_{0.065}(TiO_2)_{0.065}$ (Sample 59)	C + M

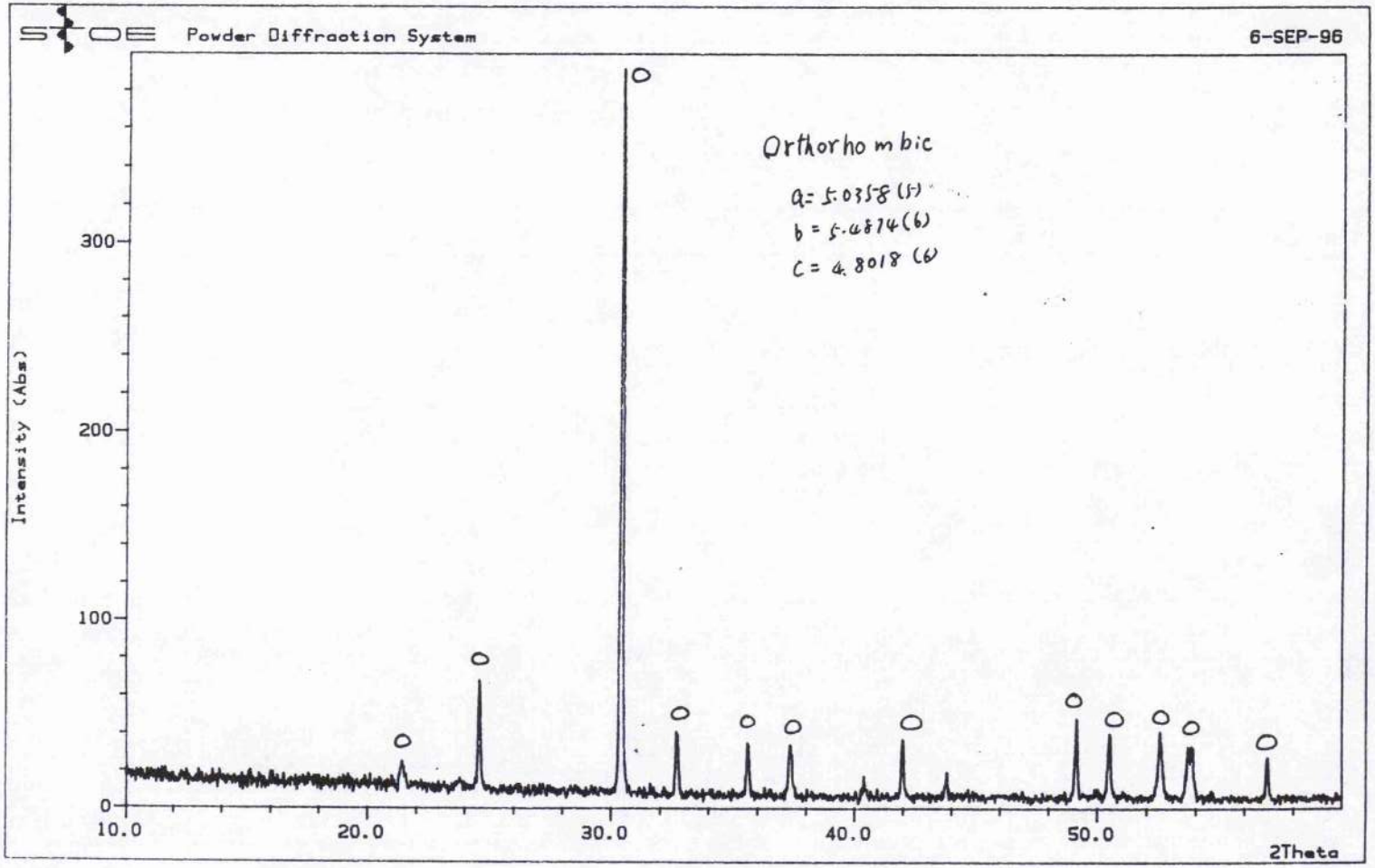

Figure A2.1: $ZrTiO_4$ (Sample 12)

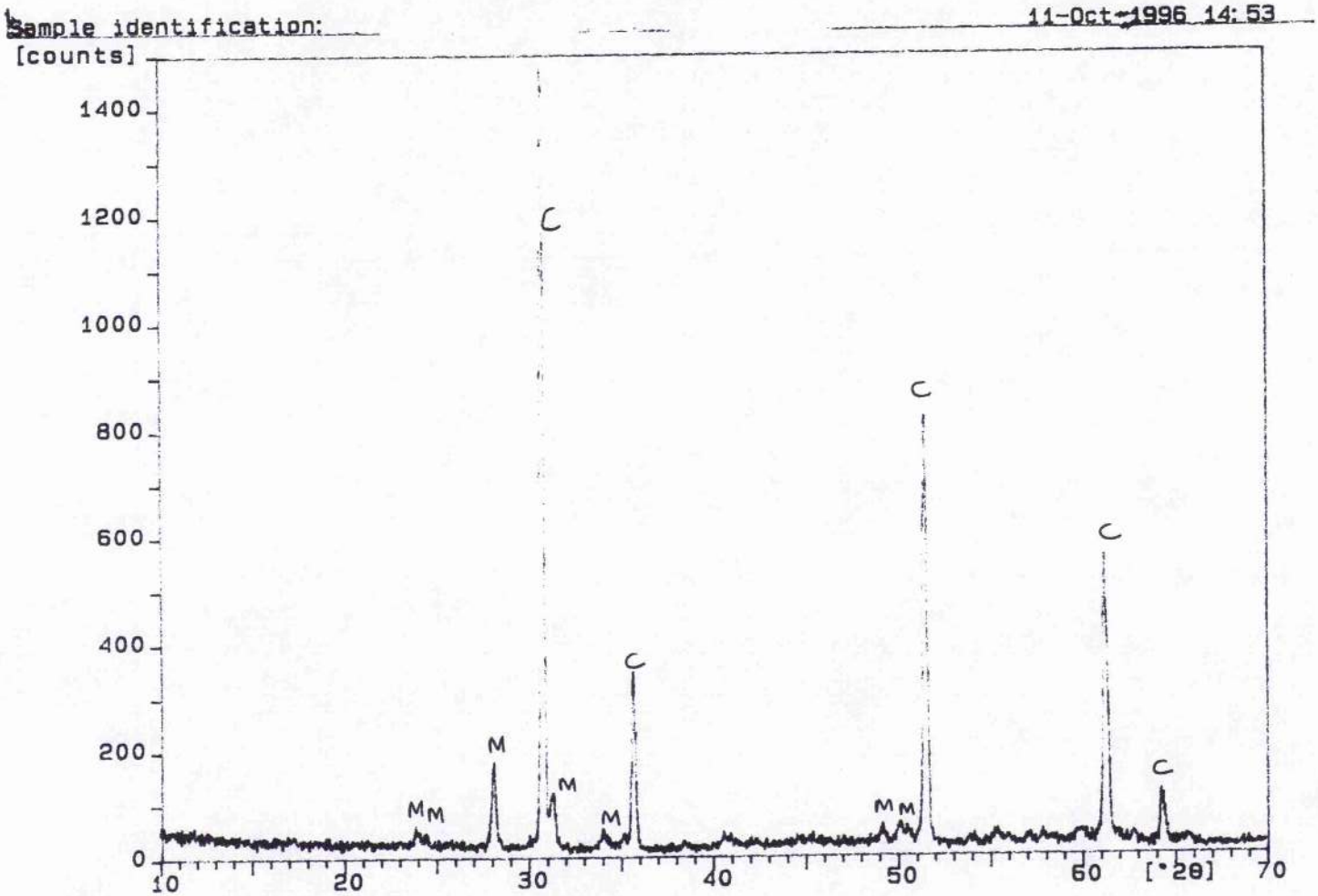

Figure A2.2: $(ZrO_2)_{0.83}\ (MgO)_{0.11}(TiO_2)_{0.06}$ (Sample 53)

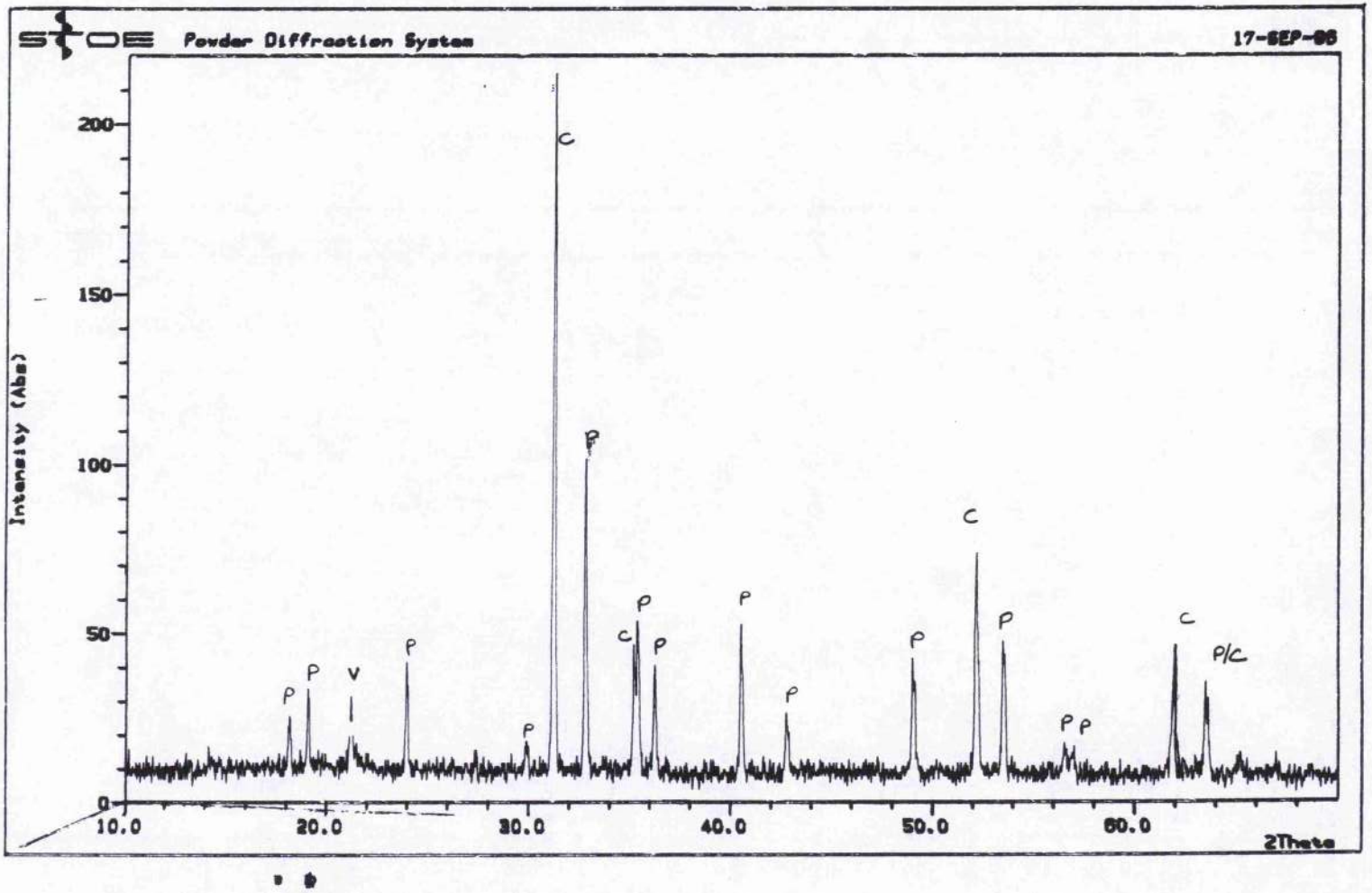

Figure A2.3: $(ZrO_2)_{0.5}\ (MgO)_{0.11}\ (TiO_2)_{0.06}$ (Sample 11)

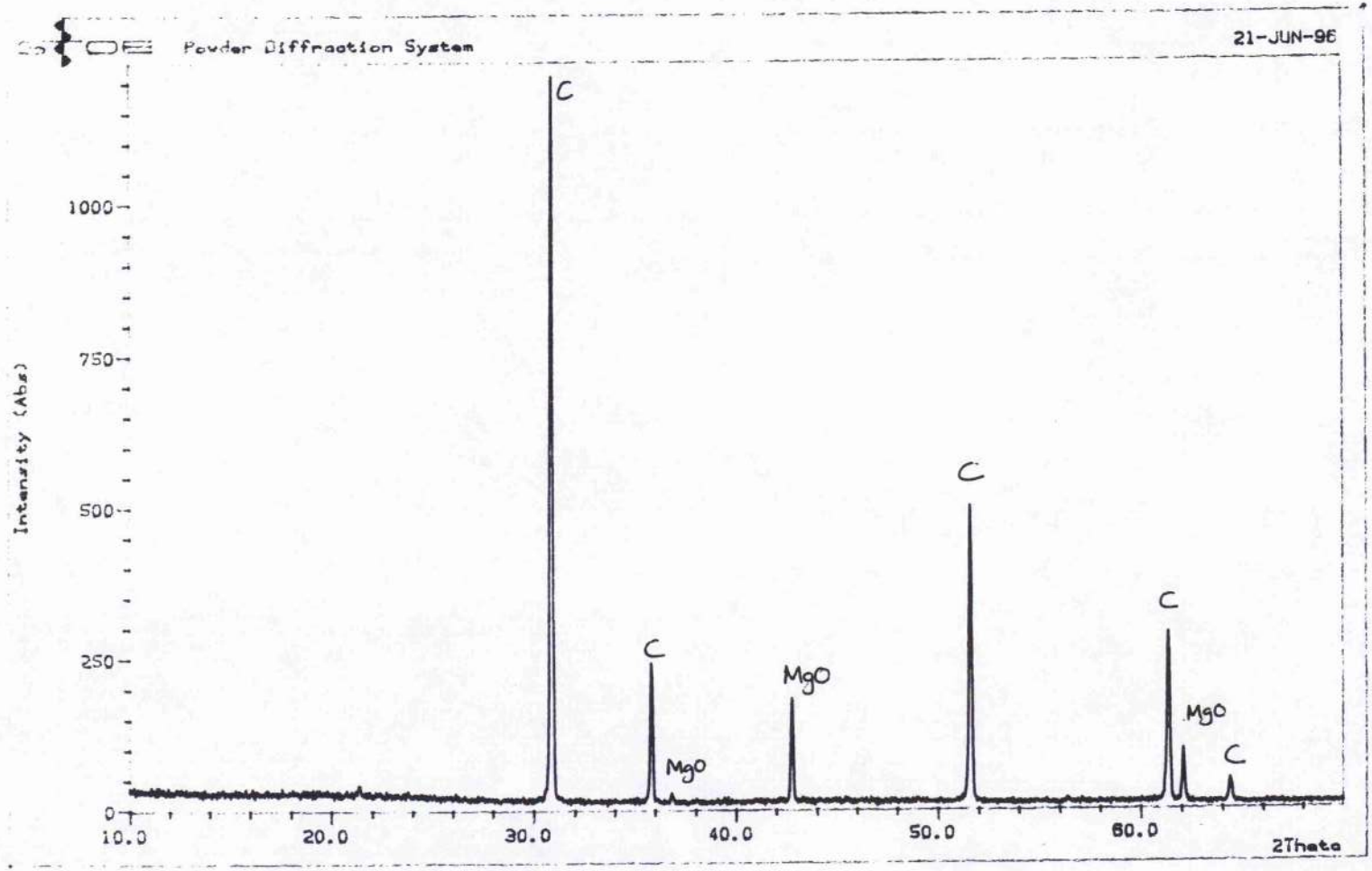

Figure A2.4: $(ZrO_2)_{0.64}(MgO)_{0.2}(TiO_2)0.16$ (Sample 23)

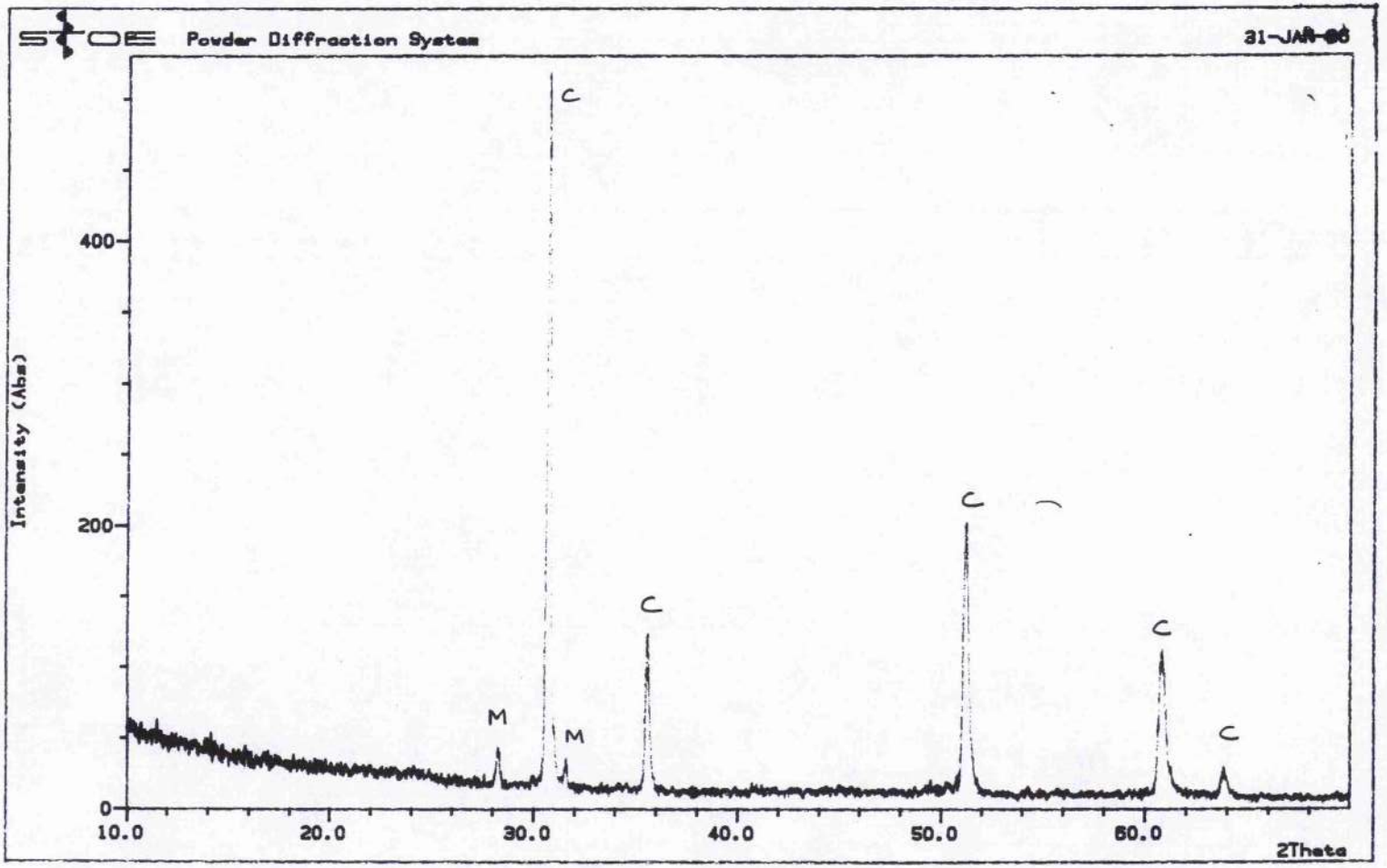

Figure A2.5 $(ZrO_2)_{0.87}(MgO)_{0.065}(TiO_{})_{0.065}$ (Sample 59)